



City Research Online

City, University of London Institutional Repository

Citation: Patel, B. (2023). Leakage flows and Conjugate Heat Transfer in Rotary Positive Displacement Machines. (Unpublished Doctoral thesis, City, University of London)

This is the accepted version of the paper.

This version of the publication may differ from the final published version.

Permanent repository link: <https://openaccess.city.ac.uk/id/eprint/30708/>

Link to published version:

Copyright: City Research Online aims to make research outputs of City, University of London available to a wider audience. Copyright and Moral Rights remain with the author(s) and/or copyright holders. URLs from City Research Online may be freely distributed and linked to.

Reuse: Copies of full items can be used for personal research or study, educational, or not-for-profit purposes without prior permission or charge. Provided that the authors, title and full bibliographic details are credited, a hyperlink and/or URL is given for the original metadata page and the content is not changed in any way.



Leakage flows and Conjugate Heat Transfer in Rotary Positive Displacement Machines

By

Brijeshkumar Ashokbhai Patel

Thesis submitted for the degree of Doctor of Philosophy
in Mechanical Engineering

City, University of London
School of Science & Technology

February 2023

Table of Contents

Table of Contents	i
List of figures	iv
List of Tables	x
Acknowledgement	xi
Declaration	xii
Abstract	xiii
Nomenclature	xiv
Chapter - 1 Introduction	1
1.1 Clearances and leakage flow in PDMs	3
1.2 Heat transfer in clearances	5
1.3 Thesis outline	6
Chapter - 2 Literature Review	8
2.1 Leakage flows	8
2.2 Heat transfer in leakage flows	15
2.3 Velocity field, temperature field and surface temperature measurement	19
2.3.1 Measurement of velocity field	19
2.3.2 Measurement of temperature field	22
2.3.3 Surface temperature measurement	25
2.4 Conclusion from the literature review	27
Chapter - 3 Objectives, Methodology and Expected contributions	29
3.1 Objectives	29
3.2 Methodology	29
3.3 Expected contribution	30
Chapter - 4 PLIF Experimental Study	32
4.1 PLIF experimental setup and procedures	32
4.1.1 Roots blower test rig	32

4.1.2	PLIF Imaging	35
4.1.3	Development of the 2-colour LIF using single camera.....	36
4.1.4	Development of the 2-colour LIF using two cameras.....	40
4.1.5	Temperature calibration and image processing	42
4.2	PLIF measurement results: advantages and limitations of the technique	43
4.3	Uncertainty in PLIF measurements.....	50
	Summary	51
Chapter - 5	IR Thermography Experimental Study	52
5.1	IR thermography experimental setup and procedures	52
5.1.1	IR thermography experimental setup.....	52
5.1.2	IR thermography experimental procedure	53
5.2	Infrared thermography measurement results	55
5.3	Uncertainty in IR thermography measurements.....	64
5.4	Summary	66
Chapter - 6	PIV Experimental Study	68
6.1	PIV experimental setup and procedure	68
6.1.1	DAQ system.....	68
6.1.2	Functional devices and seeding particles	69
6.1.3	Particle image velocimetry setup	72
6.1.4	PIV measurements	73
6.1.5	PIV data processing	75
6.2	PIV measurements and results	77
6.2.1	Measurement of the flow field in the clearance gap between the tip and casing	78
6.2.2	Results at the clearance between tip and casing	78
6.2.3	Results at the exit of the tip (trailing edge).....	87
6.2.4	Results at the entrance of the tip (Leading edge).....	91
6.3	Uncertainty in PIV measurements.....	94

6.4	Summary	96
Chapter - 7	Combined result analysis and CHT comparison.....	97
7.1	Flow field inside the clearance between tip and casing	97
7.2	Flow field at the exit of the clearance	100
7.3	Flow field at the entrance of the tip.....	105
7.4	Temperature and flow field over the Tip.....	109
7.5	Conjugate heat transfer analysis results	112
7.6	Summary	118
Chapter - 8	Conclusion, Recommendations and Contributions to Knowledge	119
8.1	Conclusion.....	119
8.2	Recommendations for future work.....	121
8.2.1	PIV experiments with various tip geometries	121
8.2.2	PLIF Experiments	121
8.3	Contributions to knowledge	123
References	125
Appendix A	Modelling of conjugate heat transfer in clearance gap of a Roots blower	130
A.1	Computational domain for CHT model.....	130
A.2	CHT Simulation setup	131
Appendix B	MATLAB code for PLIF- two camera image mapping	134

List of figures

Figure 1.1 Classification of compressors [4]	2
Figure 1.2 (a) Screw compressor[4] (b) Roots blower.....	3
Figure 1.3 Representation of clearance between Rotor Tip and Housing	4
Figure 1.4 (a) Various leakage paths in rotary screw machine and key contributors are highlighted with red arrows [6] (b) Various leakage paths in Roots Blower	4
Figure 1.5 Clearance flow investigated by Sachs using schlieren method[9]	5
Figure 1.6 Generalized heat transfer concept in clearance	5
Figure 2.1 Simulation results for different turbulence models; pressure ratio 0.5, inlet pressure 2 bar; minimum clearance height 0.4 mm[12].....	9
Figure 2.2 Contours of Mach number and velocity profiles in the male rotor-housing gap obtained by segregated solver using Spalart-Allmaras turbulence model on the finest grid of 178×68 cells for the angular velocity of 9000 rpm [13].....	10
Figure 2.3 High speed camera and CFD comparison for the gate rotor [15].....	10
Figure 2.4 schematic of tip leakage flow, with cut planes showing low speed behaviour over the front of the tip (A) and high speed over the rear (B) [20].....	11
Figure 2.5 Mach number contours along an axial cut plane for subsonic and transonic tip flow: a) $M = 0.37$ and b) $M = 1.01$ [21].	12
Figure 2.6 Comparison between the PIV results and CFD results at various crank angle positions and 625 rpm rotor speed [23]	14
Figure 2.7 The velocity and pressure distribution in the tip gap at the crank angle of 43° under the pressure ratio of 1.015(Left) and 1.072(Right): (a) velocity field, (b) Total pressure, (c) Static pressure[24].....	15
Figure 2.8 Temperature profile in clearance between rotor and casing for laminar flow for the case $T_{\text{gas}} > T_{\text{Rotor \& Casing}}$ [25].....	16
Figure 2.9 Comparison of fully developed temperature profile of laminar flow and turbulent flow [25]	16
Figure 2.10 Tip surface heat flux(W/m^2) and X-components of density gradient (kg/m^2) distributions on four cut planes (HYDRA Prediction) [10].....	17
Figure 2.11 Mach number distributions on cut plane B (transonic region)	18
Figure 2.12 Schematic of a parallel-light Z-type schlieren system [34].....	20
Figure 2.13 PIV measurement principle (Image from Dantec Dynamics [39]).....	22
Figure 2.14 Basic imaging setup for LIF technique (LaVision).....	23
Figure 2.15 Schematic of holographic interferometer [54].....	24

Figure 2.16 Basic setup of IR thermography	26
Figure 2.17 Planck’s Radiation Law & Wien’s displacement law	26
Figure 2.18 Importance of leakage flow study in positive displacement machine	28
Figure 3.1 Research methodology	30
Figure 4.1 Schematic diagram of Roots blower test rig.....	33
Figure 4.2 Rotors position in the Roots blower [23].....	34
Figure 4.3 (a) Optical element made from fused silica glass (b) Radial optical access of Roots blower to apply laser sheet (c) Optical access from side of Roots blower to visualize radial clearance	35
Figure 4.4 Arrangement of optics and Roots blower for single camera LIF imaging and measurement (a) Fused silica curved window	38
Figure 4.5 Single camera LIF setup	39
Figure 4.6 (a) Instantaneous image at 50° crank angle & captured using 320nm filter (b) Instantaneous image at 50° crank angle & captured using 280nm filter	40
Figure 4.7 Arrangement of optics and Roots blower for double camera LIF imaging and measurement	40
Figure 4.8 Two camera LIF setup	41
Figure 4.9 Two frames captured simultaneously at 300 RPM by two camera arrangement (a) Frame 0 captured by camera using 320nm filter (b) Frame 1 captured by camera using 280nm filters	42
Figure 4.10 Considered large volume ‘V’ on discharge side of the machine for temperature calibration.....	42
Figure 4.11 Schematic overview of the data processing for LIF imaging.....	43
Figure 4.12 Temperature field in the clearance gap with temperature variation across the clearance from single camera LIF measurement (300 to 900 RPM)	45
Figure 4.13 Temperature field in the clearance gap with temperature variation across the clearance from single camera LIF measurement (1200 & 1500 RPM)	46
Figure 4.14 Comparison of temperature variation across the clearance gap at different RPM from single camera LIF measurement	46
Figure 4.15 Temperature field in clearance gap with temperature variation across tip clearance from two camera LIF measurement (300 RPM to 900 RPM)	48
Figure 4.16 Temperature field in clearance gap with temperature variation across tip clearance from two camera LIF measurement (1200 RPM to 2000 RPM)	49

Figure 4.17 Comparison of temperature variation across the clearance gap at different RPM from two camera LIF measurement.....	50
Figure 5.1 High speed Infrared thermography setup	53
Figure 5.2 High speed infrared thermography test setup to measure lobe surface temperature.....	54
Figure 5.3 Images of Tip1 and Tip2 of the lobe	54
Figure 5.4 (a) High speed IR camera setup for casing temperature measurement (b) Black painted focused side of Roots blower (C) Example of thermogram of Roots blower.....	55
Figure 5.5 Thermograms of Tip1 and Tip2 at 1.2 PR various speeds obtained by averaging 500 instantaneous images represent surface temperature variation from high pressure side to low pressure side.	57
Figure 5.6 Thermograms of Tip1 and Tip2 at 1.4 PR and 1.6 PR various speeds obtained by averaging 500 instantaneous images represent surface temperature variation from high pressure side to low pressure side.	58
Figure 5.7 Temperature of lobe surface on discharge/high-pressure side obtained on the line from P1 to P5	59
Figure 5.8 Surface temperature comparison of Tip1 and Tip2	59
Figure 5.9 Temperature of lobe surface across the tip over the line L from suction to discharge for all operating conditions.....	60
Figure 5.10 Casing temperature for 1000 RPM to 2000 RPM and 1.2PR to 1.6PR.....	61
Figure 5.11 Temperature over location R1, R2, R3 at 1.2 PR, 1.4 PR and 1.6 PR	62
Figure 5.12 Temperature measurement at various time interval at 2000 RPM and 1.4 pressure ratio (Machine was started at 09:23:20)	63
Figure 5.13 Temperature over the time at the location at R1, R2, R3 on casing surface at 2000RPM and 1.4 PR	63
Figure 6.1 Schematic diagram of Roots blower test rig.....	68
Figure 6.2 DAQ system with Power supply unit	69
Figure 6.3 Litron Bernoulli laser with specifications	70
Figure 6.4 HiSense Zyla Camera (Dantec Dynamics).....	70
Figure 6.5 Synchronizer.....	71
Figure 6.6 (a) Light guide arm (b) parallel optics.....	71
Figure 6.7 (a) PIV experiment setup layout (b) Actual PIV setup.....	72
Figure 6.8 Measurement plane, position and tip step dimensions	73

Figure 6.9 (a) FOV at clearance between tip and casing (b) FOV at trailing edge of clearance (c) FOV at leading edge of clearance.....	74
Figure 6.10 (a) Raw image (b) Image after subtracting background noise.....	76
Figure 6.11 Scaling of PIV data.....	76
Figure 6.12 Cross correlation map for PIV	77
Figure 6.13 Raw images of flow field at various operating conditions	78
Figure 6.14 Velocity fluctuations in the streamwise region at reference frames: $t = t_0$, $t_0+0.18$ s, t_0+36 s for 1000RPM and 1.2PR	79
Figure 6.15 Time averaged velocity magnitude at 1.6 PR and various speeds.....	81
Figure 6.16 Time averaged velocity magnitude at 1.4 PR and various speeds.....	82
Figure 6.17 Time averaged velocity magnitude at 1.2 PR and various speeds.....	83
Figure 6.18 Comparison of the average velocity in the clearance gap at all measured conditions	84
Figure 6.19 Velocity profile across the clearance from rotor tip to casing obtained by averaging 3 profiles considered above the centre of the clearance (a) at 1.2 PR (b) at 1.4 PR (c) at 1.6 PR.....	85
Figure 6.20 Comparison of volume flow rate calculated using the entire velocity profile and partial velocity profile	86
Figure 6.21 Instantaneous vorticity contours: $t = t_0$, $t_0+0.09$ s, t_0+18 s at 2000 RPM and 1.2, 1.4 & 1.6 PR super imposed with velocity vectors.....	89
Figure 6.22 Instantaneous vorticity contours: $t = t_0$, $t_0+0.07$ s, t_0+14 s at 0 RPM and 1.2, 1.4 & 1.6 PR super imposed with velocity vectors	90
Figure 6.23 Swirl strength at all measured conditions at trailing edge of the tip (contours are derived from the average of 10 instantaneous plots).....	91
Figure 6.24 Contour of velocity gradient for all the operating conditions over the average flow field of 10 instantaneous vector field superimposed with velocity vectors	93
Figure 6.25 Scaler map of uncertainty inside the clearance at 1000RPM and 1.2 PR....	95
Figure 6.26 Scaler map of uncertainty at the exit of the clearance at 1000RPM and 1.2 PR.....	95
Figure 6.27 Scaler map of uncertainty at the entrance of the clearance at 1000RPM and 1.2 PR.....	96
Figure 7.1 Visualization of the mean velocity field inside the clearance at 2000 RPM and 1.6 PR.....	97

Figure 7.2 Velocity over the line ‘A’ across the clearance at 1.2 PR and various speed	99
Figure 7.3 Velocity over the line ‘A’ across the clearance at 1.4 PR and various speed	99
Figure 7.4 Velocity over the line ‘A’ across the clearance at 1.6 PR and various speed	
.....	100
Figure 7.5 (a) velocity vector (b) streamlines (c) vorticity contour for 2000RPM and 1.6 PR	
.....	101
Figure 7.6 Vorticity at all the measured condition	101
Figure 7.7 Turbulence intensity at 1.2 PR and various speed	102
Figure 7.8 Turbulence intensity at 1.4 PR and various speed	103
Figure 7.9 Turbulence intensity at 1.6 PR and various speed	104
Figure 7.10 Energy spectrum Log-Log curve for all measured conditions	105
Figure 7.11 (a) Velocity vectors (b) Streamlines (c) Vorticity contour at 2000RPM and 1.6 PR	
.....	106
Figure 7.12 Turbulence intensity at 1.2 PR	107
Figure 7.13 Turbulence intensity at 1.4 PR	108
Figure 7.14 Turbulence intensity at 1.6PR	109
Figure 7.15 Streamlines of flow field and measured surface temperature map of lobe in same plane at 2000 RPM and 1.6PR	
.....	110
Figure 7.16 Temperature along line L1 at 1.6PR and various speeds	110
Figure 7.17 Temperature along line L1 at 1.4 PR and various speeds	111
Figure 7.18 Temperature along line L1 at 1.2 PR and various speeds	111
Figure 7.19 Thermography camera views a) Rotor lobe surface, b) Housing surface	113
Figure 7.20 Surface temperature on the rotor lobe at 1000 rpm, 1.2 pressure ratio	114
Figure 7.21 Surface temperature on the rotor lobe at 1500 rpm, 1.2 pressure ratio	114
Figure 7.22 Surface temperature on the rotor lobe at 2000 rpm, 1.2 pressure ratio	115
Figure 7.23 Surface temperature on the rotor lobe at 2000 rpm, 1.4 pressure ratio	115
Figure 7.24 Surface temperature on the rotor lobe at 2000 rpm, 1.6 pressure ratio	116
Figure 7.25 Surface temperature on the blower housing at 2000 rpm, 1.4 and 1.6 pressure ratio	
.....	117
Figure 8.1 Schematic of flow structures found from the measurement in leakage flows	
.....	120
Figure 8.2 Various tip geometries	121
Figure 8.3 Dual scope with camera	122

Figure 8.4 Measured and calculated signals per volume in N₂ and air (acetone only in N₂) relative to those of toluene in N₂ at room temperature[52]. 123

List of Tables

Table 4.1 The main parameters of the Roots blower	34
Table 4.2 Sensor specifications.....	34
Table 4.3 Operating conditions during single camera LIF test.....	39
Table 4.4 Operating conditions during two camera LIF test	41
Table 5.1 Test conditions for IR thermography	53
Table 5.2 Uncertainty components in measurement by infrared thermography.....	65
Table 6.1 Specifications of the national instrument modules	68
Table 6.2 characteristics of the selected PIV camera.....	70
Table 6.3 Machine operating conditions.....	74
Table 7.1 Conjugate heat transfer analysis results	113
Table 7.2 Comparison of IR Thermography and CHT results on rotor lobe	116
Table 7.3 Comparison of IR Thermography and CHT results on housing	117

Acknowledgement

My gratitude goes towards the Centre for Compressor Technology of City, University of London, for providing me the necessary infrastructure, financial assistance and platform to carry out this research and to advance my career. I would like to express my gratitude to my guide and supervisor Prof Ahmed Kovacevic who has provided me with continual advice and support. Because of him this research work became part of the project which is funded by Royal Academy of Engineering and Howden compressors, UK.

I could not have started this research without support of my family members: my parents, grandparents and sister. I acknowledge their sacrifices and contribution during the course of my research. I would like to thank my wife as well who has joined me in this journey in latter phase. Without my family's support I would not have come this far.

I would like to thank all my colleagues and friends for their help and advice whenever I needed. I also thank laboratory technical staff of City for their support for this research work.

Brijeshkumar Patel

City, University of London, 2023

Declaration

I hereby declare that all work produced in this document is entirely my own work, except where otherwise indicated, and has not been submitted in whole or in part to any other university.

I grant powers of discretion to the Director of Library Services to allow the thesis to be copied in whole or in part without further reference to me. This permission covers only single copies made for study purposes, subject to normal conditions of acknowledgement.

Brijeshkumar Patel

London, 2023

Abstract

This study investigates the fluid flow and Conjugate Heat Transfer (CHT) in the clearance gaps during the operation of an optical Roots blower, which is a type of rotary Positive Displacement Machine (PDM) commonly used in energy generation and conversion systems. Leakage flow through clearance gaps between rotating and stationary elements of PDM's is a major contributor to efficiency loss and reducing clearances can cause reliability issues, especially in oil-free PDMs. However, high fidelity measurements of flow and temperatures in clearances during operation of PDM and measurements of thermo-fluid-solid interaction in clearance gaps are not reported. To address this gap, the study employs three optical measurement techniques, namely Planar Laser-Induced Fluorescence (PLIF) to measure the air temperature in clearances, Particle Image Velocimetry (PIV) to measure flow velocities, and high-speed Infrared Thermography (IR) to measure lobe and casing surface temperatures. The data collected are post-processed and analyzed using specialized data visualization software. The study establishes a state-of-the-art experimental test rig to explore the physics of flow and heat transfer in clearance gaps, and the experimental data validate the numerical models of CHT in clearance flows. The results of the study provide new insights into the difference in clearance flow between stationary and running conditions and show the presence of secondary flows such as boundary layer and vortices, which are different from measurements in stationary condition. The findings from this study are used to implement new active control methods to control leakages through clearances.

The contributions of this study are the establishment of a experimental setup for exploring the physics of the flow and heat transfer in clearance gaps, the understanding of the difference in the clearance flow between stationary and running conditions, and experimental data for the validation of numerical models of CHT in clearance flows.

A new design for the tip shape of clearance has been proposed, which aims to reduce leakage flow. Additionally, an improved setup for Planar Laser-Induced Fluorescence (PLIF) has been proposed to accurately measure the temperature inside the clearance. Further work is planned to investigate clearance flows through different shapes of clearance gaps using both PLIF and PIV measurements.

Nomenclature

Symbol	Description
T	Temperature (K)
Q	Heat transfer rate (W)
V	Velocity (m/s)
t	Time (s)
M	Mach number
h	Planck constant (Js)
h'	Heat transfer coefficient (W/m ² K)
c	Speed of light (m/s)
k	Boltzmann constant (J/K)
P	Pressure (bar)
E	Laser fluence (J/m ²)
A	Area (m ²)
S	Collected signal
f	Focal length (m)
l	Litre (l)
<i>IV</i>	Imaged field
<i>St</i>	Stokes number
d	Diameter (m)
L	Length (m)
u'	Velocity fluctuation in PIV plots (m/s)
u	Instantaneous velocity in PIV plots (m/s)
\bar{u}	Mean velocity (m/s)

v'	Velocity of object
C_d	Coefficient of discharge
x, y, z	Cartesian coordinates
V	Velocity components in y directions (m/s)
U	Velocity components in x directions (m/s)
Re	Reynolds number
Nu	Nusselt number
Pr	Prandtl number
Δx	Distance travel by object (m/s)
$u()$	Uncertainty

Greek symbols

λ	Wavelength (nm)
Δ	Difference
η	Efficiency
v	Tracer density (g/m ³)
σ	Light sheet cross section (m ²)
ϕ	Quantum yield
ρ	Density (kg/m ³)
μ	Dynamic viscosity (Pa s)
ξ	Factor for contraction and expansion
Σ	Shape factor
ω	Rotation of vorticity (1/s)
τ	Velocity gradient (1/s)

Subscripts

C	Casing
-----	--------

R	Rotor
<i>opt</i>	Optics
<i>pix</i>	Pixel
<i>abs</i>	Absorption
<i>f</i>	Fluorescence
<i>P</i>	Particle
<i>F</i>	Fluid
c	Contraction
e	Expansion
ε	Emmissivity
<i>cal</i>	Calibration

Abbreviation

CAS	Compressed Air Sector
PDM	Positive Displacement Machines
CFD	Computational Fluid Dynamics
LDV	Laser Doppler Velocimetry
OTL	Over Tip Leakage
HC	High Speed Camera
CPIV	Continuous Particle Image Velocimetry
IPIV	Instantaneous Particle Image Velocimetry
TR	Temperature Ratio
PR	Pressure Ratio
MWIR	Mid-Wave Infrared
LWIR	Long-Wave Infrared
PLIF	Planar Laser Induced Fluorescence

PIV	Particle Image Velocimetry
IRT	Infrared Thermography
CCD	Charge-coupled Device
CMOS	Complementary Metal Oxide Semiconductor
DHI	Digital Holographic Interferometry
VFD	Variable Frequency Drive
VDM	Vapour Delivery Module
RPM	Revolution Per Minute
IRO	Intensified Relay Optics
DAQ	Data Acquisition System
NI	National Instruments
FOV	Field of View
FPGA	Field Programmable Gate Arrays
SCORG	Screw Compressor Rotor Grid Generator

Chapter - 1 Introduction

The Compressed Air Sector (CAS) accounts for 20% of worldwide electricity consumption, and thus is being re-thought as an area offering great opportunities for improvement. Considering that the compression is responsible for 10-15% consumption, it is vital to pay attention to machines performances [1]. A study on carbon and energy saving markets in compressed air calculated the allocations of carbon dioxide emissions currently associated to the compressors in use and subsequent possible energy savings based on an analysis of data provided by CAGI (Compressed Air Gas Institute) and PNEUROP (European Association of manufacturers of compressors, vacuum pumps, pneumatic tools and allied equipment). The economic value was then associated with the obtainable savings, referring to the value that these savings would have if converted into CO₂ emission allowances or energy certificates traded on the European energy markets. The findings of the study place the financial value associated with the possible energy savings in the compressed air sector at between 165 and 385 million euros, with an expectation for the near future of a further increase in the range 200-500 million euro [2]. The energy saving potential for this sector is particularly high and has been calculated at between 25 and 50% of current consumption. To reach this allowance, it is necessary to put actions into place at mainly three different levels: leakage control, optimization of pressure levels on distribution lines and the replacement of obsolete technology with new machines [3].

Compressors are classified based on the gas pressurization principle as shown in Figure 1.1. Rotary screw compressors are classified as positive displacement machines because gas is compressed by reduction of its volume. Rotary positive displacement machines (PDMs) are the major proportion of CAS and used in a large number of industrial applications. These are the devices used to move fluids, such as liquids, gases or slurries. This device displaces a volume by physical or mechanical action. A positive displacement device has an expanding cavity on the suction side and a decreasing cavity on the discharge side. Fluid flows into the machine as the cavity on the suction side expands and the fluid flows out of the discharge as the cavity collapses. The volume confined inside the machine is constant given each cycle of operation. Positive displacement units are those in which successive volumes of fluid are confined within a closed space and elevated to a higher pressure. Their efficiency is influenced by leakage through the clearance gaps between their stationary and rotating parts. Heat transfer rates between the

gas and the machine parts change during the compression process, which can cause differential expansion of components and lead to deterioration of efficiency and reliability. Understanding of the leakage flows and heat transfer in rotary PDMs are two vital elements to leverage towards improvements in reliability and efficiency of these machines.

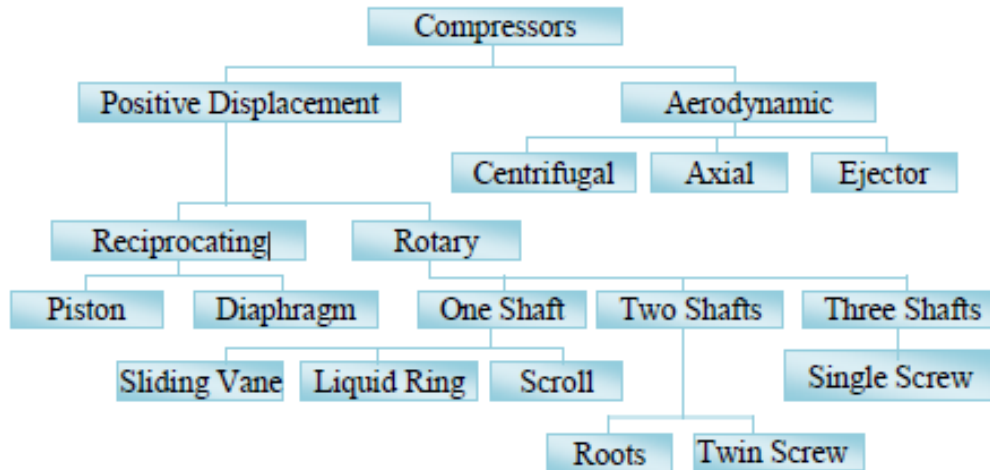


Figure 1.1 Classification of compressors [4]

Structure of screw compressor and Roots blower is shown in Figure 1.2 In these both type of machines, two rotors rotate around their axes and this intermesh create working chambers with the housing. Compression happens as these chambers reduce when rotors rotate. Rotary screw machines can be dry or could have fluid injected in the working chamber. Injected fluid serves the purpose of gas cooling, sealing of clearances and lubrication of rotors as they are in direct contact. Due to the heat of compression removed by liquid in direct contact machines with the gas, thermal management of clearances in oil flooded compressors is easy and they take large share in the market. For example, oil free screw compressors have only 13% of the market. The main difference of the Roots blower and screw compressor is that the Roots blower has straight lobes, therefore achieving fluid transfer without internal compression. However, its simple geometry allows optical access for measurements of leakage flows in radial clearance gaps.

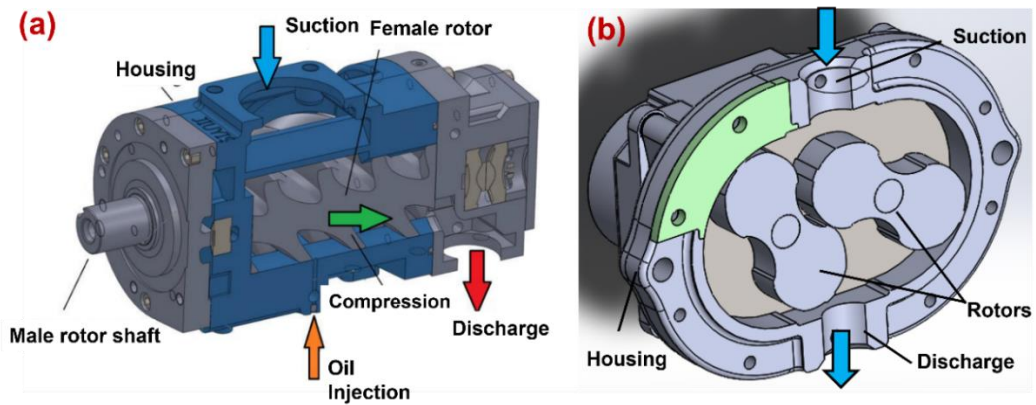


Figure 1.2 (a) Screw compressor[4] (b) Roots blower

One of the main objectives set in the latest report published by the Intergovernmental Panel on Climate Change (IPCC), to achieve net zero CO₂ targets adopted by governments for next decades [5], is to improve efficiency of machines like compressors as well as to reduce consumption and use of fossil fuels and lubricants. Reducing the number of oil injected machines by increasing the share of oil free machines would greatly contribute to realisation of these goals.

1.1 Clearances and leakage flow in PDMs

In rotary positive displacement machines, rotors are contained inside the stationary casing. It is necessary to maintain the gap between rotating and stationary parts to achieve reliable operation of the machine. Precise manufacturing of rotors enables these gaps to be very small (i.e. around 20 microns). However, these cannot be reduced to zero and therefore working fluid can still leak through the clearance gap from the higher to lower pressure creating leakage flows, Figure 1.3. Figure 1.4 [6] shows the location of various leakage paths present in a rotary screw machine and two-lobe roots blower. Six different internal clearance paths are identified by Fleming [7] inside the helical screw compressor, who also described the quantitative effect of each leakage on volumetric efficiency. They also stated that three leakage paths are most important, the contact line, the rotor tip sealing line, and the cusp blow hole. Reliability and performance are functional characteristics of the compressor that are strongly dependent on the operating clearances. Clearance height and operating parameters such as pressure ratio, operating speed and ambient condition can directly affect the volumetric efficiency and isentropic efficiency of the machine [8]. High pressure chamber gas leaks back to the inlet tract through the clearances can raise the temperature and thus lower the density of the incoming fresh air. Therefore, the mass of air trapped in the pocket gets reduced and, also, high pressure

chamber air temperature is increased. The latter effect generates thermal expansion in the rotors, affect the size of the working clearances and hence change the leakage flow rate, either increase it or decrease it depend upon the thermal expansion. So, leakage flow directly affect the volumetric efficiency and adiabatic efficiency of the machine and it becomes important to reduce the leakage losses in the PDMs.

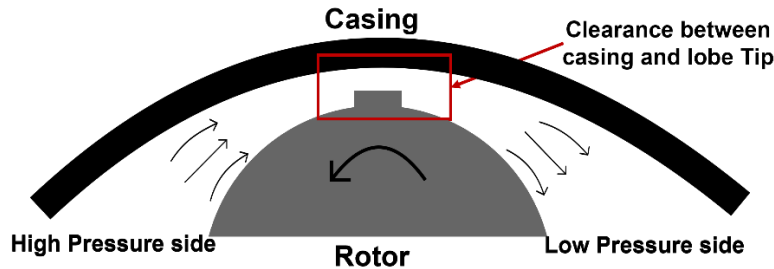


Figure 1.3 Representation of clearance between Rotor Tip and Housing

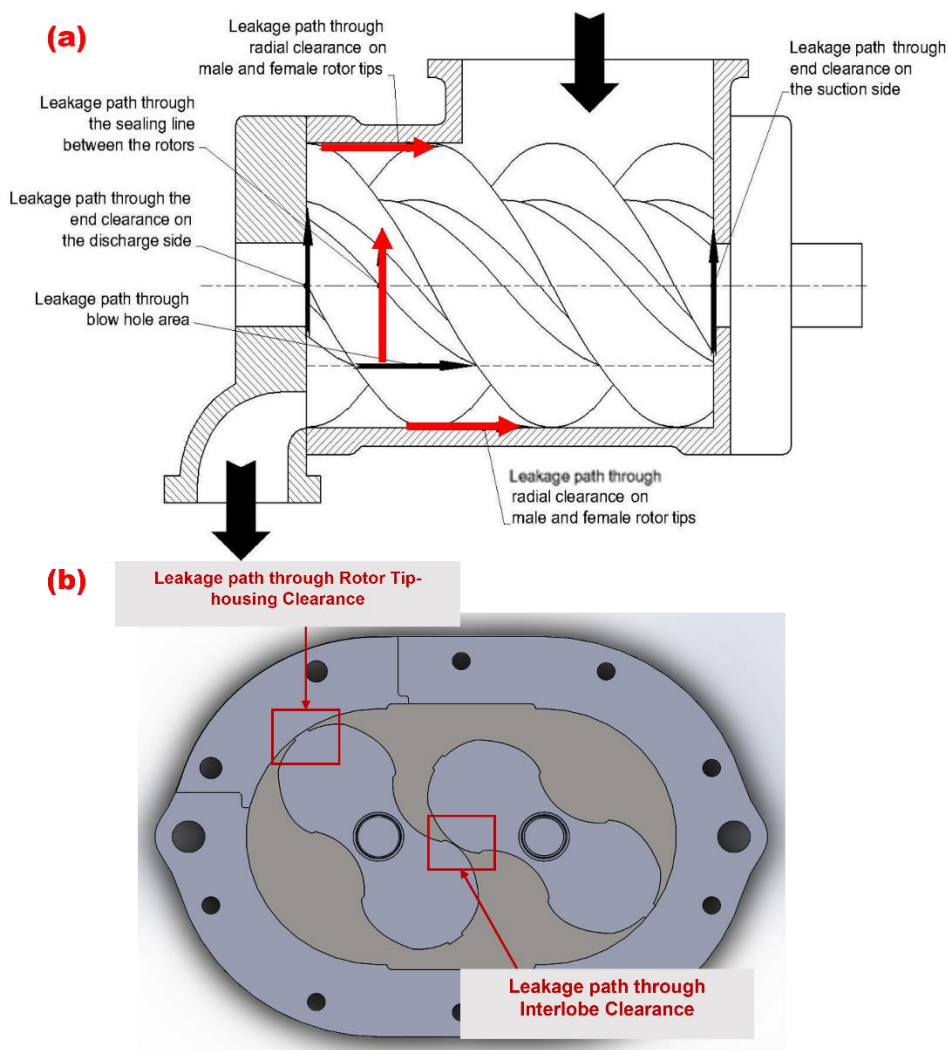


Figure 1.4 (a) Various leakage paths in rotary screw machine and key contributors are highlighted with red arrows [6] (b) Various leakage paths in Roots Blower

Representation of 2D rotor tip – housing clearance is shown in Figure 1.3, where gas flows from high pressure chamber to low pressure chamber. Inside these clearances, the nature of flow depends on the several factors such as, i) the pressure ratio across the gap, ii) the gap size, iii) type of fluid, and iv) the motion of the boundary. This complex flow is captured by Sachs [9] using schlieren method in static prototype of rotor and housing gap as shown in Figure 1.5. This gives a clear picture of complex flow phenomena present inside the clearance in a stationary condition.

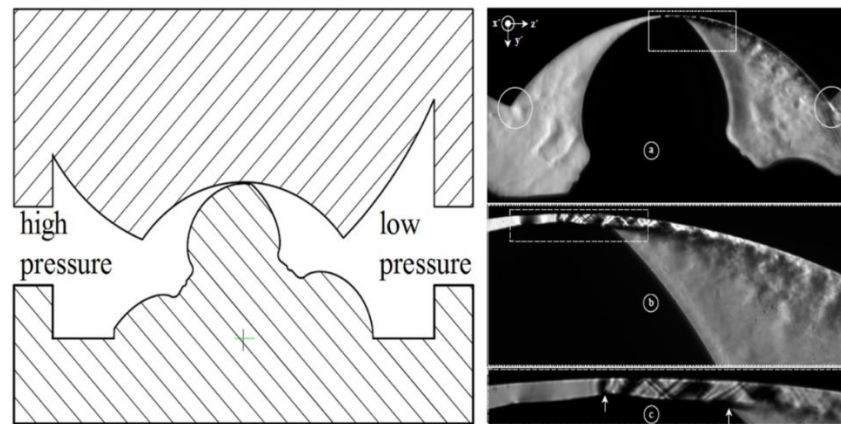


Figure 1.5 Clearance flow investigated by Sachs using schlieren method[9]

1.2 Heat transfer in clearances

In PDMs, the discharge temperature increases with the increase in the discharge pressure. In oil-free machines pressurized gas which has higher temperature leaks through the clearance gaps to the low pressure region. As shown in Figure 1.6, heat transfer can take place from fluid to solid. In complex transonic flows, the interaction between the shock wave and heat transfer commonly exists in different situations [10].

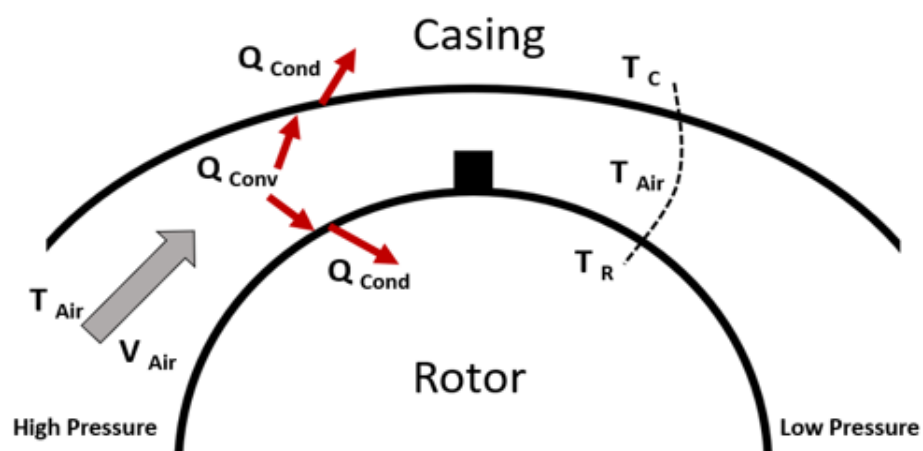


Figure 1.6 Generalized heat transfer concept in clearance

Conjugate heat transfer between fluid and solid walls is an important issue and it is challenging to model especially with complicated interfaces. It is found in many engineering industrial applications such as microscale cooling schemes for microprocessor chips, conventional internal combustion engines, heat exchangers, compressors and expanders. The ‘conjugation’ effect occurs when the temperature fluctuations in both the solid domain as well as the fluid domain become important in the solution of the heat transfer problem which makes unsteady heat transfer more of a challenge.

1.3 Thesis outline

The aim of this thesis is to evaluate experimental techniques to study leakage flow and heat transfer in the clearance gaps of rotary positive displacement machines (PDM) and to understand the main options to reduce leakages and improve reliability of PDMs by studying conjugate heat transfer (CHT) in leakage gaps of an industrial Roots blower. New experimental setups, measurement procedures and experimental results are presented. Thesis is structured as follows.

In chapter 1, introduction of rotary positive displacement machines, description of leakage flow and heat transfer in leakage flow are presented.

In chapter 2, literature review related to leakage flows and heat transfer in clearances is carried out, also various experimental techniques are studied here. The review of experimental methodologies has assisted to identify three useful techniques to visualize flow field and temperature in the clearance of these machines such as Planar Laser Induced Fluorescence (PLIF), Infrared Thermography (IRT) and Particle Image Velocimetry (PIV).

Chapter 3 outlines the aim, objectives, and methodology of the current study.

Chapter 4 describe the experimental setups and procedures in detail for PLIF, IR thermography and PIV methods.

In chapter 5, measurements are presented along with post processed results for PLIF, IR thermography and PIV methods.

Chapter 6 describes the analysis of flow field measurement inside, at the exit and the entrance of the clearance. It also presents the temperature over the lobe surface and conjugate heat transfer analysis.

Chapter 7 describes the conclusions, recommendation for future work and contribution to knowledge of the current study.

Chapter - 2 Literature Review

This study concentrates on understanding of the leakage flow and conjugate heat transfer in clearance gaps of positive displacement machines. With advanced manufacturing, nowadays small clearances between the stator and rotors can be achieved but these cannot be reduced to zero. Changes in clearance size during the operation of the machine plays a vital role in the performance of PDMs. The flow through the tip leakage gap is driven by the pressure difference on two sides of the gap. Fluid on the high-pressure side is drawn along the lobe and into the tip gap, as shown in Figure 1.3. This tip leakage flow is affected by inlet, outlet and surface boundary conditions and the relative motion of the lobe can affect the flow structure inside the gap and the total leakage flow rate. Apparently, in running conditions the complexity of leakage flow increases because fluid which passes through clearances is at increased temperature which reduces through clearances due to pressure reduction. This interaction of flow-heat-solid can affect the flow dynamics in clearances. In PDMs, especially in screw compressor application, heat transfer can be detrimental to the machine reliability because the compression of fluid creates a non-uniform three-dimensional temperature field leading to local distortions [11].

This chapter reviews literature resources on various experimental and numerical work carried out to understand leakage flows. In addition, it reviews previous research findings on the heat transfer associated with leakage flows, as well as the potential experimental techniques which can be useful to get more insight into physics of flow and heat transfer within clearance gaps of rotating positive displacement machines.

2.1 Leakage flows

Reasonable efforts have been made in the past to study flow structure inside the clearance gaps of rotary machines. The Schlieren pictures of the gas flow at the housing gap with stationary gap boundaries are obtained by Sachs[9], he stated that flow is directly affected by gap boundary and flow separation inside the gap. Later computational fluid dynamics (CFD) simulation is carried out by Kauder [12] by considering schlieren experimental results obtained by Sachs as a reference. Different turbulence models like Spalart-Allmarus, Standard k- ϵ (Two-layer Zonal), Standard k- ϵ (Wall function approach) were examined with a view to discovering how accurately it can simulate the gap flow, Figure 2.1 shows the difference in simulation results obtained with different turbulence models.

Vimmr & Fryc [13] have presented a numerical simulation of the leakage flow between the moving rotor and housing of a screw compressor. As shown in Figure 2.2, there is no shock wave present at a pressure ratio of 2, which contradicts the experimental result obtained by Sachs. But it is worth noting that this simulation carried out at an angular velocity of 9000rpm.

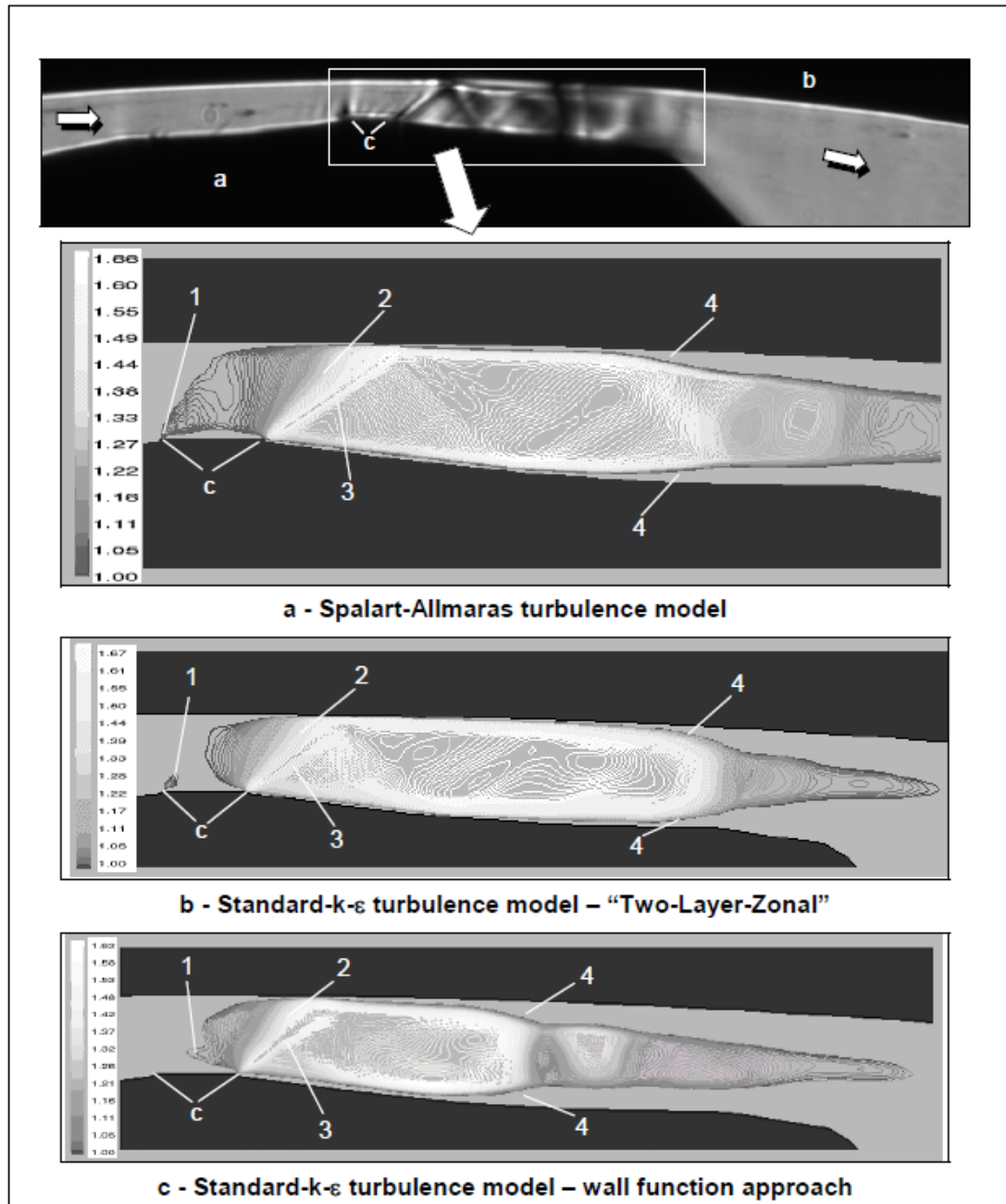


Figure 2.1 Simulation results for different turbulence models; pressure ratio 0.5, inlet pressure 2 bar; minimum clearance height 0.4 mm[12]

- 1 transition zone for transonic flow
- 2 expansion fan
- 3 oblique shock
- 4 separation and contraction

- a male rotor
- b casing
- c sealing strip

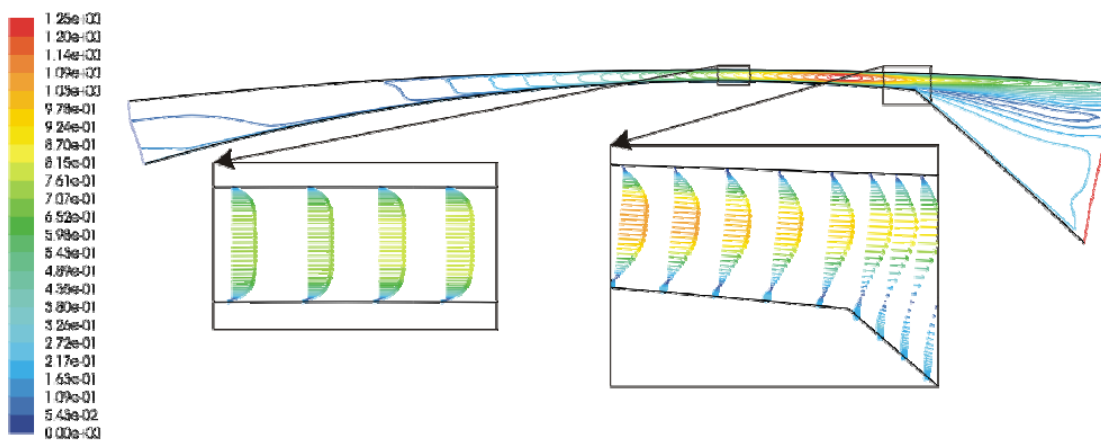


Figure 2.2 Contours of Mach number and velocity profiles in the male rotor-housing gap obtained by segregated solver using Spalart-Allmaras turbulence model on the finest grid of 178×68 cells for the angular velocity of 9000 rpm [13]

Guerrato et al. [14] measured the flow field in the working chamber near the discharge chamber and in the discharge chamber of oil-free compressors using laser doppler velocimetry. While as shown in Figure 2.3, flow visualization at the suction of twin screw compressor was carried out by Kovacevic et al. [15] using high speed camera, the effect of water injection into the airstream at the inlet of an oil-free screw compressor was analysed using CFD and experimental data obtained using High-speed camera. CFD models are validated using experimental data.

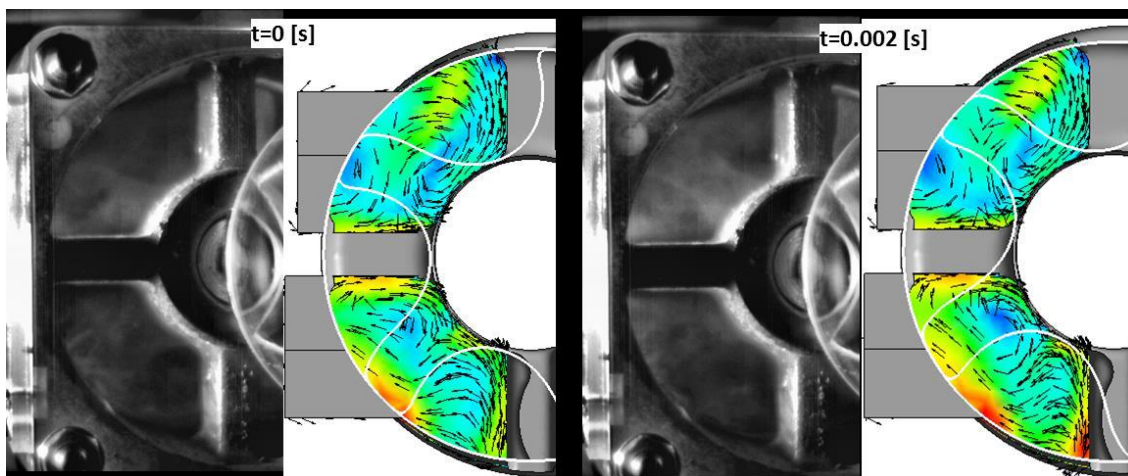


Figure 2.3 High speed camera and CFD comparison for the gate rotor [15]

The influence of rotor deflection upon screw compressor performance was studied by Kovacevic et al. [16]. The compression process within screw compressors induces large pressure and temperature changes that cause the rotors to deform. This led to the development of a 3-D numerical method to study Fluid Solid Interaction (FSI) which has

been used to calculate flow and deformation simultaneously. Buckney [17] looked into the thermal distortion of the casing and rotor in order to improve the efficiency of screw compressor. A validated procedure was developed to enable a chamber model to predict compressor performance while including the effects of rotor and casing distortion resulting from dependent thermal effects. A new approach of injecting a small quantity of flashing liquid (i.e. water) in dry screw compressor is introduced by Stosic et al. [18] to control discharge temperature of oil-free compressor and to operate it at higher pressure ratios in single-stage machine. Thermal expansion is studied by Daemgen et al [19] by measuring the temperatures in the rotor teeth for 22kW oil-injected screw compressors and they had extrapolated this data for larger rotors. They conclude that the temperature difference between the rotor tooth and casing is lower than the expected for medium-size oil-injected screw compressors, and the main influence on temperatures is from the oil thermostat.

Extensive research has been carried out in the field of turbines related to leakage losses because it is a critical issue for this application, as it reduces the power extracted and generates aerodynamic mixing losses. The hot gas leaking through the clearance gap also tends to burn away the blade tip or attached shroud seal. The leakage flow over the front portion of the turbine rotor blade tends to be subsonic, and the reattachment of the pressure side bubble is driven by flow diffusion (A in Figure 2.4), which induces higher mass flow through the gap. The deceleration amplifies the turbulence, resulting in high heat transfer coefficients. Further on the blade the leakage flow typically reaches supersonic speeds (B in Figure 2.4) due to the combination of a high driving pressure ratio and the significant streamline curvature as the flow enters the pressure side of the tip gap [20].

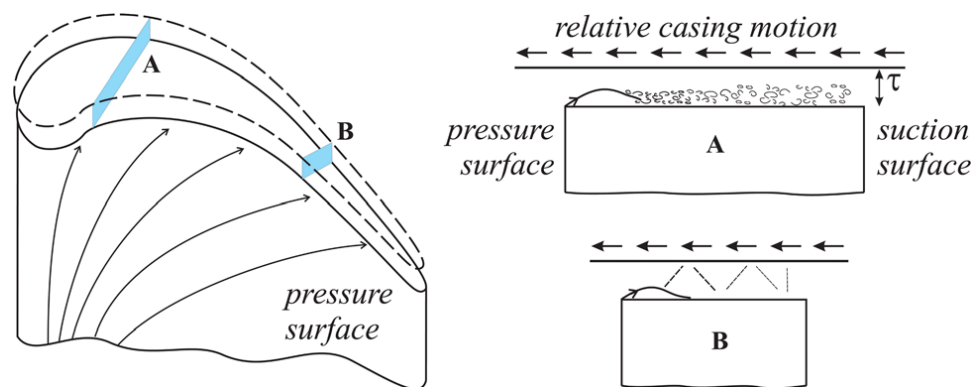


Figure 2.4 schematic of tip leakage flow, with cut planes showing low speed behaviour over the front of the tip (A) and high speed over the rear (B) [20]

Over tip choking and its implication on the turbine blade tip is presented by Zhang [21] using a Reynolds-averaged Navier–Stokes model (HYDRA). As shown in Figure 2.5, over tip leakage (OTL) flow pattern depends upon the pressure difference across the tip. The tip leakage flow accelerates, separates, and then mixes out at the tip-gap exit. At an exit Mach number of 0.37, Figure 2.5 (a) shows a typical over tip leakage-flow pattern without any shock formation for low-speed tip flows. Figure 2.5 (b) shows a qualitatively different flow feature at an exit Mach number of 1.01. These transonic flow features include a dramatic reduction in the size of the separation bubble, reflections of oblique shocks between casing and tip, thinning and thickening of the tip boundary layer, a normal shock at the tip-gap exit. The effective throat area for OTL flow decreases significantly as the separation bubble shrinks.

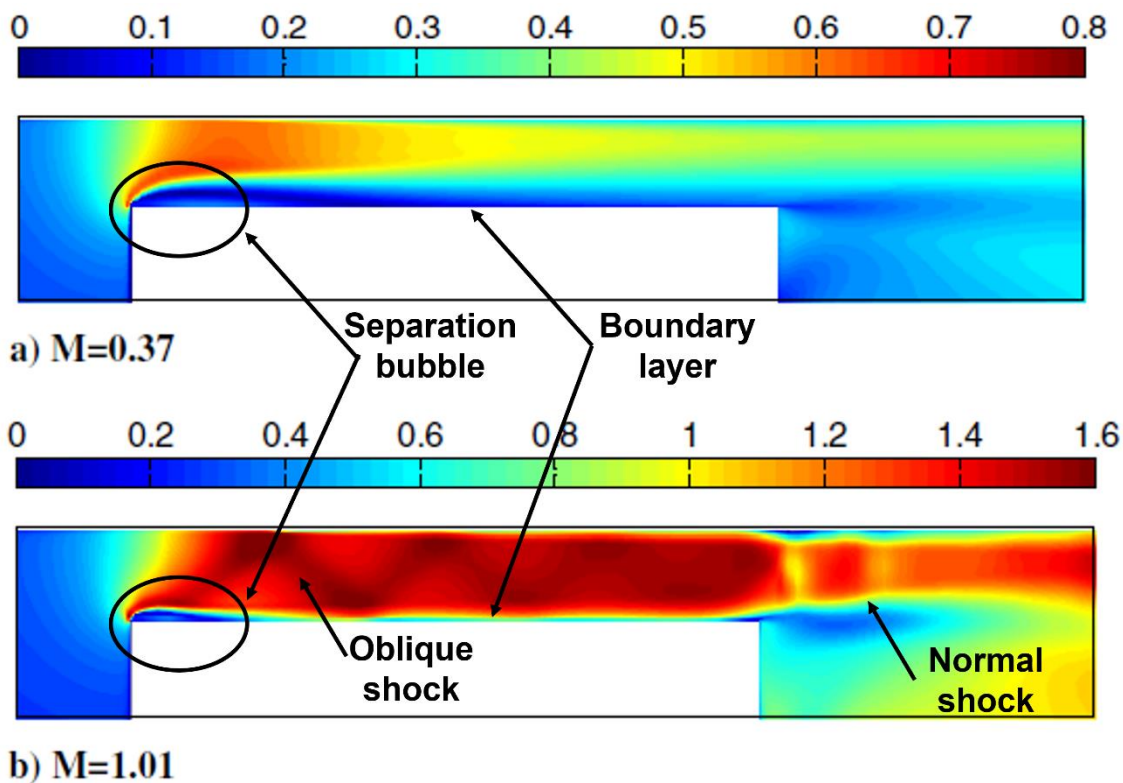


Figure 2.5 Mach number contours along an axial cut plane for subsonic and transonic tip flow: a) $M = 0.37$ and b) $M = 1.01$ [21].

In 1941, Kolmogorov proposed two hypotheses stating that real turbulent flows are practically locally homogeneous and isotropic and thus universal on small scales regardless of their inhomogeneities and anisotropy at large scales. Spectral analysis can conveniently separate different spatial scales and thus is essential for dealing with turbulence problem. Energy spectrum can be used to check whether employed technique is able to resolve the inertial subrange or not. It also indicates the nature of the decay of

the turbulence energy. Study of unsteady structure of compressor tip leakage flows shows that the flow at the exit of the tip showing a convergence towards the Kolmogorov $-5/3$ cascade [22].

Recently, a study is carried out by Singh et al. [23] using optical visualization and unsteady Reynolds-Averaged Navier Stokes (URANS) computational modelling methods while focusing on investigating the transient flow field inside a Roots blower. In this study, low-speed experimental investigations are carried out using three different experimental methods like High-Speed Camera (HC), continuous High-Speed Particle Image Velocimetry (CPIV) and instantaneous PIV (IPIV) obtained with a double pulse laser and a double frame camera. Tests were performed at the speeds of 464rpm and 625rpm, operating at pressure ratios between 1.06-1.07 bara. Figure 2.6 shows a comparison of flow field obtained by PIV measurement and CFD analysis at various rotation angles of a lobe. It is observed that experiments and CFD simulation both were not able to get the flow field inside the clearance between lobe tip and casing.

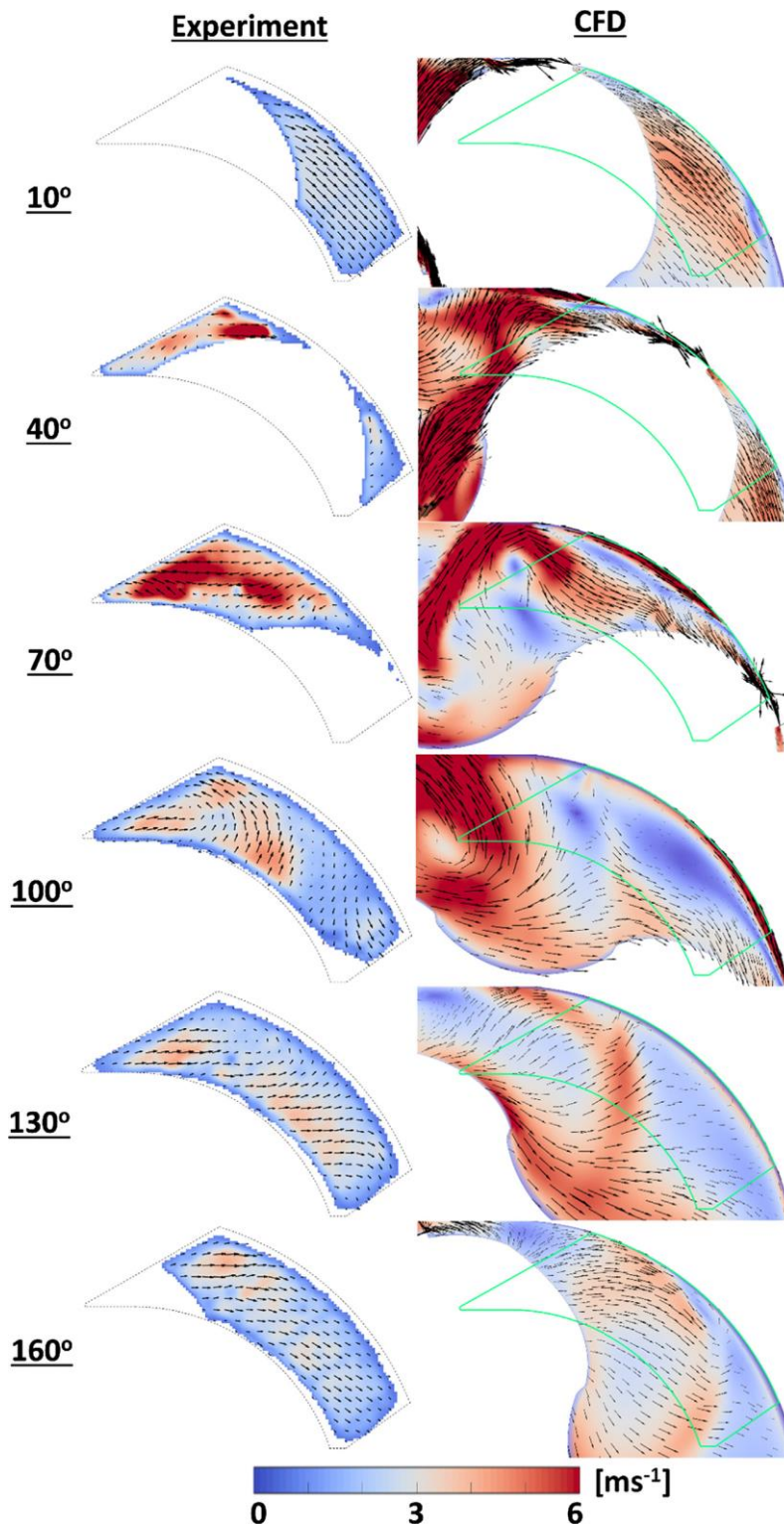


Figure 2.6 Comparison between the PIV results and CFD results at various crank angle positions and 625 rpm rotor speed [23]

It is observed that out of the three analysed methods, the IPIV technique is the most suitable to capture the Roots blower flow field. However, it was not able to resolve flow features in regions near gaps and walls. The study also revealed that leakage flows impact both, three dimensionality and turbulent mixing in a Roots blower. Vortices generated by

the axial and inter-lobe leakage flows cause high mixing in the flow. The axial leakage generates a strong corner vortex on the rotor edges. This induces highly three-dimensional flow in the trailing low-pressure chambers. Very recently, the three-dimensional unsteady CFD model of the Roots blower with the dynamic grids generated by SCORG (Screw Compressor Rotor Grid Generator) was established to predict the gap flow [24], CFD model shows the same flow pattern but overestimating the leakage flow velocity. The variation of velocity profile along the tip gap under the pressure ratio of 1.015 (left) and 1.072 (right) can be seen in Figure 2.7.

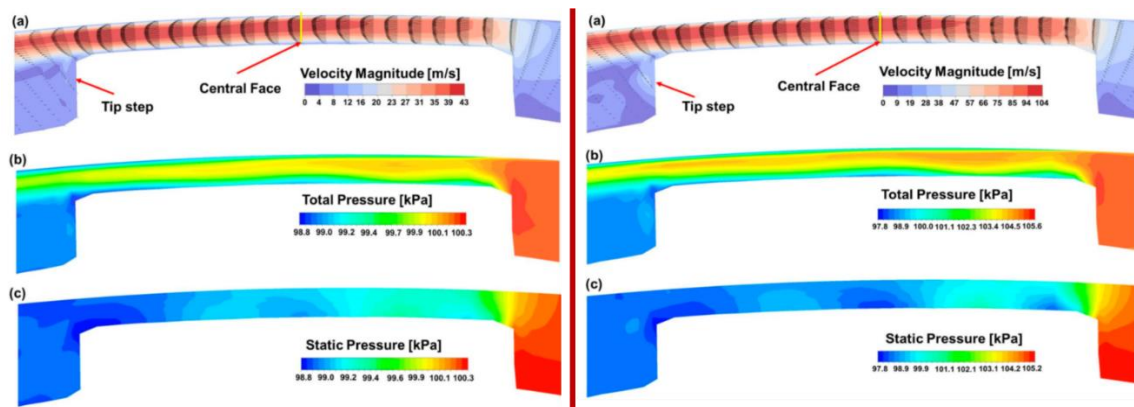


Figure 2.7 The velocity and pressure distribution in the tip gap at the crank angle of 43° under the pressure ratio of 1.015(Left) and 1.072(Right): (a) velocity field, (b) Total pressure, (c) Static pressure[24]

At the pressure ratio of 1.072, the variation of the velocity profile, the total pressure and the static pressure are similar to that at the pressure ratio of 1.015. The maximum velocity increases from 43 to 104 m/s due to the increase of pressure ratio. The average velocity at the central face can be calculated by performing integration over velocity profile. Their values are 33 m/s and 76 m/s under the two pressure ratios respectively. It is interesting to note that the rotor velocity also influences the shape of the velocity profile.

2.2 Heat transfer in leakage flows

The gas compressed in positive displacement machines is heated on the high-pressure side by the compression process. The gas temperature is typically higher than the rotor and casing. The flow of heat from gas to rotors and casing is shown in Figure 1.6. According to Roland Muller [25], in the case of the laminar flow regime through the clearance gap and $T_{gas} > T_{Rotor \& \ Casing}$ immediately behind the entrance of the gap, the gas on the walls on the respective wall temperature cools. In another run, heat is flowing from the hotter inner layers of gas towards the wall by heat conduction in the gas so that

the gas cools slowly in the centre of the gap. In the case outlined here the cooling on the housing side due to the higher temperature gradient is stronger, which has an asymmetric temperature profile as shown in Figure 2.8. In the other part of the cycle, the temperature gradient is reversed, and the rotor heat is extracted from the wall and introduced into gas.

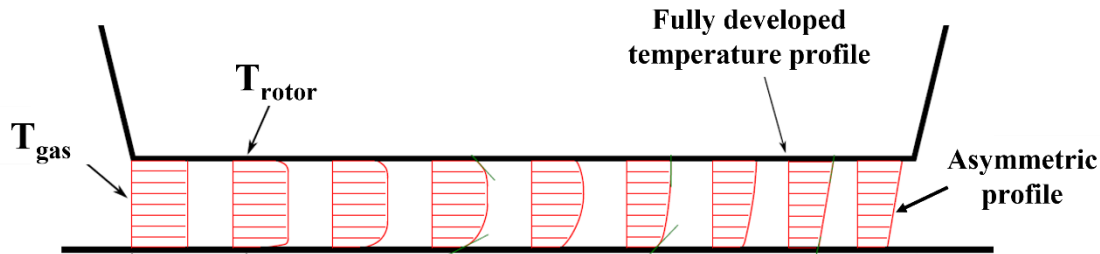


Figure 2.8 Temperature profile in clearance between rotor and casing for laminar flow for the case $T_{\text{gas}} > T_{\text{Rotor \& Casing}}$ [25]

For fully developed turbulent flow the temperature profile with the same thermal boundary conditions is similar. However, due to the turbulent motion of the fluid, the thermal conductivity in the gap centre is apparently increased, see Figure 2.9. The temperature gradient at the wall is significantly higher than in the laminar case, resulting in the increased heat exchange between the two components.

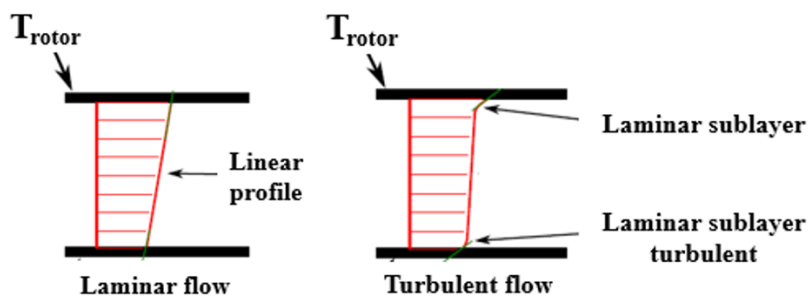


Figure 2.9 Comparison of fully developed temperature profile of laminar flow and turbulent flow [25]

Because of the compressibility of gases, for large pressure gradient, the density of the gas varies significantly in the flow field, which is expected to cause significant influence on the flow and heat transfer. In addition, friction in the compressible flow region can play a vital role.

Over tip leakage flow in the gap between the rotor blade and casing in the turbine has been the focus of turbomachinery research community over the past decades because of

high pressure, high temperature, and high-speed operating conditions. Zhang et al. [10] reported detailed experimental evidence of the heat transfer stripe distribution caused by shock wave structures over the tip in turbines. He stated that the supersonic part of tip experiences noticeably lower heat transfer than that near the leading-edge where the flow inside the tip gap remains subsonic. Near the pressure-side corner, the flow accelerates, and an oblique shock wave originates near the separation bubble. This is observed from all four cut planes in Figure 2.10. The flow continues to accelerate between the reflections of the oblique shock wave between the casing and the tip. A normal shock wave is generated immediately afterwards as the flow passes the blade tip gap. The resulting shock-boundary-layer interaction contributes to further enhancement of heat transfer to the blade tip near the shock foot.

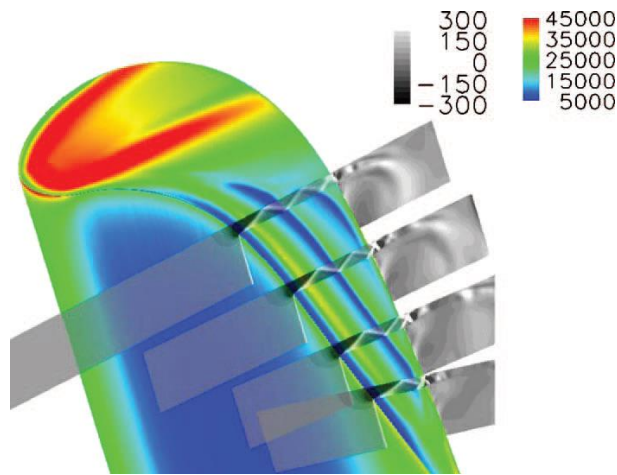


Figure 2.10 Tip surface heat flux(W/m²) and X-components of density gradient (kg/m²) distributions on four cut planes (HYDRA Prediction) [10]

The question important for understanding the heat transfer over the turbine tip is “Is the over tip leakage aerodynamics significantly affected by the wall thermal condition?”. The numerical analysis the study of Zhang and He [26] reveals that the wall–gas temperature ratio could greatly affect the transonic OTL flow field and there is a strong two-way coupling between aerodynamics and heat transfer. The change in the temperature ratio brings more profound differences in the transonic flow regime. Figure 2.11 presents Mach number distributions for a wall–gas temperature ratios (TR) of 0.92 and 0.63 on the cut plane of a tip surface as shown in Figure 2.10. In common, typical transonic OTL flow features are shown for both TRs, including pressure side edge flow separation, oblique shock reflections and normal shock at the tip–gap exit. For the lower TR case, the normal shock wave occurs further downstream (close to the exit of the tip gap). Figure 2.11(b)

also shows that the multiple reflections of the oblique shocks are more evident for the case with TR of 0.63. The same thing is validated by experiments as well [27].

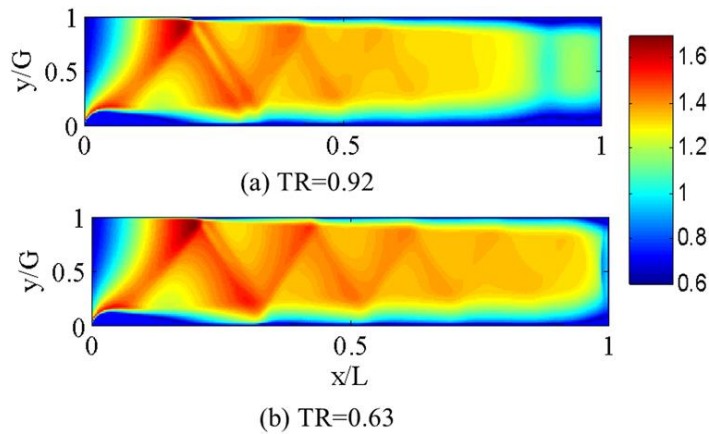


Figure 2.11 Mach number distributions on cut plane B (transonic region) for (a) TR = 0.92 and (b) TR = 0.63

Flow field and heat transfer inside the leakage flow shows the presence of conjugation. Conjugate heat transfer (CHT) is frequently described as heat transfer between a fluid, and a solid in which the interface condition is initially unknown and is found from the heat transfer solution. Conjugate is defined as “joined together” or “coupled”. Most heat transfer problems consider thermal interactions between a fluid and a solid, CHT is widely considered to be modelling convection without using a convective heat transfer coefficient [28].

Perelman [29] deals with the simplest “conjugated” boundary value problems of heat transfer in which heat conduction equations are solved in common for a body with heat sources and for a liquid flowing around the body. The method of the asymptotic solution of integral equations occurring in conjugated problems is presented. A numerical model is developed by Chiu [30] to calculate conjugate heat transfer in flow over a horizontal heated channel. The developed model was validated with experimental results. This study shows that conjugate heat transfer significantly affects the temperature level and uniformity at the heated surface, channel wall and gas phase, thus impact the rate of heat transfer. A fully conjugate heat transfer analysis of gaseous flow, within slip flow regime, in short microchannels is carried out by Croce [31]. The main focus is on the interaction between compressibility and heat transfer and a semi-analytical solution based on differential transform method is presented for solving the non-linear integrodifferential equation occurring in the problem Joneydi [32]. The main conclusion is that in the conjugate heat transfer case the temperature distribution of the plate is flatter than the one

in the non-conjugate case. This feature is more pronounced under turbulent flow when compared with the laminar flow.

2.3 Velocity field, temperature field and surface temperature measurement

This study emphasises to obtain the velocity field and temperature field inside the clearance of rotary PDMs as well as temperature information of rotary and static elements. To obtain velocity and temperature field, optical measurement is the most suitable approach. Various techniques are explored to get velocity field, temperature field and surface temperature of moving object. Various temperature and velocity measurement techniques suitable for current application such as schlieren technique, particle image velocimetry (PIV), infrared thermography, Planar laser induced fluorescence and Holographic interferometry are studied to identify appropriate technique for velocity and temperature field visualization.

2.3.1 Measurement of velocity field

Flow field measurements play a crucial role in understanding the behavior of fluid dynamics in various systems, ranging from microfluidic devices to aerospace engines. In the case of micrometer-sized clearances, such as those found in the operating conditions of rotors, obtaining accurate velocity data is particularly challenging. Measuring the velocity flow field within micron-sized clearances under the operational conditions of a rotor presents a significant challenge.

The Schlieren method is one such technique used to visualize and quantify flow patterns within narrow gaps. It relies on the principle of light refraction, where variations in the refractive index of a fluid cause bending of light rays passing through it. By exploiting this phenomenon, the Schlieren method can provide insights into the velocity flow field within micron-sized clearances.

On the other hand, Particle Image Velocimetry (PIV) has emerged as a powerful non-intrusive technique for measuring velocity fields in various flow regimes. PIV utilizes the motion of tracer particles suspended in the fluid to track flow patterns and calculate the velocity at different locations within the clearance.

2.3.1.1 Schlieren method

In fluid dynamics, Schlieren imaging is a commonly used tool. With this technique, air flows and shock waves can be depicted in detail which led to extensive use of this technique in aerodynamical studies [33]. The measuring-principle of the schlieren technique is based on the deflection of a collimated light beam crossing gradients of the index of refraction in a transparent medium. It is, therefore, suited for applications in which deviations of light are intended to be visualized as they appear e.g., at refraction gradients due to density-discontinuities in a fluid.

Using a Schlieren system combined two-dimensional temperature and velocity measurements can be done in liquid and gas flow. Temperature measurements can be made by relating the intensity level of each pixel in a Schlieren image to the corresponding knife-edge position measured at the exit focal plane of the Schlieren system. The same Schlieren images can be used to measure the velocity of the fluid flow. Attraction to use the Schlieren technique for measuring temperature of the flow is due to its relatively easy implementation, low cost, use of conventional light sources, and a high and variable sensitivity. As shown in Figure 2.12, classical schlieren systems include a point-like light source, usually a xenon flash lamp. The light from the source is collimated by a lens, which is at least as large as the object being analysed. After the collimated beam passes through the test section, it is refocused by a second lens. A knife-edge is then placed at this focal point, which is the exit focal point of the lens system array. When the knife-edge is placed horizontally, positive density gradients are visualized as light areas and negative gradients as dark ones. The reason is that the light rays deflected upwards by the positive gradients miss the knife-edge, whereas those deflected downwards by the negative gradients are blocked out by the knife. [34]

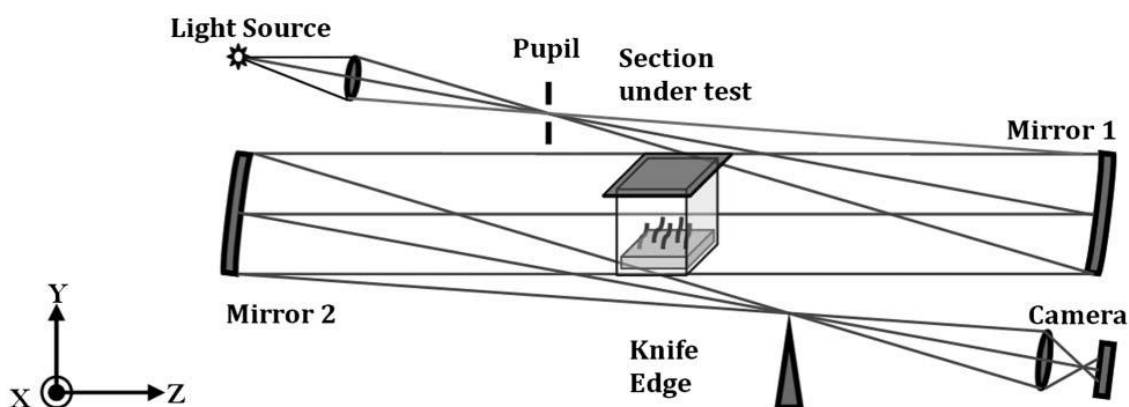


Figure 2.12 Schematic of a parallel-light Z-type schlieren system [34]

A review of various schlieren instrumental setups [35] suggest that this technique requires throughout transparent medium, which is not suitable for geometry of current Roots blower machine. Therefore, it is difficult to employ this technique for current research.

2.3.1.2 Particle Image velocimetry

PIV is a non-intrusive optical velocity measurement technique yielding planar whole field quantitative measurements of instantaneous and mean velocity. Improvements in laser and digital imaging techniques have significantly enhanced the ability of PIV. Traditionally PIV has found its application in low-speed flows. However, this technique is extended to high-speed compressible flows, which is made possible with high energy short pulse lasers and cameras with very short interframe time [36]. PIV determines a velocity field by tracking the average motion of particle groups from a pair of images that are separated by a known time delay. Each image is divided into a grid of regularly spaced interrogation windows. An algorithm computes the cross-correlation function for all interrogation windows, resulting in one displacement vector per interrogation window and therefore produces a regular grid of vectors. Advancement in the image post processing algorithms has widened the dynamic range of PIV [37]. Dividing the displacement vector field by the time delay determines the velocity vector field. The schematic of PIV is shown in Figure 2.13. The PIV technique requires the flow-field to be seeded with small particles which accurately follow the flow. A dual-pulse laser is used to illuminate a thin sheet of the flow with a short time delay, Δt , between the two pulses. The light scattered by the seed particles is recorded by a double shutter camera, in this case a camera with a sCMOS sensor, positioned normal to the laser sheet. By prescribing the time delay between pulses (Δt) and measuring the particle displacement (Δx) between the two recorded images, the velocity field can be computed as $\Delta x/\Delta t$. In practice the particle displacement is computed by dividing the recorded image into sub-areas called Interrogation Windows (IW). The in-plane displacement of the particles in each IW is obtained using statistical image cross-correlation. A velocity vector map over the whole image area is obtained by repetitive cross-correlation and velocity calculation for each IW. A detailed description of the PIV technique is given in a book by Raffel [38].

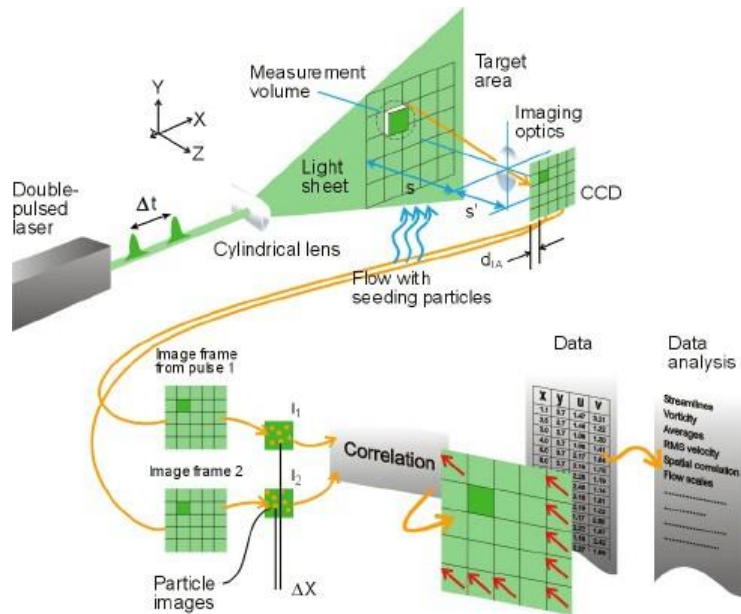


Figure 2.13 PIV measurement principle (Image from Dantec Dynamics [39])

PIV seems suitable for the current application as it requires optical access from two side of the flow field. To apply PIV for the flow visualization in clearances of the Roots blower, it is possible to get optical access to a clearance, to seed the particles and to illuminate flow using the laser.

2.3.2 Measurement of temperature field

Optical methods allow temperature measurement without direct physical contact with the object or the need for invasive sensors. This non-contact nature ensures that the measurement process does not disturb the thermal equilibrium of the system under investigation, making it suitable for sensitive or delicate objects. Information of temperature inside the clearance is useful to understand the heat transfer process inside the clearance. Two optical measurement techniques used for temperature field analysis are explored: Planar Laser-Induced Fluorescence (PLIF) and Holographic Interferometry. PLIF is a powerful method for visualizing temperature distribution within clearance gaps. On the other hand, Holographic Interferometry provides accurate visualization of temperature fields in transparent objects, without the need for additional particles or probes.

2.3.2.1 Planar laser induced fluorescence (PLIF)

Laser diagnostics are widely used in fundamental combustion science, research and development to investigate transient phenomena without influencing the system under study [40]. Laser induced fluorescence (LIF) of a “tracer” added in small amounts to a

non-fluorescing surrogate fluid has become the tool of choice to image heat-transfer phenomena [41]. The objective of the LIF imaging in this work is to provide two-dimensional measurements of the temperature within the clearance gap of the Roots blower. LIF is a powerful technique for nonintrusive visualization of concentrations in the mixing of gaseous and liquid flows and for gas-temperature imaging. It is used in industrially relevant applications like internal combustion (IC) engines [41]. Most work pertains to fluids with excitation by a pulsed UV laser where it is relatively straightforward to obtain sufficient LIF signal for qualitative visualization of the fluid. Fluorescent organic species [42] are the most commonly used tracer group for imaging applications via laser-induced fluorescence in, e.g., gaseous flows or IC engines during the compression stroke.

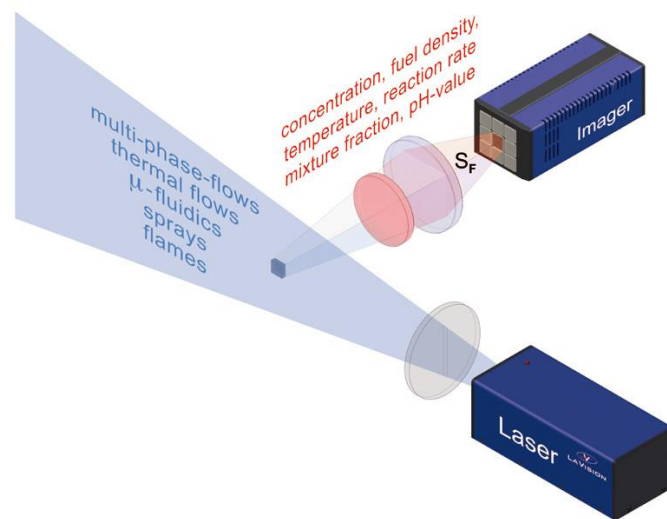


Figure 2.14 Basic imaging setup for LIF technique (LaVision)

As shown in Figure 2.14, a laser beam is formed into a light sheet which intersects the fluid area of interest, e.g. in flames, sprays or thermal flows. The resulting fluorescence light from excited molecules in the light sheet is imaged through a selective filter onto a time-gated digital camera. For pulsed ultraviolet LIF applications, usual practice is to use an image intensifier to amplify the LIF signal. The conversion of LIF images into meaningful concentration or temperature fields is based on calibration measurements. This system normally includes instruments like laser source e.g. Nd YAG Laser, imaging camera e.g. Charge-coupled device (CCD) or Complementary Metal Oxide Semiconductor (CMOS) cameras, Image intensifier, lenses as per requirement and computer system. The temperature of the fluid film can be determined using a LIF

technique, and the temperature and heat flux at the fluid-solid interface can be determined by making IR temperature measurements as shown in Mathie [43].

It is necessary to check the feasibility of this method in the current focus of leakage flow since this method is not used in past to study temperature distribution in small clearance gaps. Feasibility study of PLIF technique presented in this thesis is carried out in collaboration with LaVision GmbH, Germany.

2.3.2.2 Holographic Interferometry

Holographic interferometry is an optical visualization method ranked among the most accurate for research of inhomogeneities of transparent objects. A great advantage is that other particles or probes, which might influence the flow, are not added in the observed area. Interferometry is based on the principle of a wave phase change when switching through a nonhomogeneous transparent object. The phase shift can be visualized by the interference fringes by comparing a light beam that passes through the object and a reference light beam. [44]

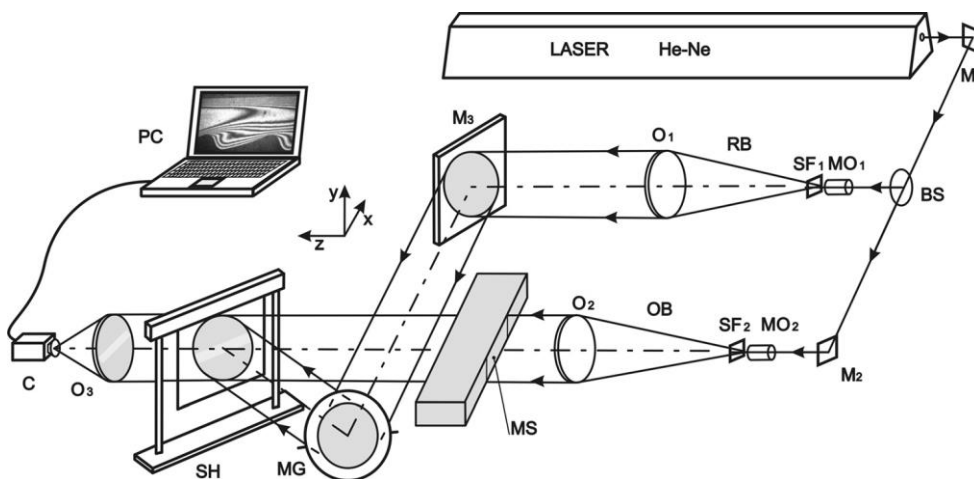


Figure 2.15 Schematic of holographic interferometer [44]

Schematic diagram of holographic interferometry is shown in Figure 2.15. This method also requires laser source, camera, lenses, filters, computer system and specifically a transparent object. In the past, this method was used to visualize temperature fields in the vicinity of two parallel plates. Possibility of the measurement of a temperature field generated by heated fluid from a synthetic jet (SJ) actuator is shown by Dancova et al [45]. Digital holographic interferometry (DHI) was the main measuring method used for the experiments. A single-projection DHI was used for the visualization of the temperature field as an average temperature along the optical axis. Herman et al [46]

presented holographic interferometry combined with the high-speed cinematography to visualize the unsteady temperature fields in self- sustained oscillatory flow.

Holographic interferometry, although a highly accurate optical visualization method, not suitable for the current application due to the requirement of a transparent object. Since the focus is on studying temperature distribution in small clearance gaps, a transparent object that allows for the necessary phase shift visualization is not available.

2.3.3 Surface temperature measurement

Temperature measurement of the lobe surface of the optical Roots blower using conventional temperature measurement technique such as use of thermocouples and RTDs [47] or by thin film sensors are possible but it is very complex and can give only a handful measurement points. This is not suitable for measuring the temperature of the entire lobe surface in operation which is needed for the current application. Therefore, another solution for non-intrusive experimental techniques is required. IR thermography has been widely used for surface temperature measurement and it provides an effective approach for non-intrusive and spatio-temporal measurement of temperature [48], and it can overcome the limitations of traditional measurement methods. Liquid crystal thermography can also be used to measure the surface temperature, but it also required the thermochromic liquid crystal coating on the surface and imaging of the change in the colour of the coating [49].

2.3.3.1 Infrared thermography technique

All objects with surface temperatures above absolute zero emit electromagnetic radiation and the surface temperature of the object can be determined from the wavelength and intensity of electromagnetic radiation emitted in the infrared region of the spectrum [50]. To determine temperatures accurately with IR Thermography, careful attention towards a proper choice of windows, elimination of specular reflections from channel walls, and estimation of local emissivity changes are required. As shown in Figure 2.16, IR thermography involves the infrared camera and optical lens.

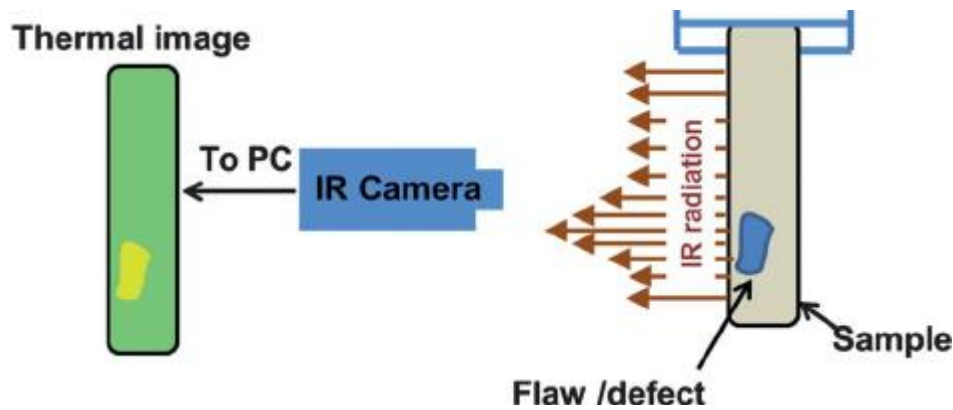


Figure 2.16 Basic setup of IR thermography

The bodies occurring in real life show very diverse radiation properties. Therefore, it has proved worthwhile to initially consider the simplified laws of a model body of ideal radiation properties to be then applied to occurring objects. This model body is known in radiation physics as the “black body”. It distinguishes itself by the fact that, of all bodies of equal temperature, it shows the largest possible emitted radiation. The spectral spread of radiation emitted by a black body is described by planck’s radiation law. Representation of radiation laws in Figure 2.17 shows that the spectral composition varies with the object temperature. Furthermore, it must be noted that, at each wavelength, radiation intensity increases with rising temperature. PLANCK’s radiation law represents the principal relationship regarding non-contact temperature measuring.

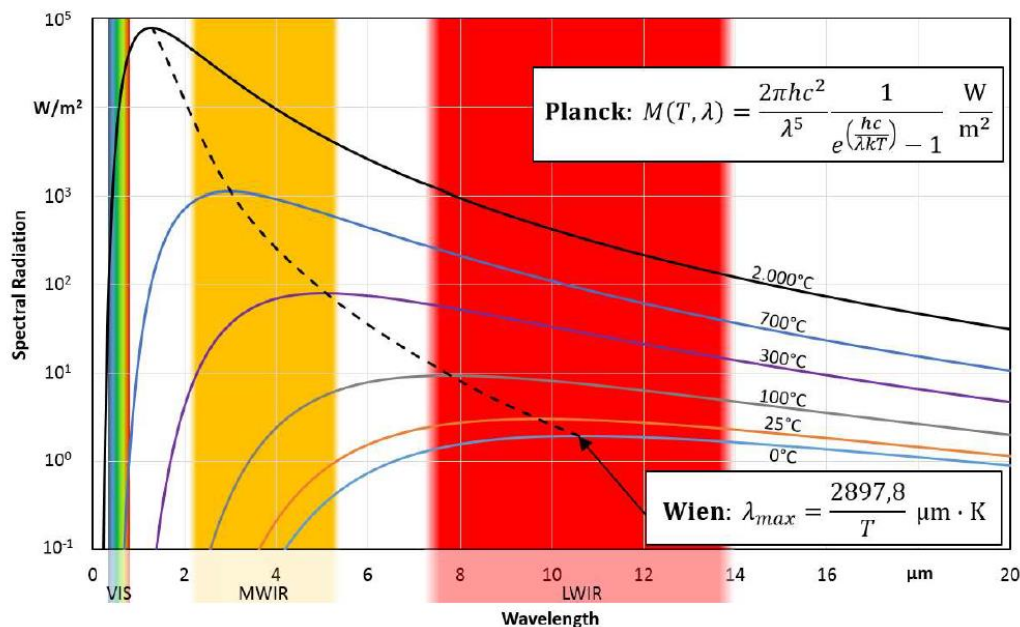


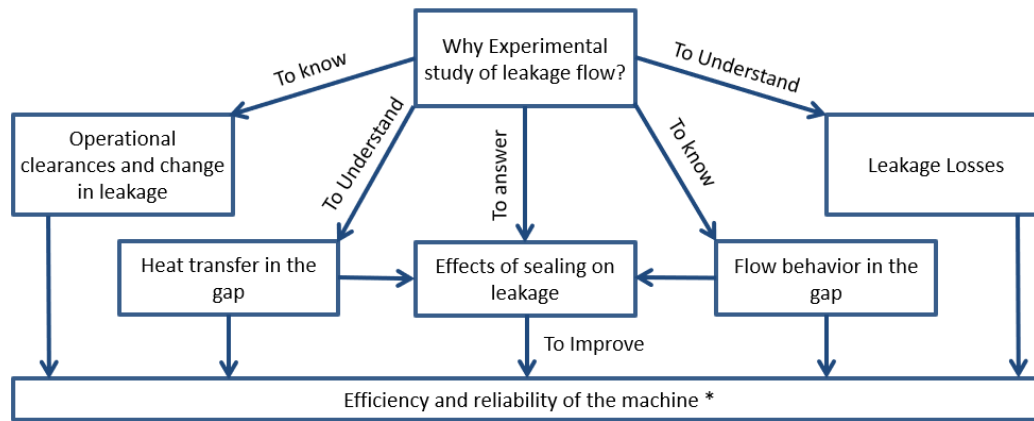
Figure 2.17 Planck’s Radiation Law & Wien’s displacement law

The recent advancement in infrared thermography cameras with better technical characteristics such as thermal resolution and dynamic range [51][52], make IR

thermography more accurate and suitable non-intrusive temperature measurement technique for application in Roots blower surface temperature measurements. Recent technology also facilitates the phase-locked detection of surface temperature [53] which is necessary in this application. Literature also shows the use of infrared thermography to study effect of conjugate boundary condition on heat transfer analysed by investigation of local temperature measurement [54]. Significant experimental work has been carried out to understand the turbine blade tip heat transfer and aerodynamics, these studies mostly employ infrared thermography to study the heat transfer over the turbine tip surface [55] and it indicates the reliability of this technique for surface temperature measurement. IR thermography is successfully used to investigate the flows in microchannels by T.L Liu and C Pan, and it is stated that IR thermography could measure transient temperature along the channel [56]. Therefore, IR thermography is most suitable method for this application, and is employed to measure the surface temperature of the lobe in running condition of the machine in this study.

2.4 Conclusion from the literature review

Literature shows that flow field inside the clearance gap of rotary positive displacement machines depends upon the pressure ratio across the gap, gap size, type of fluid, motion of a boundary also various flow structures such as shock, boundary layer and vortices are present. In addition, flow through leakage gaps involves convective heat transfer in the fluid part and conductive heat transfer in solid parts. If the conduction through the wall is not negligible, the conductive and convective heat transfer modes are fully coupled, in other words, the boundary conditions at the interface are important. So, heat transfer inside the clearance gap between gas and solid should be treated as CHT and the consideration and understanding of CHT is an important factor in Rotary PDMs. To understand the CHT inside the clearance gap it is necessary to study surface temperature behaviour of the lobe and flow field temperature of leakage flow during the operation of the machine. However, experimental data for the flow field, temperature field and surface heat transfer inside the leakage flow for positive displacement rotary machine are not available. It necessitates the gathering of experimental data. These data are necessary to understand flow-heat-solid interaction in the clearance gap to improve reliability of such machines by clearance management as a long-term goal. Importance of the leakage flow study in PDMs is illustrated in Figure 2.18.



* Global energy consumption by CAS is 10 – 15 % , So it is vital to pay attention to machines performances

Figure 2.18 Importance of leakage flow study in positive displacement machine

Among the various flow and temperature visualization techniques discussed in the literature, Planar Laser-Induced Fluorescence (PLIF), Particle Image Velocimetry (PIV), and Infrared (IR) thermography appear to be the most suitable for studying leakage flows in clearance gaps. PLIF can provide visualization of the temperature field in leakage flows, but feasibility needs to be verified since it has not been employed in similar applications before. PIV has the potential to visualize the velocity field in leakage flows, although visualizing the flow in micron-sized clearance gaps during machine rotation poses challenges. High-speed infrared thermography can measure lobe surface temperature during machine operation, but the rotating speed of the machine presents a challenge.

By employing these techniques and addressing the associated challenges, a comprehensive understanding of leakage flows in rotary positive displacement machines can be achieved, leading to improved machine reliability through effective clearance management.

Chapter - 3 Objectives, Methodology and Expected contributions

The aim of this research is to study physics of flow and heat transfer in the leakage gaps of positive displacement machines experimentally. By understanding the flow structure and flow-heat-solid interaction it may be possible to reduce internal leakages and improve reliability of PDMs.

3.1 Objectives

The research objectives of this study are:

- Identify experimental methods from the literature, which could be utilised to visualize flow velocities and temperatures in the clearance gaps of operating rotary positive displacement machines.
- Establish the test rig and obtain measurement results in the clearance gaps of operating Roots blower using three measurement methods. i) Particle Image Velocimetry (PIV) for measurement of the flow velocities, ii) Infrared thermography for measurement of the rotor lobe and casing temperatures and iii) Planar Laser Induced Fluorescence (PLIF) for measurement of the fluid temperature in the leakage gap.
- Evaluate the influence of the speed of rotation and operational pressures on physics of leakage flow and conjugate heat transfer in the operational Roots blower.

This research will lead to identifying methods for reducing leakage flows through clearance gaps and improving reliability of rotary positive displacement machines. This work will also generate the experimental dataset to validate numerical models developed for prediction of leakage flows in PDMs.

3.2 Methodology

Roots blower is a good representative of rotary positive displacement machines. The straight lobes of a Roots blower allow optical access suitable for analysis of flow physics in clearance flows of PDMs. The research approach is graphically shown in Figure 3.1. Firstly, with the help of literature review, suitable experimental methods will be identified for optical measurements of leakage flows and temperatures of the fluid and solid parts of the clearance gap. Secondly, optical Roots blower test rig will be design and developed. Parameters of the experimental setup for chosen measuring techniques will be developed.

Thirdly, an extensive experimental campaign will be carried out to collect data using selected Planar Laser Induced Fluorescence (PLIF), Particle Image Velocimetry (PIV) and Infrared Thermography (IR) measurement methods. Velocity field, temperature field and surface temperature of the lobe will be obtained by post processing of recorded data. After analysing the data together, findings will be derived to evaluate influence of the rotational speed and operational pressures on the leakage flows which will be a guideline for implementing methods for reducing leakage losses and improving reliability of oil free rotary positive displacement machines. The obtained experimental dataset will be used for development and validation of numerical methods for accurate prediction of such flows.

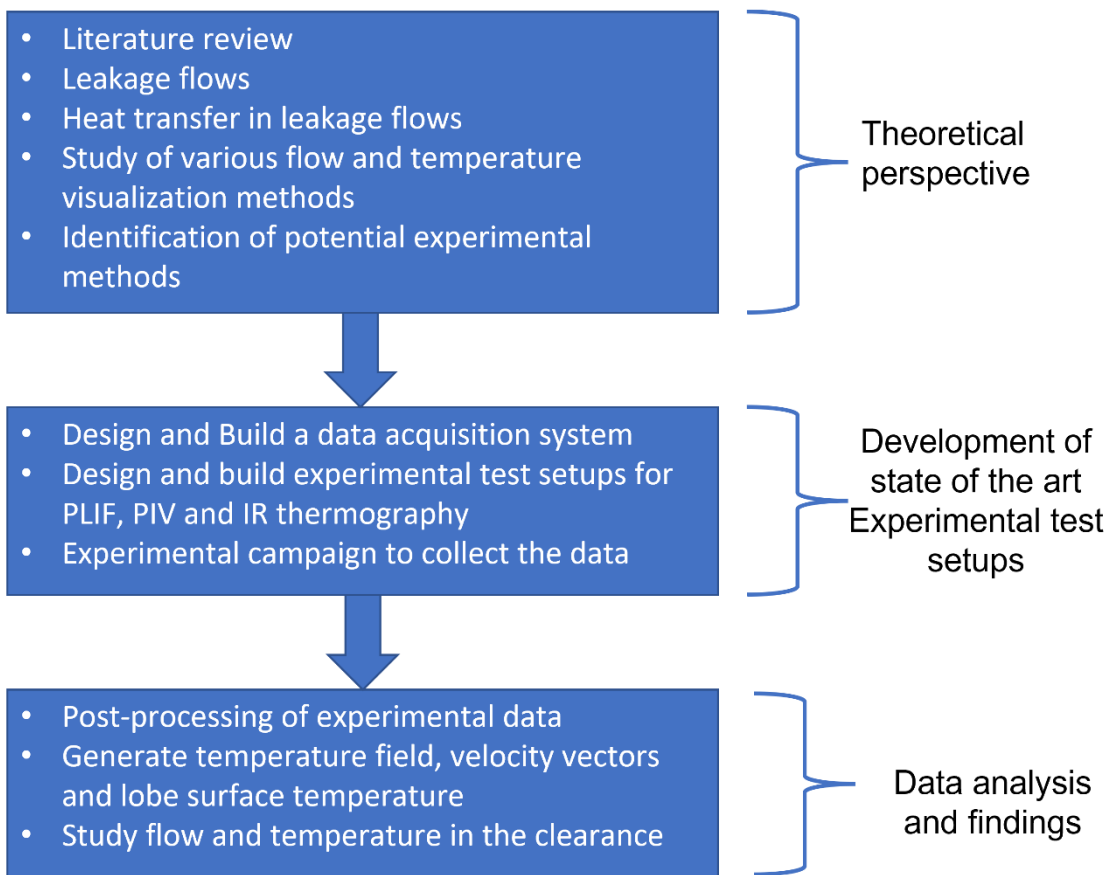


Figure 3.1 Research methodology

3.3 Expected contribution

This study is focused on the experimental investigation of flows and heat transfer in the leakages of rotary positive displacement machines. Following major contributions are expected to arise from the work,

- Report on the various available techniques for flow visualisation, which will result in the selection of suitable potential techniques to visualise the flow field and temperature field inside the clearance gaps in an operational rotary positive displacement machine.
- Design and installation of the experimental setups for the chosen experimental techniques including PLIF, PIV and IR thermography. Journals and conference publications will be produced in order to disseminate learnings to the wider community.
- Set of visual and statistical results of the fluid and temperature flow fields in the clearance gaps of rotating PDMs to investigate the fluid flow structure inside the leakage gaps and the effect of temperature on the flow. It will also generate research publications based on obtained results as well as a database of experimental results to help development and validation of numerical models for accurate prediction of physics in clearance gaps of PDMs.

This study will be the pioneering step to deliver an understanding of leakage flows in rotary PDMs using experiments during the operation of the machine.

Chapter - 4 PLIF Experimental Study

Temperature and velocity measurement in the clearance gaps of rotary PDMs during operation of the rotary PDM machine is challenging due to the size of these gaps. There are no dedicated techniques available for this kind of measurement. Therefore, various available techniques to measure temperature and velocity field are investigated in Chapter 2 and three different techniques have been selected for temperature and velocity measurements in the leakage gaps. These are, Planar laser induced fluorescence (PLIF), High speed infrared thermography and (IRT) and Particle image velocimetry (PIV) techniques for measurement of temperature field, surface temperature and velocity field respectively. PLIF technique is not used in the past to measure the temperature field inside the clearances of rotary PDMs during the operation of the machine. Therefore, feasibility study is carried out to see its potential to measure the flow field temperature and to derive improvement ideas to use it for this measurement. PLIF feasibility study is presented in this chapter.

4.1 PLIF experimental setup and procedures

PLIF experiment consist of two major parts, the optical roots blower test rig connected with data acquisition system and the optical arrangement for PLIF. This test campaign was carried out on the optical Roots blower test rig which was shipped to LaVision, in Germany where two distinct setups are prepared and tested.

4.1.1 Roots blower test rig

The schematic diagram of the Roots blower test rig is shown in Figure 4.1. In this study, a Howden URAI-22 oil-free Roots blower was used. The main characteristics of the used Roots blower are listed in Table 4.1. The machine is connected to a variable speed electric drive motor by a pulley transmission system to run at speeds of up to 2700 RPM. Motor speed is controlled by Variable Frequency Drive (VFD). To monitor and control the operating parameters of the machine, pressure and temperature sensors were installed at suction (P1, T1), discharge (P2, T2) and at the orifice plate (ΔP , T3) as shown in Figure 4.1. A shaft encoder and torque meter were used to measure the speed and power input to the Roots blower. The flow through the machine was derived from the measurements across the orifice plate. The detailed specifications of used sensors are listed in Table 4.2. The speed of the motor was governed by the variable frequency drive. A manually controlled ball valve, installed in the discharge line of the machine, was used to set the

required discharge pressure. The pressure was limited to 2 barg, to avoid excessive discharge temperatures. All sensors were connected to a National Instrument-based data acquisition system and real-time data was recorded using LabView based programming. In order to visualize the temperature field inside the Roots blower, it is necessary to allow an optical access in the machine. For PLIF, the optical element should be transparent for UV light and for this application it had to withstand temperatures and pressures of up to 300 °C and 7 barg respectively. For all these requirements, a fused silica glass is the most suitable material. As shown in Figure 4.2, the green highlighted portion of the casing was replaced by the fused silica glass window. Figure 4.3(a) shows a complex shape of this optical glass. The optical access in radial direction where the laser sheet is applied is shown in Figure 4.3(b) while the optical access to visualize the flow in the clearance gap between the rotor tip and housing is shown in Figure 4.3(c). A thin gasket was provided between the metal and glass surfaces to avoid direct contact and reduce risk of the glass cracking. The glass contact was kept tight using an external metal plate to eliminate leakage through the glass and metal mating surfaces.

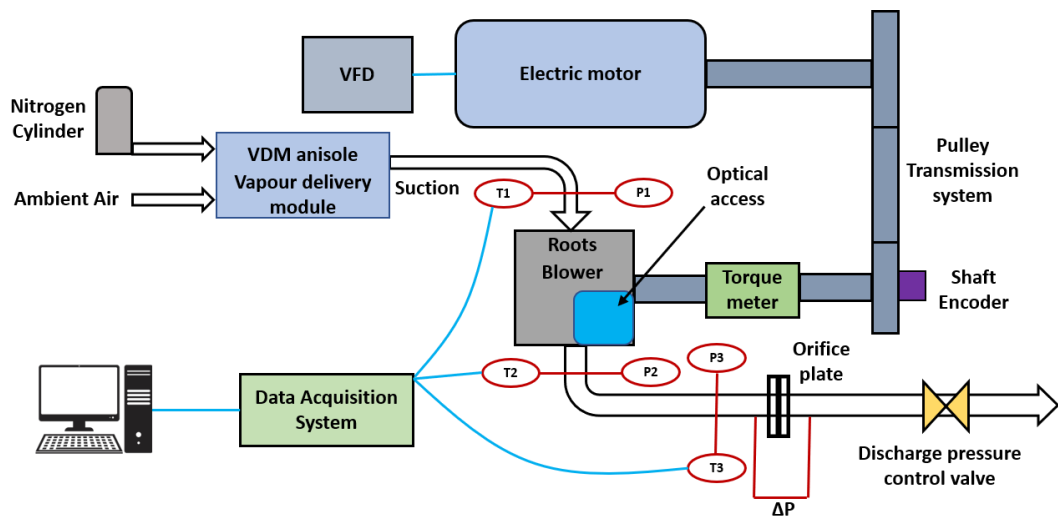


Figure 4.1 Schematic diagram of Roots blower test rig

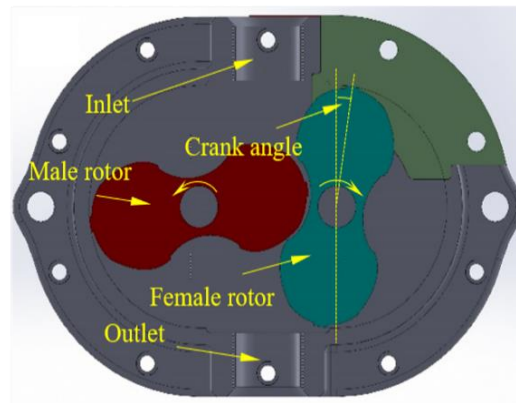


Figure 4.2 Rotors position in the Roots blower [23]

Table 4.1 The main parameters of the Roots blower

Items	Specification	Items	Specification
Diameter of the rotor [mm]	101.3	Tip gap[mm]	0.1
Axis distance [mm]	63.12	Interlobe gap[mm]	0.17
Rotor length [mm]	50.5	Axial gap[mm]	0.15
Displacement volume [l/rev]	0.4618	Width of tip step[mm]	6.4

Table 4.2 Sensor specifications

Parameters	Instrument	Specification
Speed, N	Shaft encoder (BHG 16.25W.3600-B2-5)	3600 TTL pulses per revolution Accuracy= $\pm 10\%$ of TTL pulses
Torque, T	TP-5 KMCB torque meter (Strain gauge transducer)	Max capacity: 50Nm, Range = 0 – 6000 rpm, Supply volt=10v dc, Accuracy= 0.25 % of max capacity
Inlet pressure, P1	PMP5026 pressure transducer	Operating range = 3.5bar(abs) Excite voltage=12-16V dc, Output voltage = 0-10 V Accuracy = $\pm 0.2\%$
Inlet temperature, T1		
Outlet temperature, T2	Platinum resistance thermometer	Range= -75°C to 250°C , accuracy= $\pm 0.5^{\circ}\text{C}$
Orifice plate inlet Temp, T3		

Outlet pressure, P2	PMP5026 pressure transducer	Operating range =15 bar (abs)
Orifice plate inlet pressure, P3	PMP5026 pressure transducer	Excite voltage=12-16V dc, Output voltage = 0-10 V accuracy = ±0.2%
Orifice plate differential pressure, ΔP	PMP5026 pressure transducer	Pressure diff = 0.5 bar excite voltage=12-16V dc, Output voltage = 0-10 V accuracy = ±0.2% FS.

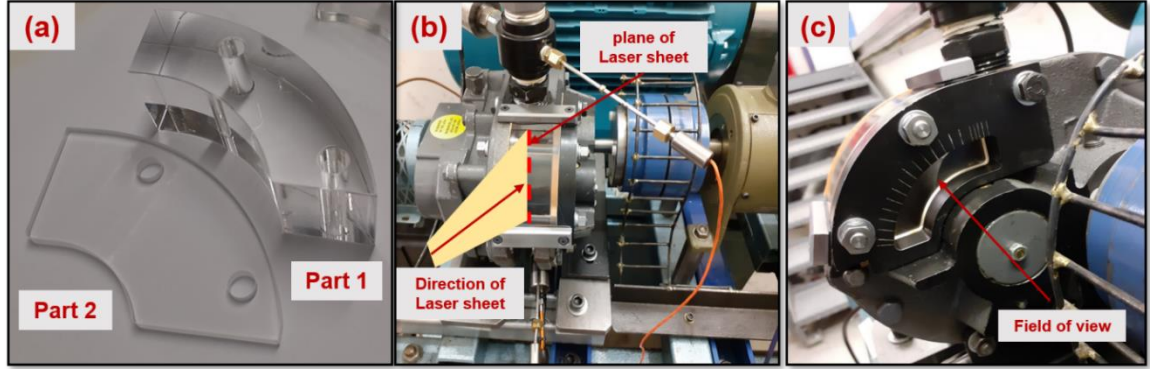


Figure 4.3 (a) Optical element made from fused silica glass (b) Radial optical access of Roots blower to apply laser sheet (c) Optical access from side of Roots blower to visualize radial clearance

4.1.2 PLIF Imaging

The LIF technique allows for spatiotemporally resolved, non-intrusive measurements of the scalar field, such as temperature and species concentration, by quantitatively interpreting the light emitted by a tracer molecule. Upon excitation by a light source produced from a laser, tracer molecules gain energy which is sometimes dissipated by photon emission. A camera collects these photons, and the resulting signal is quantified based on its relation to a relevant flow parameter. The quantification of this relation requires an in-depth understanding of the physics underlying the excitation process of the employed molecular tracer.

The total collected LIF signal (S_{LIF}) can be described by the following relationship [41],

$$S_{LIF} = \eta_{opt} \left(\frac{E_{pulse} \lambda}{A h c} \right) IV_{pix} \nu_{tracer} \sigma_{abs} \phi_f \quad 4.1$$

Where η_{opt} stands for the efficiency of the collection optics and incorporates factors such as the solid angle of the detector lens and the spectral responsivity of the detection system. E_{pulse} is local laser fluence, h is Plank's constant, c is the speed of light in vacuum, λ is the wavelength and A is the laser sheet area. Altogether the bracketed term represents the number of excitation photons per laser-sheet cross-sectional area. The size of the imaged volume (IV_{pix}) along the laser sheet propagation times the tracer number density (ν_{tracer})

gives the number of tracer molecules available for excitation. The last two terms, the absorption cross-section (σ_{abs}) and the fluorescence quantum yield (ϕ_f) account for the photophysical dependencies of the fluorescence signal and represent the probability of absorption and the efficiency of fluorescence emission respectively. The fluorescence properties of aromatic tracers such as toluene, naphthalene and anisole have been investigated, calibrated and employed in an engine-relevant planar air-to-fuel ratio measurement as well as in thermometry studies [41]. In this study anisole is used as a tracer. The anisole tracer has strong absorption in the UV and high signal sensitivity to temperature and oxygen concentration. Also, anisole yields the best signal per volume in both nitrogen and air. In terms of signal alone, anisole is a good choice for the compression of air considered in this study [42].

The two-colour detection approach (2-colour LIF) requires the illumination of the seeded volume and the subsequent detection of the emitted fluorescence by two detectors simultaneously (each looking at a different part of the emission spectrum). The resulting signal ratio (here abbreviated as $S_{\lambda_1}/S_{\lambda_2}$) depends only on the absorption cross-section and the fluorescence quantum yield of the tracer at the respective wavelength ranges [57]. Dependencies such as the pulse-to-pulse energy variation and tracer density cancel out, while others such as the efficiency of the detection optics are incorporated in a constant (C).

$$\frac{S_{\lambda_1}}{S_{\lambda_2}} = C \frac{\sigma_{abs}\phi_{f\lambda_1}}{\sigma_{abs}\phi_{f\lambda_2}} = f(T, v_{o_2}) \quad 4.2$$

It should be noted that the signal ratio depends essentially on two parameters, the local temperature and the local oxygen concentration. Therefore, a reliable calibration would require for both these quantities to be known. The arrangement of the PLIF imaging equipment with the Roots blower test rig includes two different data acquisition systems (DAQ); one being used to operate and record the Roots blower test rig data and the other for PLIF imaging. For PLIF imaging and post processing, DaVis software from LaVision is used, it provides ease to record, calibrate and post process the data. A more detailed explanation of the equipment and its arrangement is presented in subsequent sections.

4.1.3 Development of the 2-colour LIF using single camera

A schematic drawing of the imaging system is shown in Figure 4.4. The beam from the Q-smart Q-850 Nd:YAG laser at 1064 nm is guided through the 2C and 4C modules to convert it into 266nm. A laser sheet is then formed by the combination of the sheet optics and the cylindrical lens of -50mm. The sheet had a thickness of about 1mm and it was

placed at the central plane of the lobes of the Roots blower passing through the curved fused silica window. The average laser shot energy in the observation area was 100 mJ. The energy distributions along and across the sheet is Gaussian. As the total fluorescence signal through the sheet is collected by the camera, the non-uniform distribution through the laser-sheet has tendency affect this distribution. But this does not affect the results because in 2-colour LIF, same laser-sheet illuminates the images taken through both wavelength filters which are divided by each other. Owing to spatial constraints, the emitted fluorescence light was rotated by 90° using a UV mirror and guided to the detection optics. Two emitted wavelengths of 320nm and 280nm were selected based on the fluorescent spectra of anisole [42]. For that reason, two filters are needed to capture two different wavelengths from emitted light. One filter of 320nm with 40nm bandwidth and another filter of 280nm with 20nm bandwidth were used. To capture identical flow field by a single camera, it is necessary to change filters alternately at each measuring condition. The machine was operated for a sufficient time to achieve steady state for measurements at each operating condition as shown in Table 4.3. Images are recorded at each operating condition by changing the filters alternately. The LaVision Imager M-Lite CMOS camera (pixel size: $5.86 \times 5.86 \mu\text{m}^2$ and Number of Pixels: 1936×1216 pixels) with LaVision intensified relay optics and UV camera lenses (LaVision, $f = 100 \text{ mm}$, $f/2.8$) were used to record images of the field of view. Detection limit of fluorescence for the camera was estimated by LaVision using their database of Anisole LIF data. For instantaneous images with approximately 200 counts (image intensity), it was estimated that a standard deviation statistical uncertainty of $\pm 20 \text{ K}$ exists at the temperature of 300 K and slightly larger ($\pm 27 \text{ K}$) at 400 K. Phase-lock at a particular crank angle was achieved by an external triggering device with the custom signal modulation from LaVision. At each crank angle, 200 consecutive images were captured.

Following the two-colour strategy for measuring the temperature, the anisole fluorescence was seeded in the form of vapour using a Bronkhorst VDM (Vapour Delivery Module). This VDM needs nitrogen as a carrier gas to convert the liquid form of a seeding material into vapour. Nitrogen was supplied to VDM as a carrier gas and the flowrate of anisole and nitrogen mixture was adjusted using a mass flow controller. The mixture produced in the seeder was introduced at the suction hose of the Roots blower. The seeder maximum capacity of co-flow of air or nitrogen was 30 l/min. In this test, the nitrogen co-flow was kept at 30 l/min, and the anisole flow of 7 l/min was maintained with 5 l/min of carrier Nitrogen flow. The amount of seeded flow was determined by

checking the signal of the fluorescence particles in a recorded image at the beginning of the experiment. Measurements were carried out at the female rotor crank angle of 50° since this was the best position to obtain a clear image of the clearance area including upstream and downstream flow fields. The different test conditions at which measurements were recorded using a single camera are shown in Table 4.3. The discharge pressure and speed were increased by gradually closing the discharge valve and variable frequency drive (VFD) drive respectively. The terminology used for the rotor position in relation to the crank angle is shown in Figure 4.2. A sample LIF image taken by the single camera is shown in Figure 4.6. These images only represent recorded intensities using two different filters. To derive temperature fields from these images, post processing of data is required, and it is further explained in Section 4.1.5.

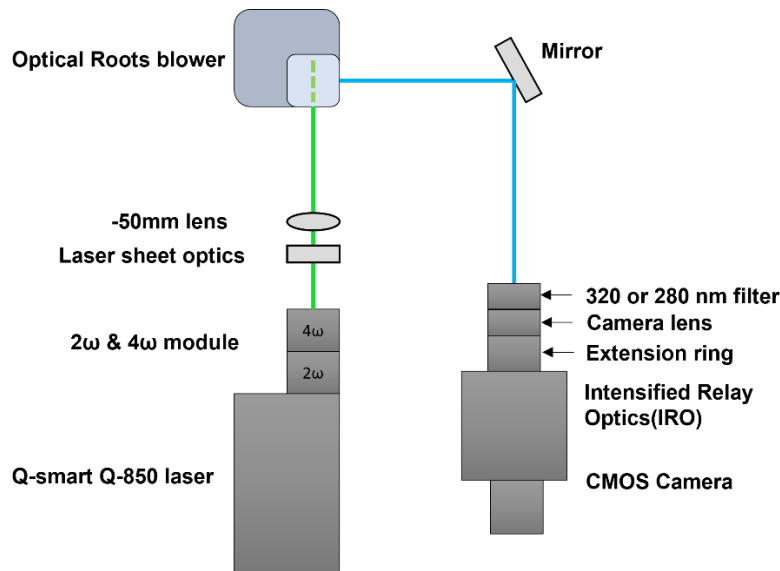


Figure 4.4 Arrangement of optics and Roots blower for single camera LIF imaging and measurement (a) Fused silica curved window

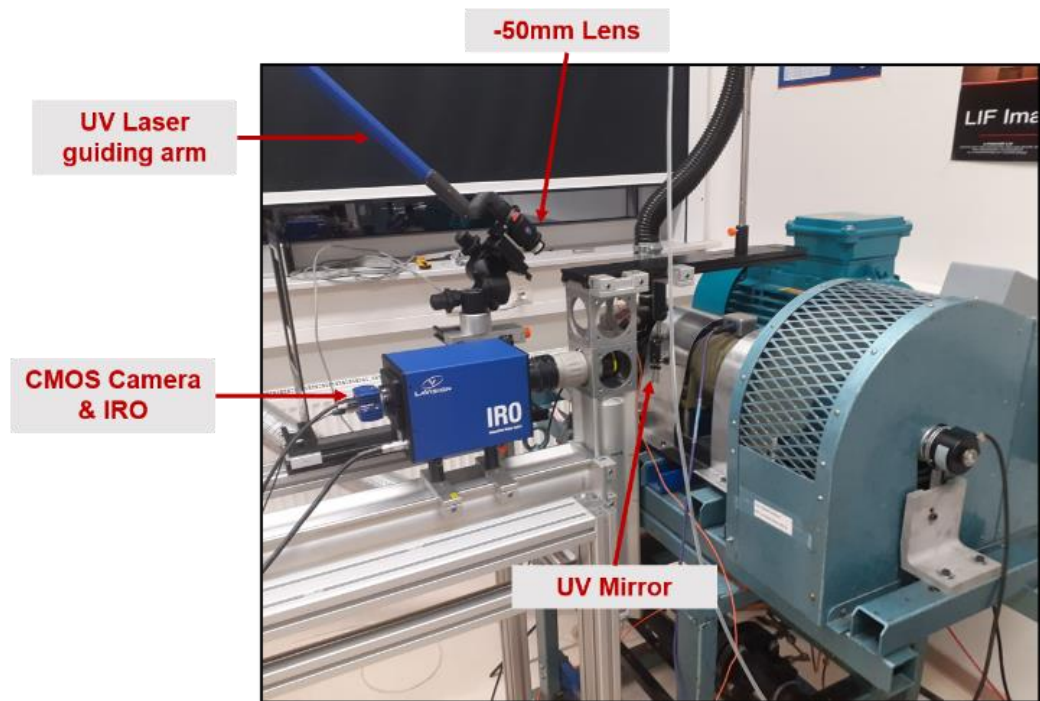


Figure 4.5 Single camera LIF setup

Table 4.3 Operating conditions during single camera LIF test

Speed (RPM)	Filter	Discharge pressure(barg)	Discharge temperature (°C)
300	320	1.04	22
	280	1.04	22
650	320	1.11	29
	280	1.11	27
900	320	1.18	37
	280	1.18	40
1200	320	1.29	59
	280	1.29	53
1500	320	1.43	80
	280	1.43	87

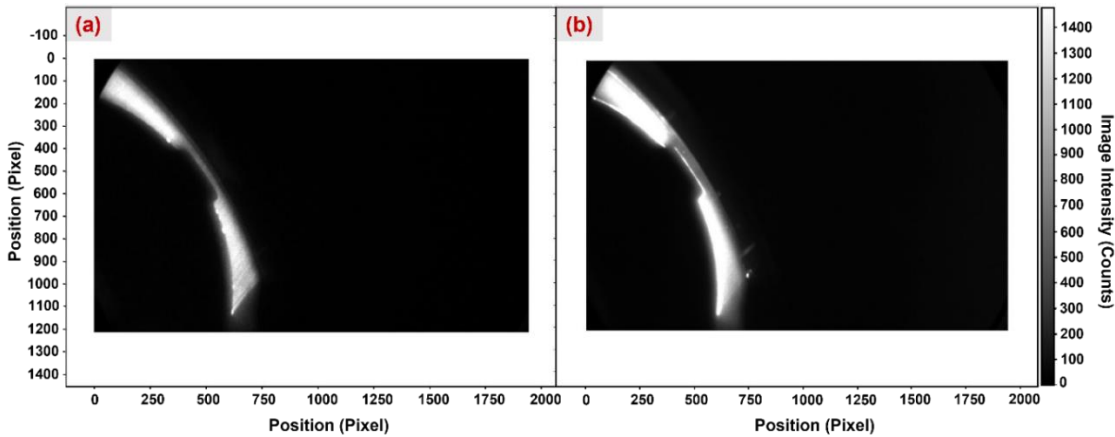


Figure 4.6 (a) Instantaneous image at 50° crank angle & captured using 320nm filter (b) Instantaneous image at 50° crank angle & captured using 280nm filter

4.1.4 Development of the 2-colour LIF using two cameras

The arrangement of the equipment for two colour LIF method is similar to that of the single colour LIF, but as shown in Figure 4.7, the second camera was installed with an intensifier relay optics (IRO) and extension ring (32mm). Two different filters were used, 320nm and 280nm, each attached to a separate camera. The angle between the axes of the two cameras was 90° and the fluorescence spectrum was split between the two cameras using a dichroic mirror.

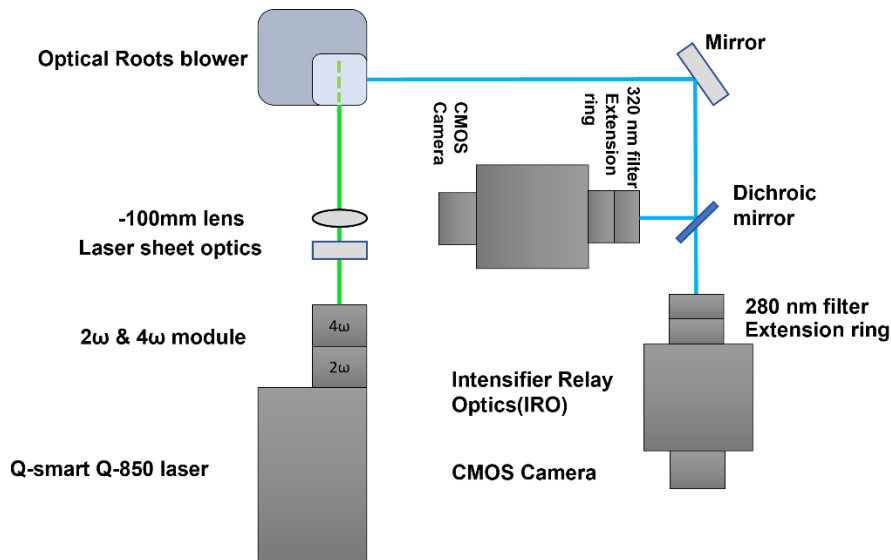


Figure 4.7 Arrangement of optics and Roots blower for double camera LIF imaging and measurement

Similarly, as for the single camera setup, a 50mm cylindrical lens was used to generate a laser sheet. The seeder allowed a supply of co-flow of air or nitrogen up to 30 l/min. The air co-flow was kept at 30 l/min, and the anisole flow of 7 l/min was maintained with 5 l/min of carrier nitrogen flow. The nitrogen flow was maintained to as low as possible

level in order to avoid oxygen quenching but allow the seeder to operate. At the beginning of the experiment, the amount of seeded flow was determined by checking the level of fluorescence particle's signal in the recorded image. The arrangement of the two-camera LIF which enables a target field to be captured with two different filters simultaneously is shown in Figure 4.8. Sample frames (frame 0 and frame 1) captured by the two different cameras, when the blower was rotating at 300 RPM, are shown in Figure 4.9.

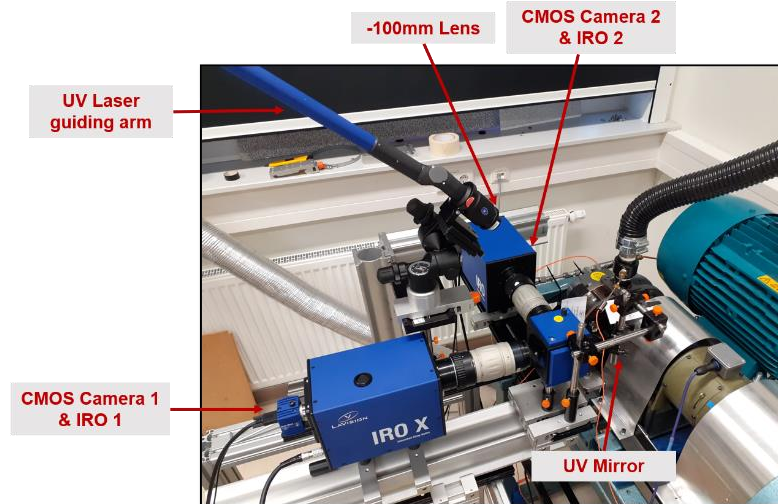


Figure 4.8 Two camera LIF setup

Different test conditions at which measurements were recorded using two cameras, are shown in Table 4.4.

Table 4.4 Operating conditions during two camera LIF test

Speed (RPM)	Discharge pressure(barg)	Discharge temperature (°C)
300	1.05	19
650	1.09	26
900	1.18	33
1200	1.34	44
1500	1.50	70
1800	1.65	100
2000	1.75	141

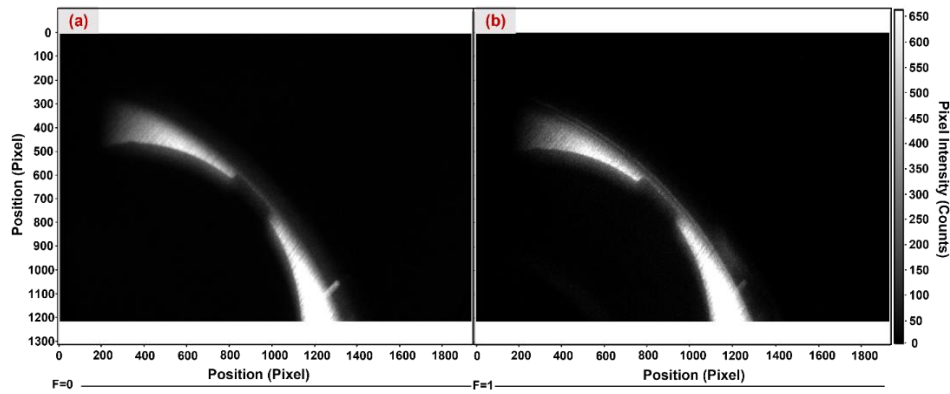


Figure 4.9 Two frames captured simultaneously at 300 RPM by two camera arrangement (a) Frame 0 captured by camera using 320nm filter (b) Frame 1 captured by camera using 280nm filters

4.1.5 Temperature calibration and image processing

The biggest challenge to the development of reliable temperature calibration in this research was that no predefined temperature data of the flow field inside the Roots blower was available. However, it was reasonable to assume that the temperature in the large volume of the targeted field, indicated with letter V in Figure 4.10, was equal to the discharge temperature from the blower. This value was easily obtained from the temperature sensor in the discharge line.

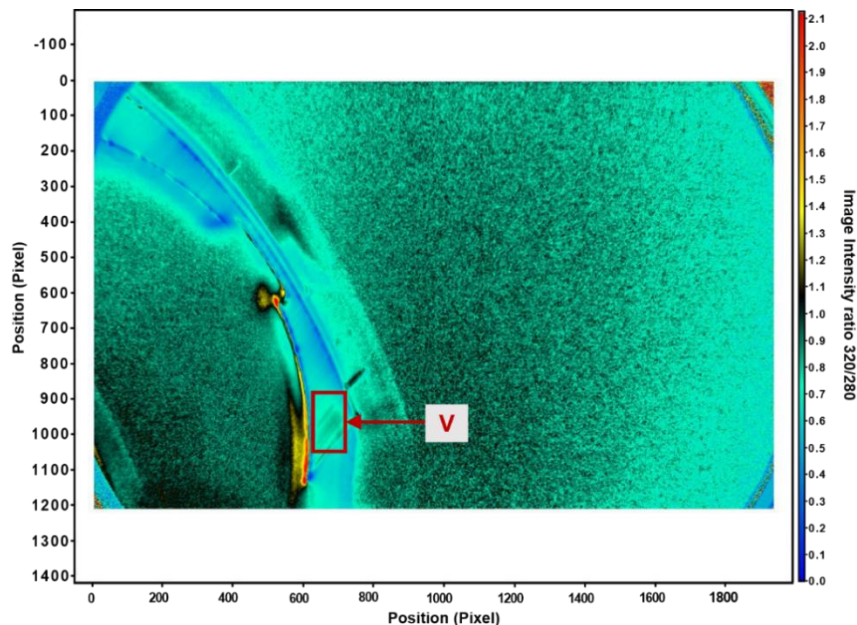


Figure 4.10 Considered large volume 'V' on discharge side of the machine for temperature calibration

To visualize the temperature, the recorded images had to be processed. The image processing method is shown in Figure 4.11. According to Equation 4.2, the ratio of the

two images can produce a temperature image. The image processing steps to process PLIF recordings are outlined below. This processing was realised using LaVision Davis software, which was also used to record the measurements.

- I. When taking a picture of the flow field, the projected image on the camera sensor from both filters will have distortion. This distortion is significant in two camera measurement. To correct for this one image should be transformed back to the coordinates of another image, this is called image mapping process. It is not necessary for images captured using single camera arrangement because captured image will be on same sensor, but it is applied on the images captured using two camera setup because position of camera sensors are different.
- II. One image is normalized by another image; in this case, the image captured with the 320nm filter was normalized by image captured with the 280nm filter.
- III. Image normalisation produced the image with raw ratio values. It is function of temperature.
- IV. For the measurements performed in this experiment, it is assumed that the temperature in the discharge side (region denoted by ‘V’ in Figure 4.10) is equal to the temperature measured by temperature sensor at the discharge of the Roots blower. Using this correlation, the raw intensities are converted into temperature.

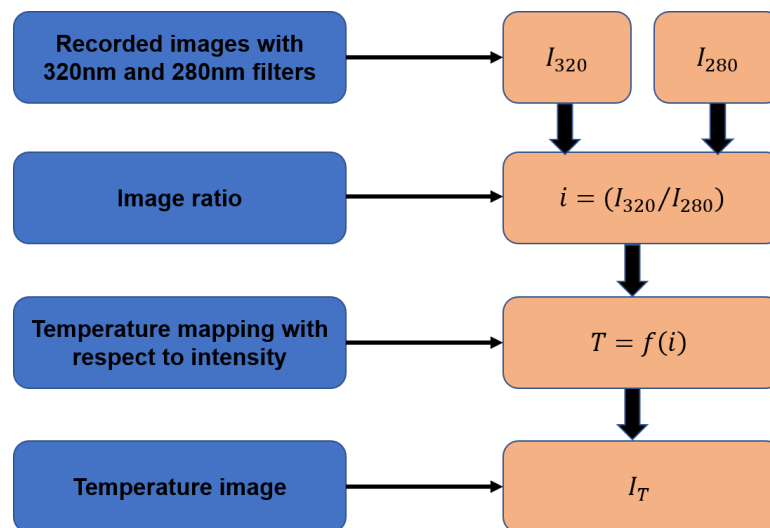


Figure 4.11 Schematic overview of the data processing for LIF imaging

4.2 PLIF measurement results: advantages and limitations of the technique

The single camera procedure was required to check the quality of the temperature images in order to fine tune the various aspects of the setup such as amount of tracer particles,

signal strength, phase-locking and its ability to analyse the temperature field in the compressor clearances. However, it has several limitations, namely:

It was observed that reasonable amount of time was needed to change the filters for each measuring condition from 320nm to 280nm filters or vice-versa, the blower operating condition and hence the internal temperatures may change during this period. This may result in an incorrect estimate of temperature because the ratio of 320/280 images cannot be obtained at the same instant.

The fluorescence signal is sensitive to both temperature and oxygen concentration. Fluorescence from the tracer can be lower in air than in nitrogen due to quenching by oxygen. The mixture of Nitrogen and anisole introduced with air at the suction may get affected by oxygen quenching.

Very high-intensity signals from the lobe surface were observed, main cause is the vaporisation of lobe paint which was observed due to the high energy of the applied laser. Laser was operated at full energy of 100mJ/pulse which is sufficient to burn the paint. So, near to the lobe wall surface, vaporization of paint was captured instead of fluorescence particles.

The test results for the temperature field from 300 RPM to 1500 RPM obtained by the procedure described in section 4.1.5 for single camera arrangement and they are shown in Figure 4.12 and Figure 4.13. The flow domain above section AA is the low-pressure region of the suction side while the flow domain below section AA is the high-pressure region of the discharge side. As it can be observed, with the increase in speed and discharge pressure, the bright area on the suction side increases in size and intensity. This is most likely due to reflections from the rotating lobe surface and glass. As the speed increases, the repetition rate of the laser striking the lobe also increases. This results in the glow along the lobe and glass to extend towards the middle of the flow domain with the increase in speed. One of the options to eliminate this glow is to fine tune the position of the laser sheet. For the reason mentioned above, it is expected that the temperature measurement may not be accurate in this area. Temperature variation along the section AA indicates that temperature at the centre of the clearance decreases in each case. As shown in Figure 4.14, the overall temperature inside the clearance is increasing with increase in speed and pressure ratio. It is noticeable that the temperature is minimum at the centre of the clearance.

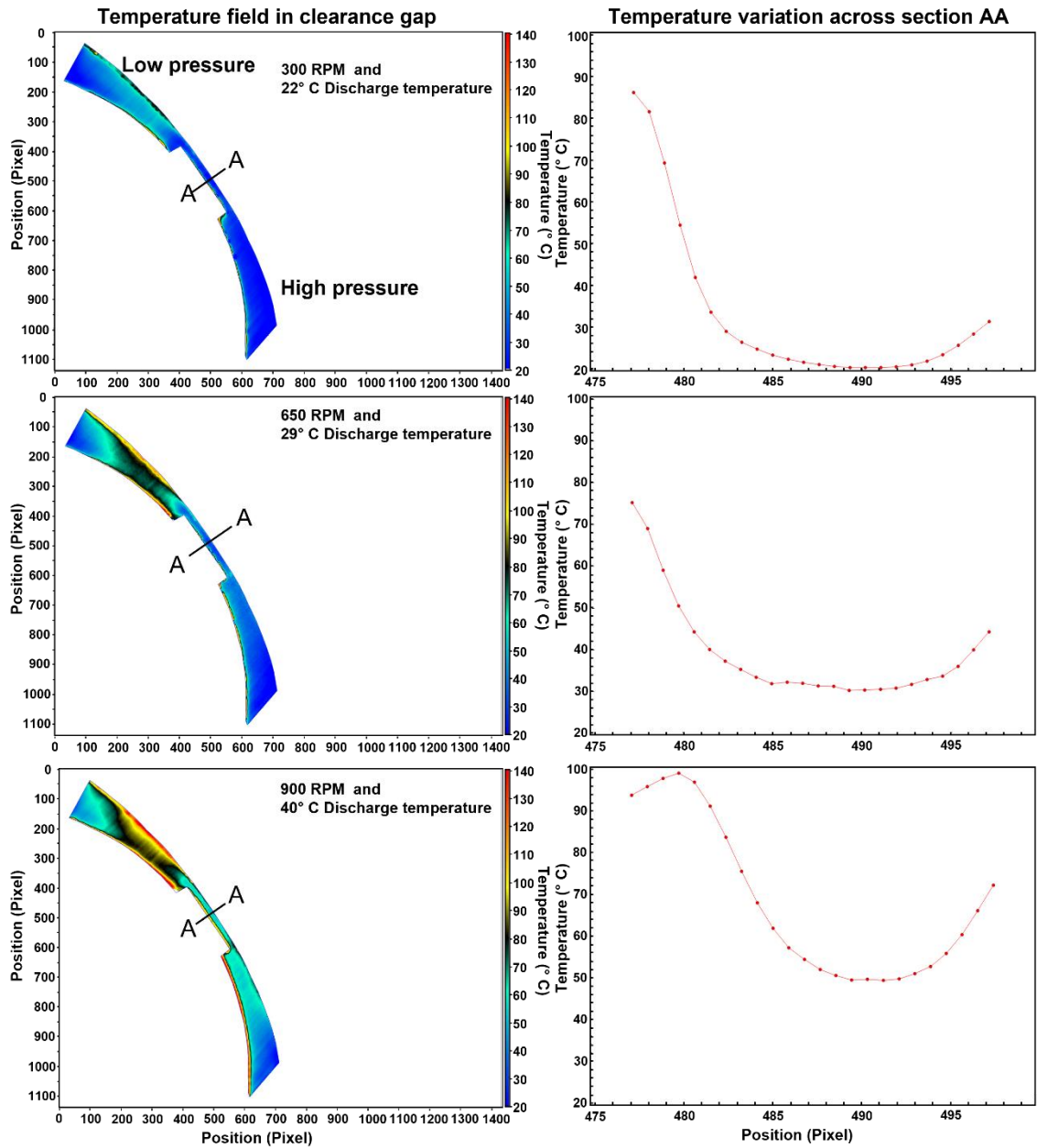


Figure 4.12 Temperature field in the clearance gap with temperature variation across the clearance from single camera LIF measurement (300 to 900 RPM)

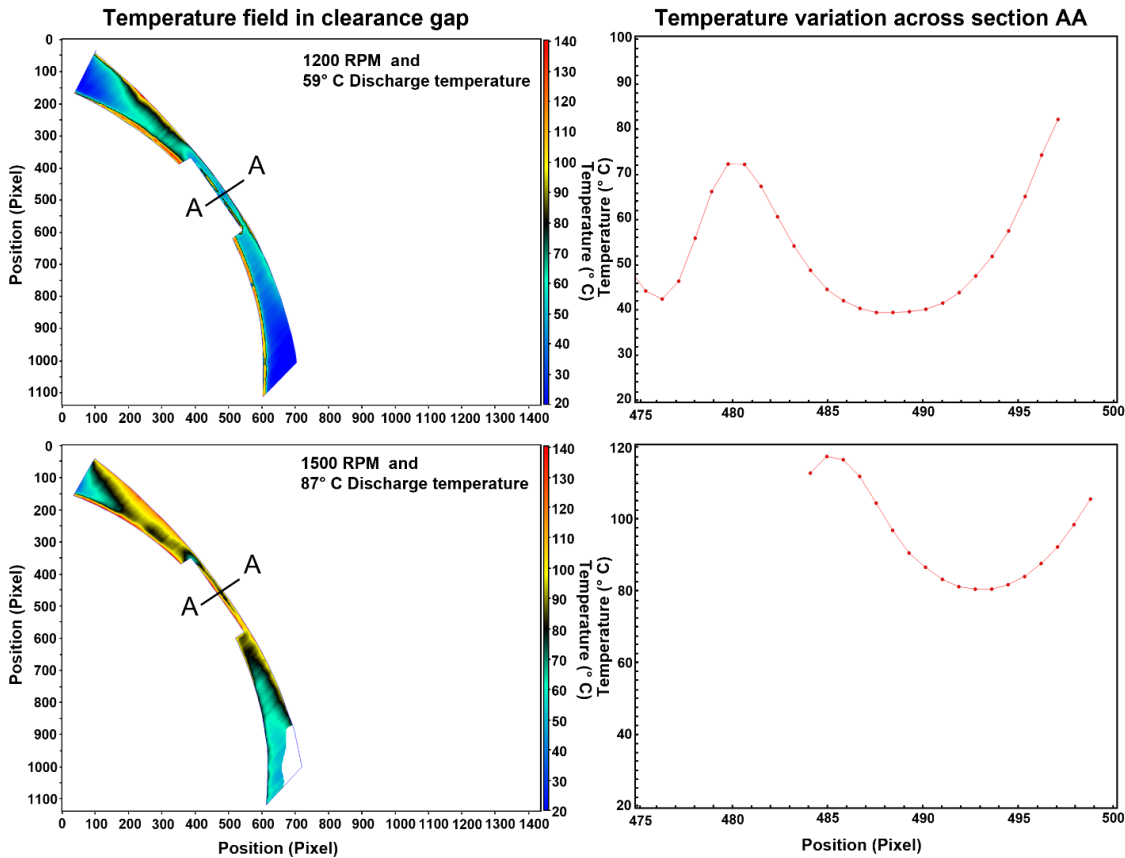


Figure 4.13 Temperature field in the clearance gap with temperature variation across the clearance from single camera LIF measurement (1200 & 1500 RPM)

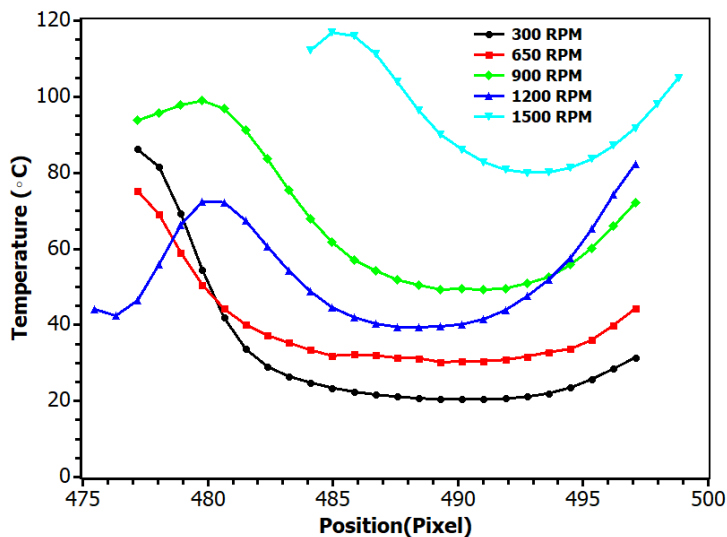


Figure 4.14 Comparison of temperature variation across the clearance gap at different RPM from single camera LIF measurement

The two-camera set-up was developed to eliminate problems encountered with the single LIF camera imaging. To reduce the possibility of oxygen quenching, the anisole seeding line was supplied with Nitrogen while the excess air was sucked in from the

atmosphere. However, this can reduce the LIF intensity, lower signal to noise ratio can cause the need of higher IRO (Intensified Relay Optics) gain values. Oxygen quenching is a process which decreases the fluorescence intensity of an anisole. Operating the machine with pure nitrogen could have significantly boosted the fluorescence intensity, while reducing signal to noise ratio. In addition, installing a larger focal length lens on the sheet optics could boost the collected fluorescence signal by a factor of 2 for the $f = -100\text{mm}$ lens as it would generate less divergence along the length of the glass.

Simultaneous use of two cameras eliminated the time interval needed to capture two images during single camera measurement but introduced a problem with the image mapping since the two cameras had to be located at different locations. In other words, if one of the two cameras move then the mapping function will change and the ratio of the two images will be inconsistent at different stages of the measurement campaign. This will result in the mapping function error which is prevented using very robust mounts for cameras, intensifiers, lenses, filters and dichroic mirror. To compensate for the different locations of cameras and to generate a reliable image ratio, firstly the image mapping was tried to carry out using DaVis software, but it was not able to generate acceptable image mapping so, MATLAB code was developed inhouse to transform the 320nm image with respect to 280nm image. MATLAB programming transform the co-ordinates of one image in such a way that it matches with other image. MATLAB code is provided in Appendix B. To transfer the co-ordinates, manually calculated clearance gap and rotor tip position is required as an input. The resulting temperature field thus obtained is shown in Figure 4.15 and Figure 4.16. More glares are observed in these results, and this made it difficult to visualize the temperature. As shown in Figure 4.17, the temperature along section AA shows randomness and has no consistent pattern. These images do not produce reliable values of temperature in the clearance gap. However, in future this issue can be resolved by implementing more reliable image mapping or by using DualScope to measure two images simultaneously with a single camera. DualScope is an optical splitting system that allows simultaneous acquisition of two spatially identical but spectrally separated images simultaneously with the use of only one single camera. Presented temperature plots are used to evaluate applicability of the PLIF technique, and the detailed error analysis along with confidence interval of quantitative results is not carried out.

Another most significant challenge associated with the two-camera experiment is the generation of reliable temperature calibration for the LIF signal ratio. One approach could

be to supply the Roots blower with already preheated anisole-seeded flow over a range of temperatures, operate the Roots blower in a free-flowing condition and calibrate at the desired crank angle of lobes. Alternatively, the calibration could be performed outside the Roots blower using a flow-cell; however, as the excitation arrangement and background fluorescence intensity would differ, this procedure should be carried out very carefully.

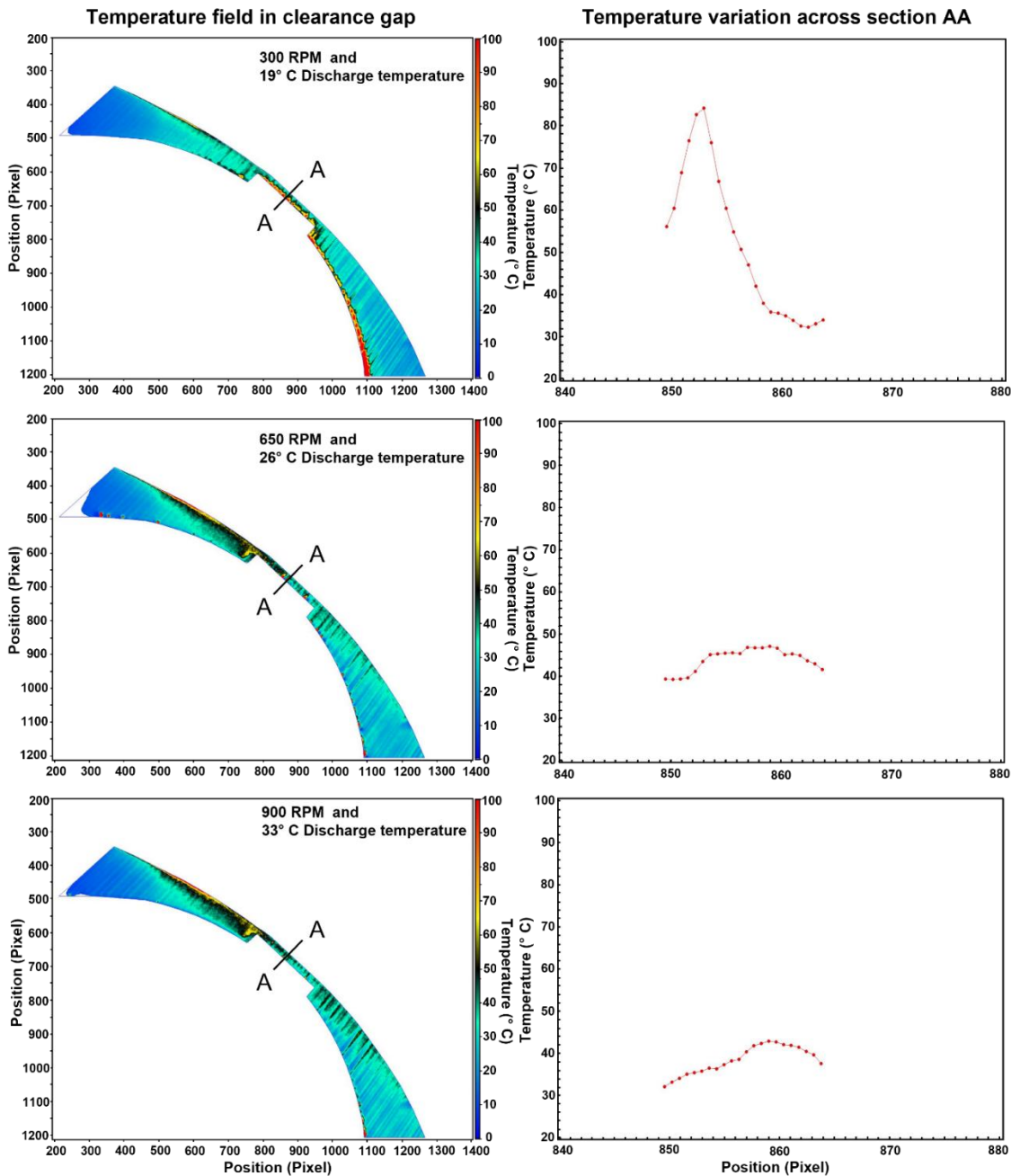


Figure 4.15 Temperature field in clearance gap with temperature variation across tip clearance from two camera LIF measurement (300 RPM to 900 RPM)

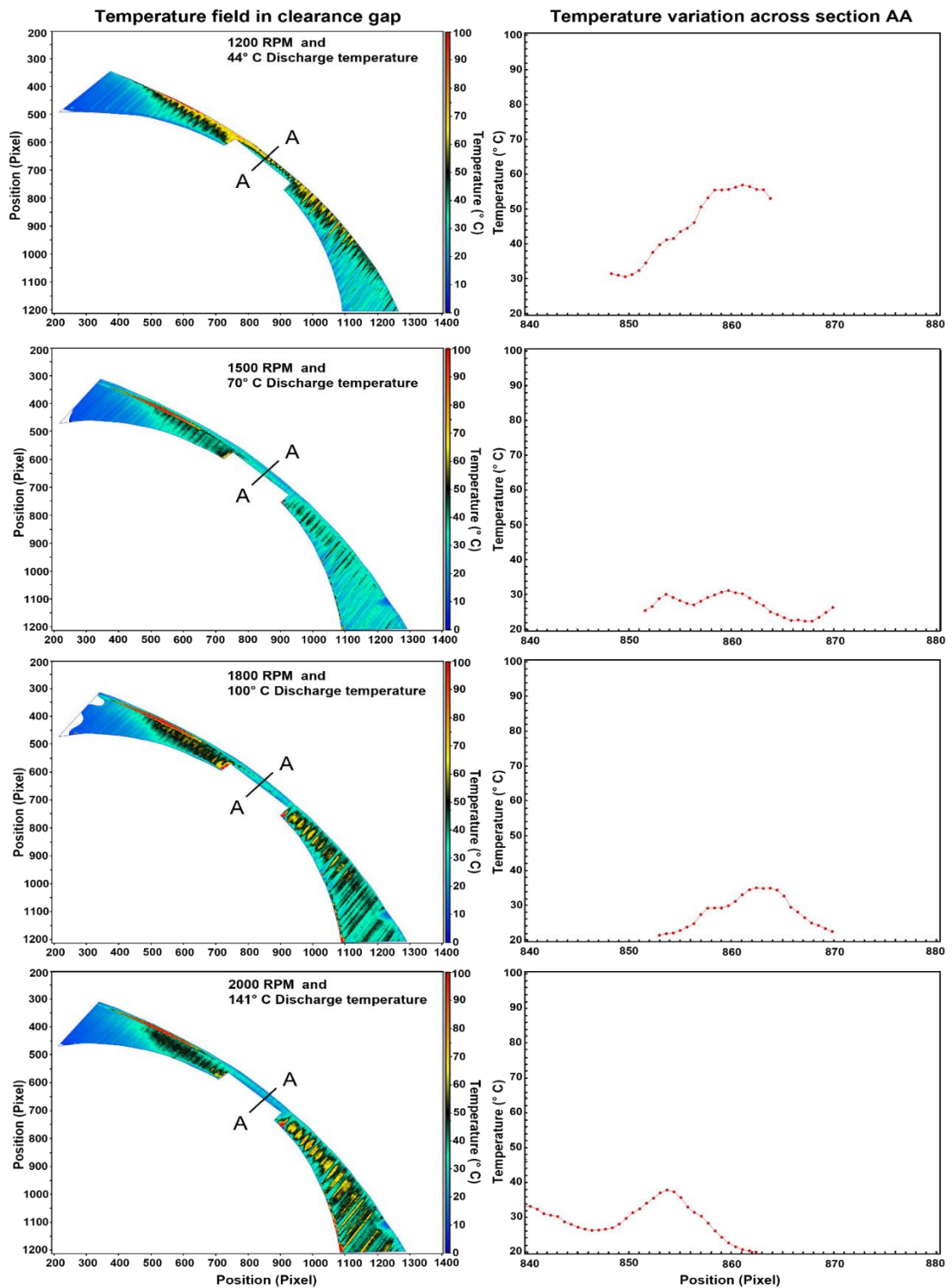


Figure 4.16 Temperature field in clearance gap with temperature variation across tip clearance from two camera LIF measurement (1200 RPM to 2000 RPM)

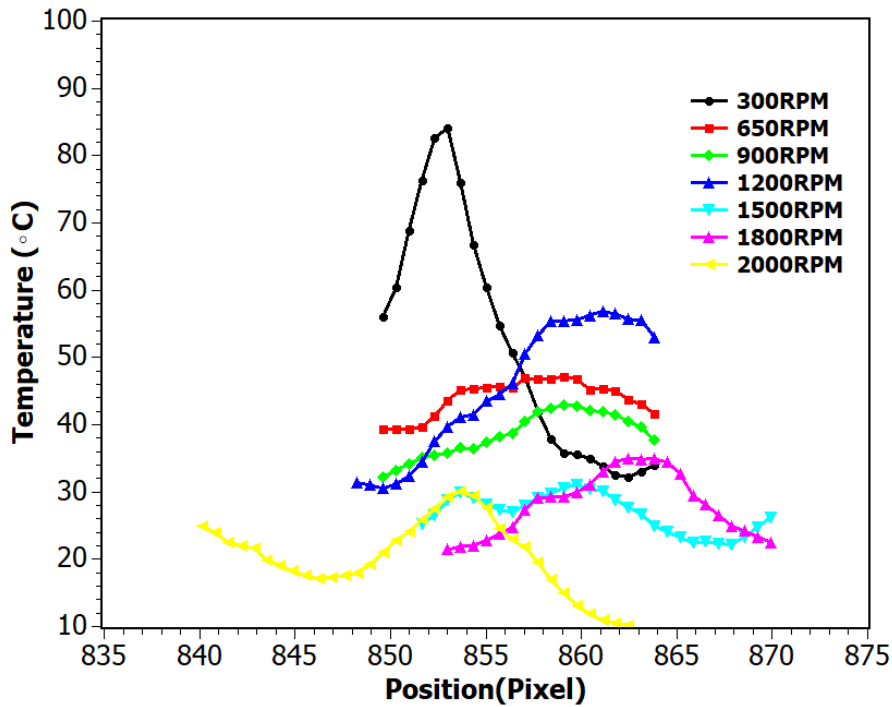


Figure 4.17 Comparison of temperature variation across the clearance gap at different RPM from two camera LIF measurement

Feasibility study of PLIF measurement technique is carried out using two different arrangements namely single camera setup and two camera setups. Results obtained from single camera arrangements are promising while results from two camera setups are not reliable. However, this feasibility study has provided valuable improvement ideas to further develop PLIF experimental setup to study flows inside the clearance of rotary PDMs.

4.3 Uncertainty in PLIF measurements

Feasibility study of the PLIF technique was carried out in this study so the formal uncertainty analysis of PLIF measurements was not conducted. In doing so, it is important to acknowledge that there are potential sources of uncertainty in the results that may impact their accuracy and reliability

There are several sources of uncertainty that can impact temperature measurements obtained using Planar Laser-Induced Fluorescence (PLIF) techniques. Some of these sources include:

- Uncertainty in the fluorescence signal intensity: The fluorescence signal generated by the PLIF technique is proportional to the temperature of the medium being measured. However, the signal intensity can be affected by a variety of

factors, including variations in laser power and attenuation of the signal as it passes through the medium.

- Calibration uncertainty: Accurate temperature measurements using PLIF require calibration of the fluorescence signal intensity with known temperature values. However, there can be uncertainty associated with the calibration process, particularly if the calibration measurements are affected by noise or other sources of error.
- Uncertainty in fluorescence intensity ratio: In current cases, temperature measurements are obtained by comparing the fluorescence signal intensity from two different wavelengths. However, there can be uncertainty associated with the ratio of fluorescence intensities, particularly if both the wavelengths have different sensitivities to factors such as laser power or chemical interference.
- Variations in experimental conditions: Variations in experimental conditions such as laser power, ambient temperature, and pressure can also impact the accuracy of temperature measurements obtained using PLIF techniques.

Furthermore, it is important to note that a feasibility study is typically focused on demonstrating the potential of a measurement technique, rather than providing precise and accurate quantitative measurements. As such, the results of this study should be interpreted with caution and may not be suitable for applications that require highly precise or accurate data.

Despite these limitations, the feasibility study provides valuable insight into the potential of PLIF as a measurement technique. Future work could focus on conducting a more rigorous uncertainty analysis to obtain more accurate and reliable measurements, or on exploring ways to improve the calibration and control of experimental conditions to reduce the potential for uncertainty.

Summary

This chapter presents the feasibility study of PLIF measurement in Roots blower. The chapter provides details on the development of 2-color LIF using a single camera and two cameras, along with temperature calibration and image processing. The PLIF measurement results are presented, including the advantages and limitations of the technique. Additionally, the chapter provides the potential sources of uncertainty in temperature measurement using PLIF. Next chapter explains IR thermography experiments.

Chapter - 5 IR Thermography Experimental Study

This chapter describes the experiments carried out using high speed thermography camera to measure surface temperature of the lobe during the running condition of the machine along with the result analysis and uncertainty associated with the measurement.

5.1 IR thermography experimental setup and procedures

IR thermography consist of the Roots blower test rig connected with DAQ system and Infrared camera arrangement. This setup was produced inhouse at City using the infrared camera from Infratec, UK.

5.1.1 IR thermography experimental setup

IR thermography has been widely used for surface temperature measurement and it provides an effective approach for non-intrusive and spatio-temporal measurement of temperature. This technique is applicable for surface temperature measurement. In order to determine temperatures accurately with IR Thermography, careful attention toward a proper choice of windows, elimination of specular reflections from channel walls, and estimation of local emissivity changes are required. The principle of infrared thermography is based on the physical phenomenon that any body of a temperature above absolute zero ($-273.15\text{ }^{\circ}\text{C}$) emits electromagnetic radiation. There is clear correlation between the surface of a body and the intensity and spectral composition of its emitted radiation. [50] By determining its radiation intensity, the temperature of an object can thereby be determined in a non-contact way.

As shown in Figure 5.1, Infrared thermography setup is relatively simpler than the PIV and PLIF setup. The same Roots blower test rig used for PLIF was also used for this test. ImageIR 8300hp camera has been chosen, with the spectral range of 2 to $5.7\text{ }\mu\text{m}$, and temperature range of -40 to $1500\text{ }^{\circ}\text{C}$ with full frame rate of 355Hz. Sapphire glass is used to get an optical access to the lobe surface, glass thickness is 29.25mm and it has 83% transmissivity. These parameters are considered during post processing of measured data.

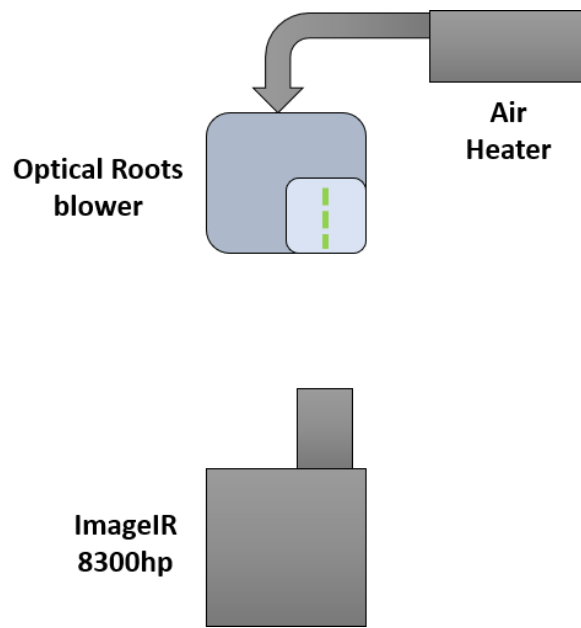


Figure 5.1 High speed Infrared thermography setup

IR thermography is carried out to measure the surface temperature of the lobe and the casing in the running conditions of the machine.

5.1.2 IR thermography experimental procedure

The machine is operated at various speeds and pressure ratios as listed in Table 5.1. The discharge pressure is maintained by closing the discharge valve of the machine. The actual setup is shown in Figure 5.2, ImageIR8300 camera is placed near the optical roots blower and focused on the lobe surface. Camera is phase locked with the rotor position using a shaft encoder and DAQ system to capture thermal images at a particular rotational angle of the lobe. IRBIS software from Infratec is used to record and analyse the data, and interface between DAQ system and IRBIS is developed to achieve the phase lock of Rotor position to capture images at desired rotor angle. Both lobes are painted black to get a maximum possible emission suitable for infrared thermography. The black paint is removed from part of one of the tips in order to help to focus camera exactly on the tip surface (Figure 5.3) as a reflection from the shiny portion will be clearly visible with the camera.

Table 5.1 Test conditions for IR thermography

Speed (RPM)	Pressure Ratio
1000	1.2
1240	1.2

1500	1.2
1800	1.2
2000	1.2
2000	1.4
1800	1.4
1500	1.4
2000	1.6
1800	1.6

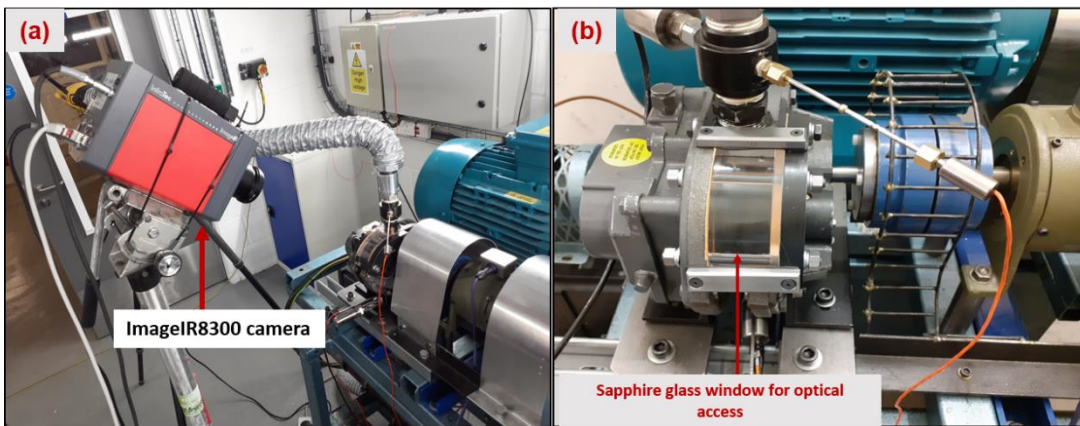


Figure 5.2 High speed infrared thermography test setup to measure lobe surface temperature

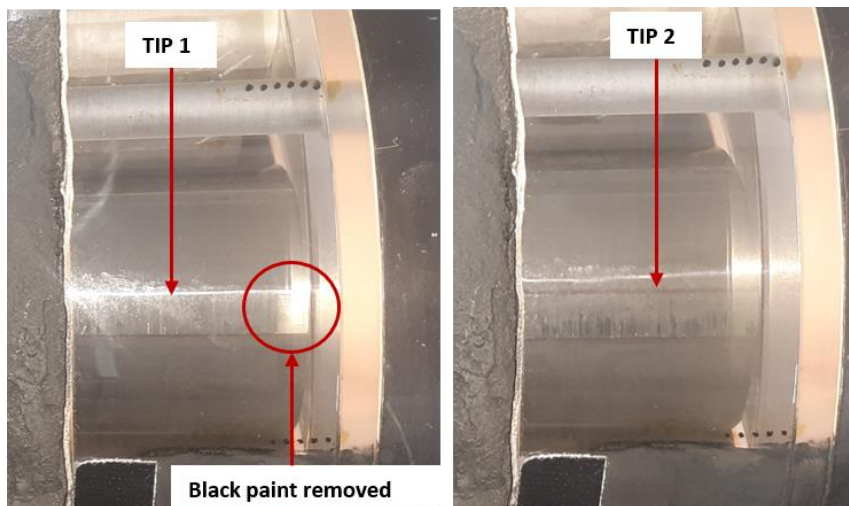


Figure 5.3 Images of Tip1 and Tip2 of the lobe

Temperature measurement of the outer casing is also carried out to study the temperature distribution on the surface of the machine. The arrangement of camera for this

measurement is shown in Figure 5.4(a). The blower surface is painted black on the outside to reduce reflections from the lobe surface, this paint doesn't change the temperature behaviour of the surface. The black painted blower with the example of thermogram is shown in Figure 5.4 (a) & (b). Measurements are carried out at the same operating conditions as listed in Table 5.1. The machine was allowed to stabilize at each operating conditions and after which the measurement is performed.

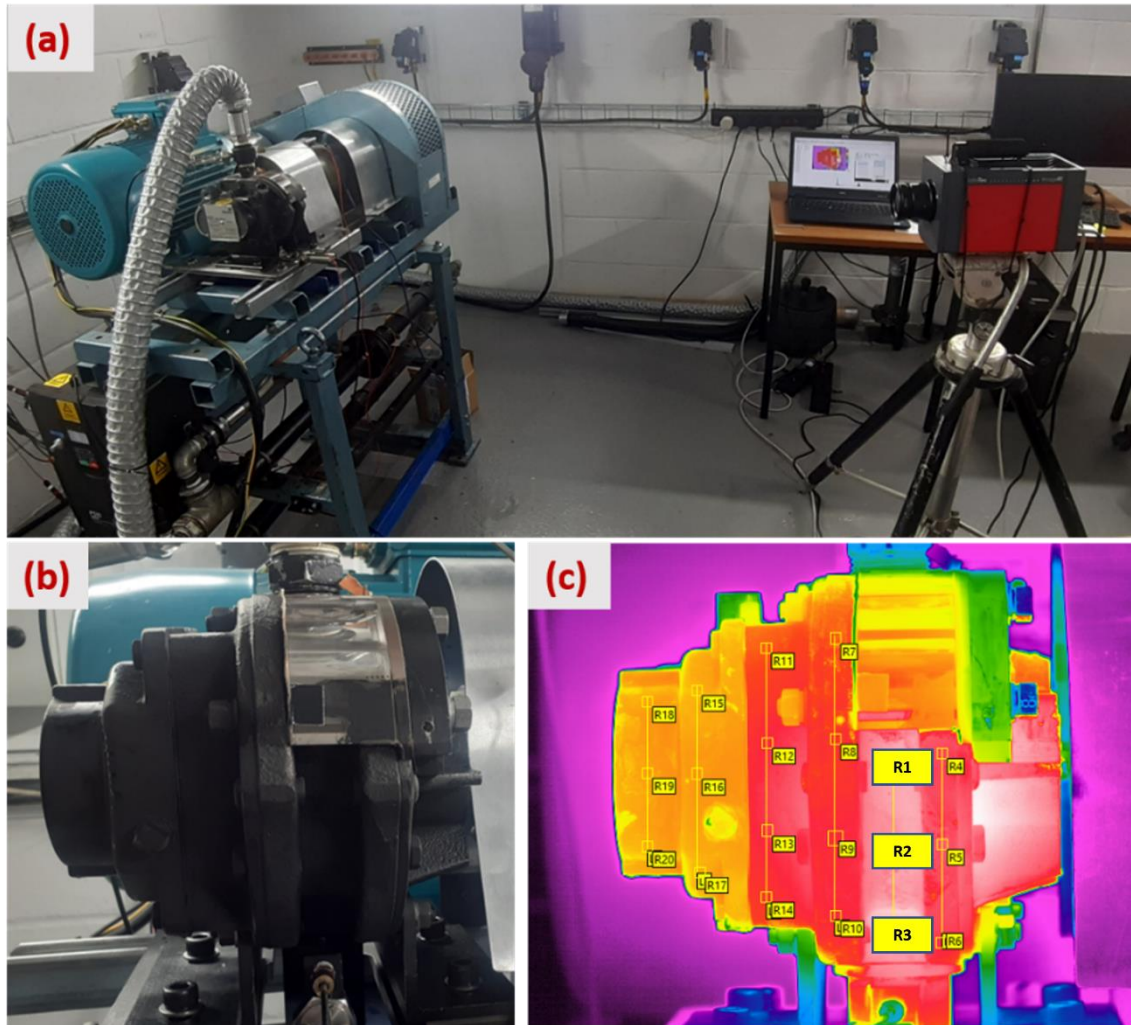


Figure 5.4 (a) High speed IR camera setup for casing temperature measurement (b) Black painted focused side of Roots blower (C) Example of thermogram of Roots blower

5.2 Infrared thermography measurement results

Thermal images, called “Thermograms” obtained from the Infrared thermography of the lobe surfaces are shown in Figure 5.5 and Figure 5.6 at all operating conditions. The lower side of the lobe is exposed to the high-pressure chamber and the upper side is exposed to the low-pressure chamber. To make the statistical comparison of temperature lines are plotted from suction side to discharge sides on this thermograms over which temperature

values are extracted. Also points P1 to P8 are placed on the thermograms, P1 & P5 lies on the surface of the lobe at discharge side while P2 & P6 lies at the edge of the tip at discharge side. Similarly, P4 & P8 lies on the surface of the lobe at suction side while P3 & P7 lies at the edge of the tip at suction side. At all operating conditions, temperature of the lobe surface in the high-pressure side below the tip is higher than temperatures of the low-pressure side above the tip. The surface temperature on the discharge side of the lobe is decreasing at same pressure ratio with increase in speed but it increases with the increase in pressure ratio. Figure 5.7 shows the clear trend where temperature on discharge side is decreasing with increase in speed at same pressure ratios. While it is interesting to see the temperature difference across the tip from Figure 5.8, value of temperature difference remains almost constant at constant pressure ratio across the tip but this difference is noticeable as plotted in Figure 5.9. It is clear that temperature is increasing as we move from suction side to discharge side over the tip surface. It shows that the thermal load on the lobe surface is varying with speed at the same pressure ratio. The probable reason is the decrease in leakage flow rate with the increase in speed. It is confirmed by PIV measurements, as explained in section 6.2.

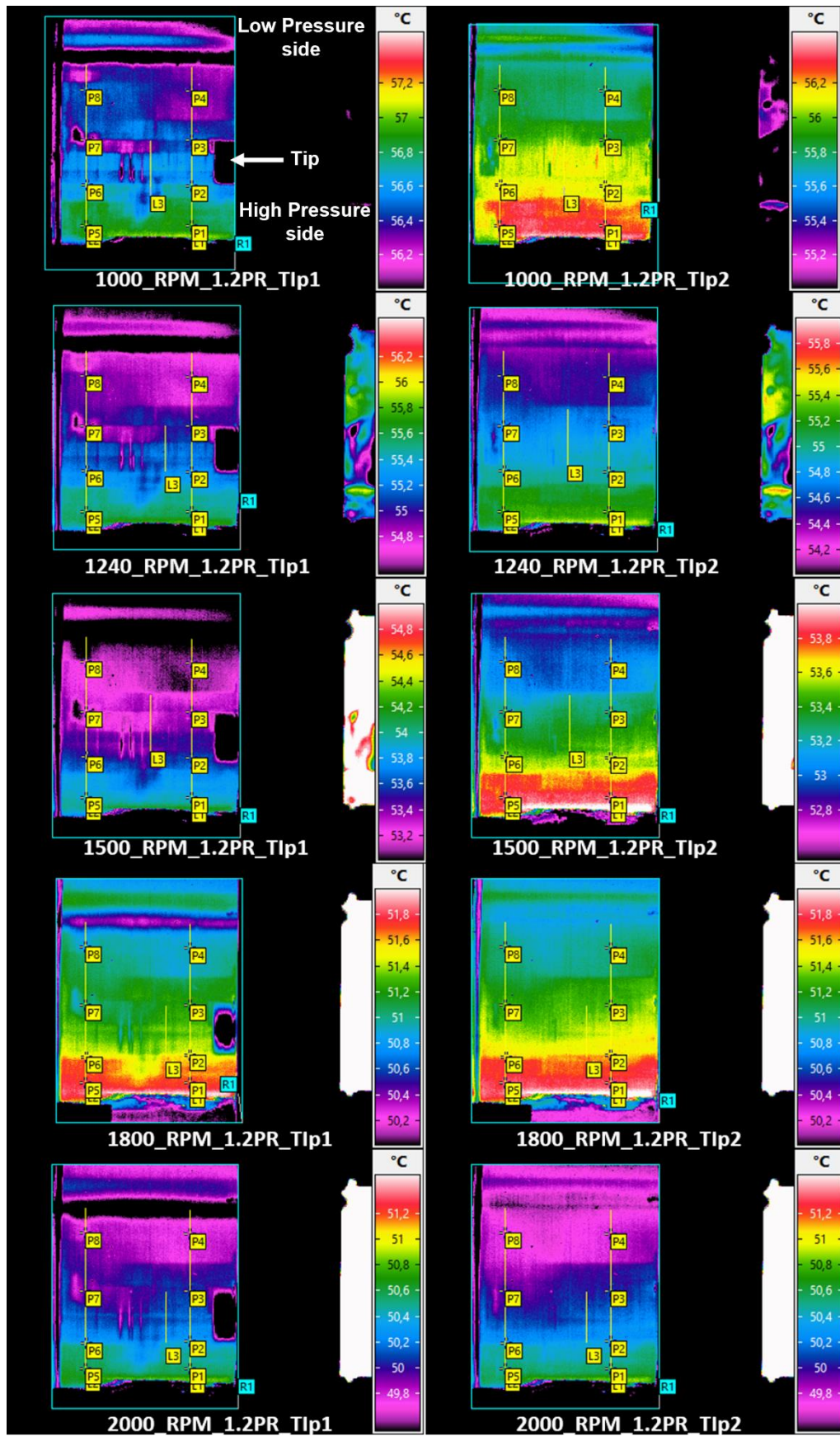


Figure 5.5 Thermograms of Tip1 and Tip2 at 1.2 PR various speeds obtained by averaging 500 instantaneous images represent surface temperature variation from high pressure side to low pressure side.

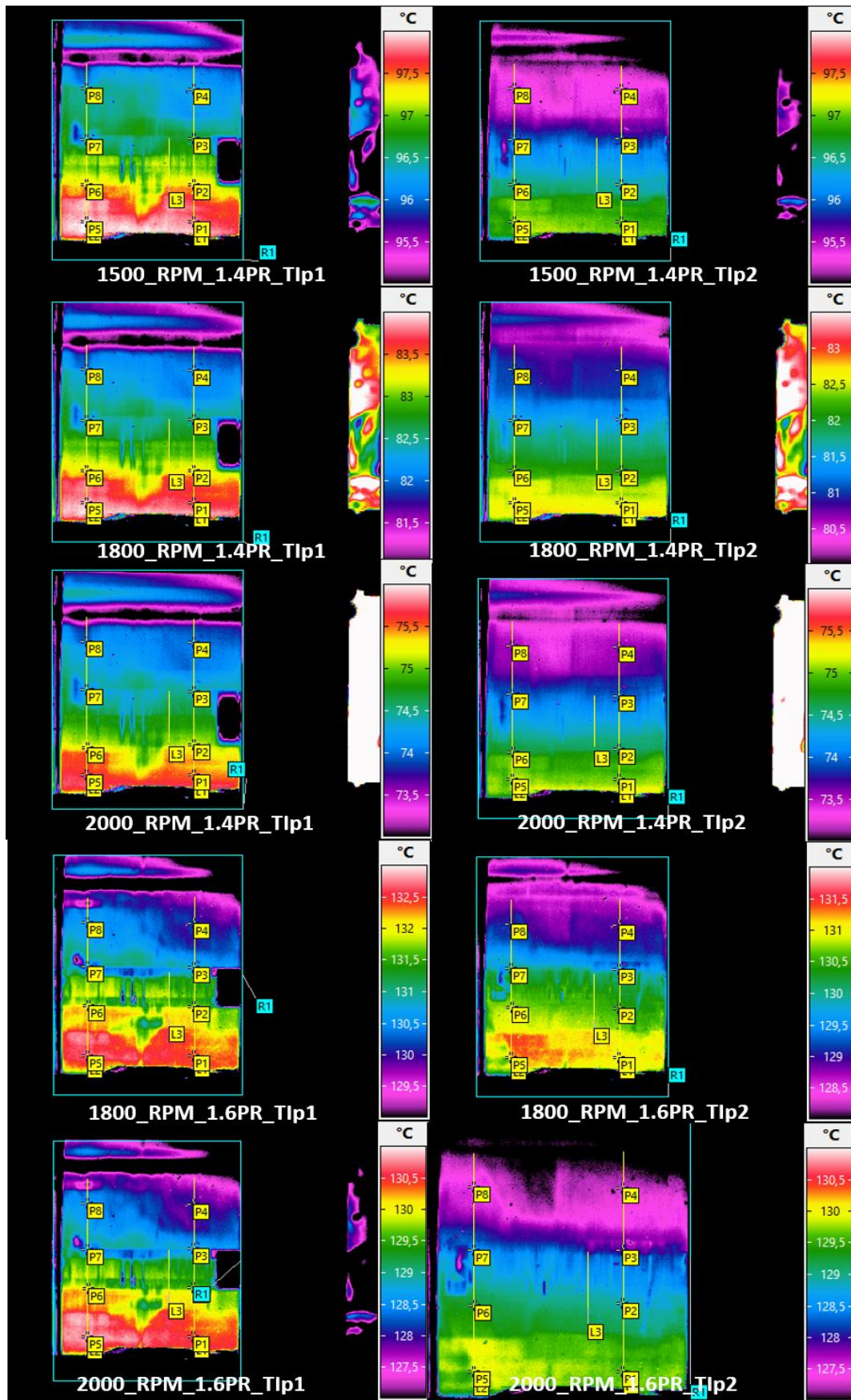


Figure 5.6 Thermograms of Tip1 and Tip2 at 1.4 PR and 1.6 PR various speeds obtained by averaging 500 instantaneous images represent surface temperature variation from high pressure side to low pressure side.

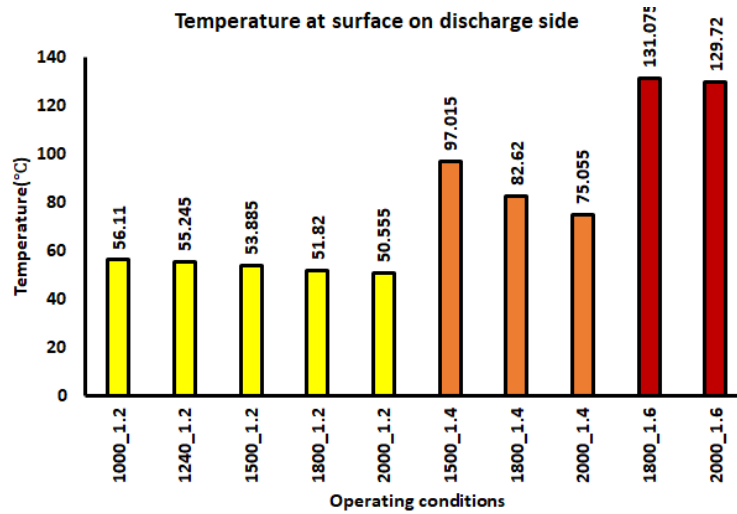


Figure 5.7 Temperature of lobe surface on discharge/high-pressure side obtained on the line from P1 to P5

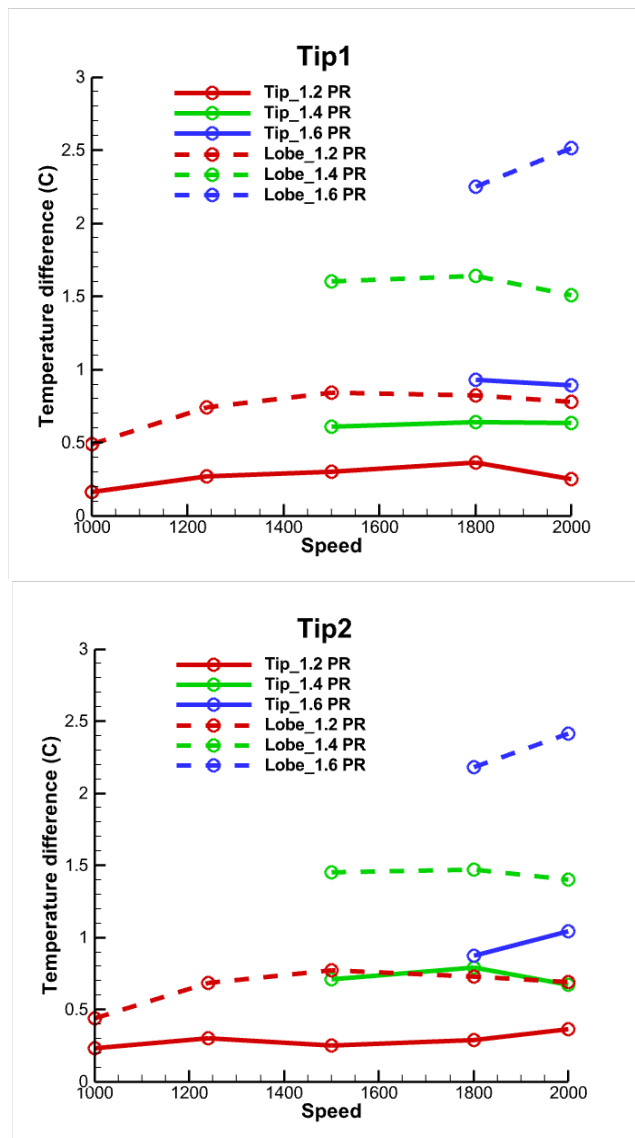


Figure 5.8 Surface temperature comparison of Tip1 and Tip2

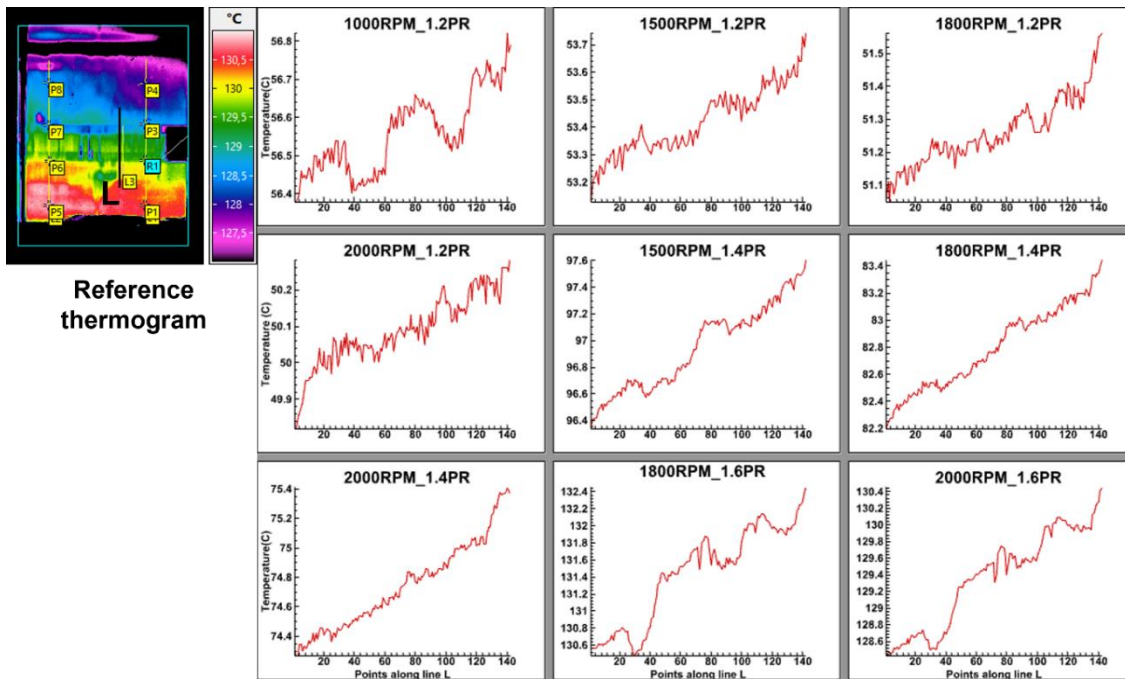


Figure 5.9 Temperature of lobe surface across the tip over the line L from suction to discharge for all operating conditions

Temperature measurement of the outside of the casing is also carried out to study the temperature distribution on the machine surface. The camera arrangement for this measurement is shown in Figure 5.4 (a). The black painted blower with the example of thermogram is shown in Figure 5.4 (b) & (c). Measurements are carried out at the same operating conditions as listed in Table 5.1, machine was allowed to stabilize at each operating conditions after which the measurements are performed.

It is observed from the measurement (Figure 5.10) that over the entire surface, temperature is decreasing with the increase in speed at the same pressure ratio. The surface temperature is increasing with the increase in pressure ratio. It also indicates the effect of speed on casing surface temperature at the constant pressure ratio. High temperature spot is observed near the discharge port at Location R3. Temperature is decreasing when moving away from the discharge port, which is shown in Figure 5.11.

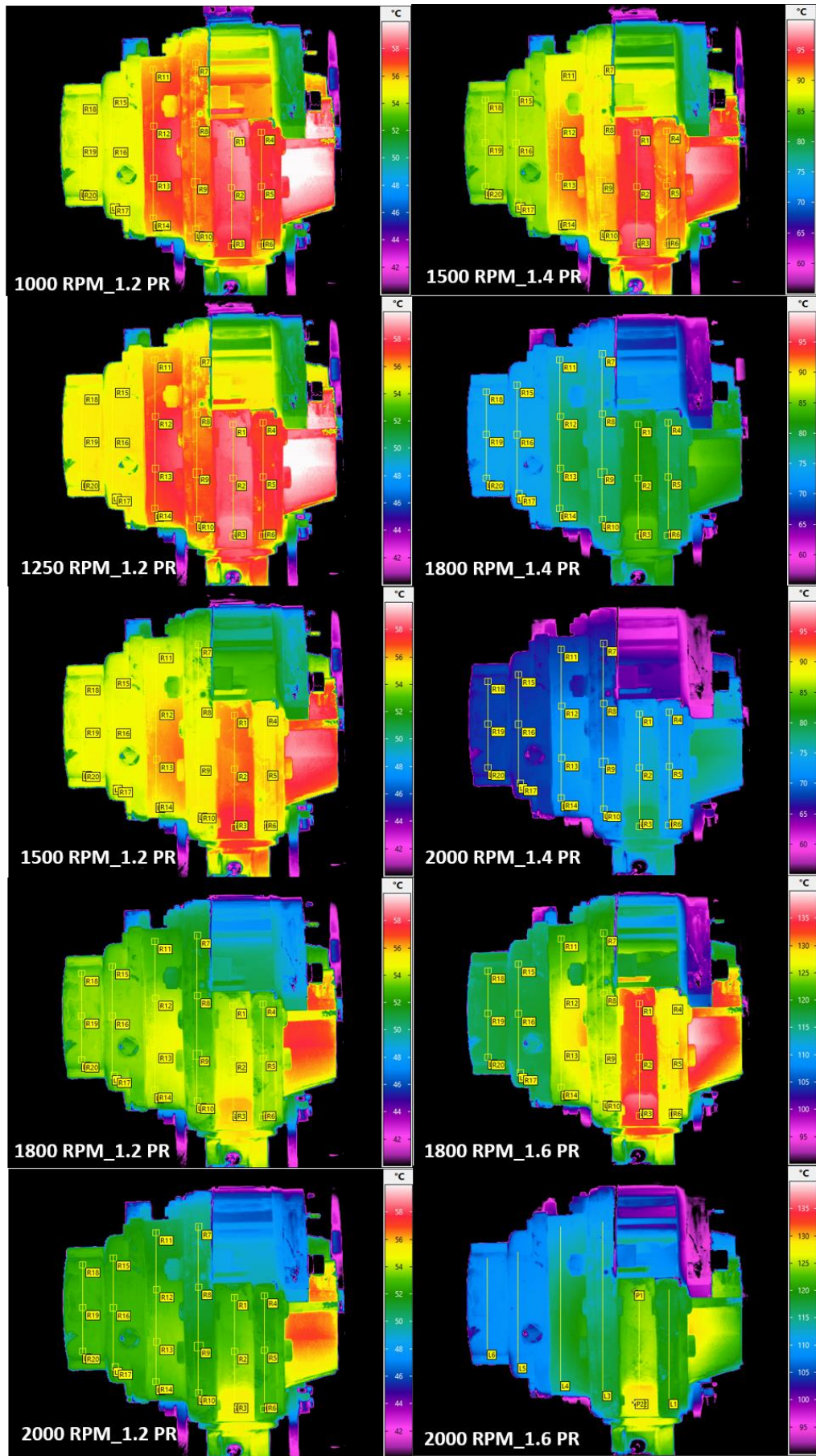


Figure 5.10 Casing temperature for 1000 RPM to 2000 RPM and 1.2PR to 1.6PR

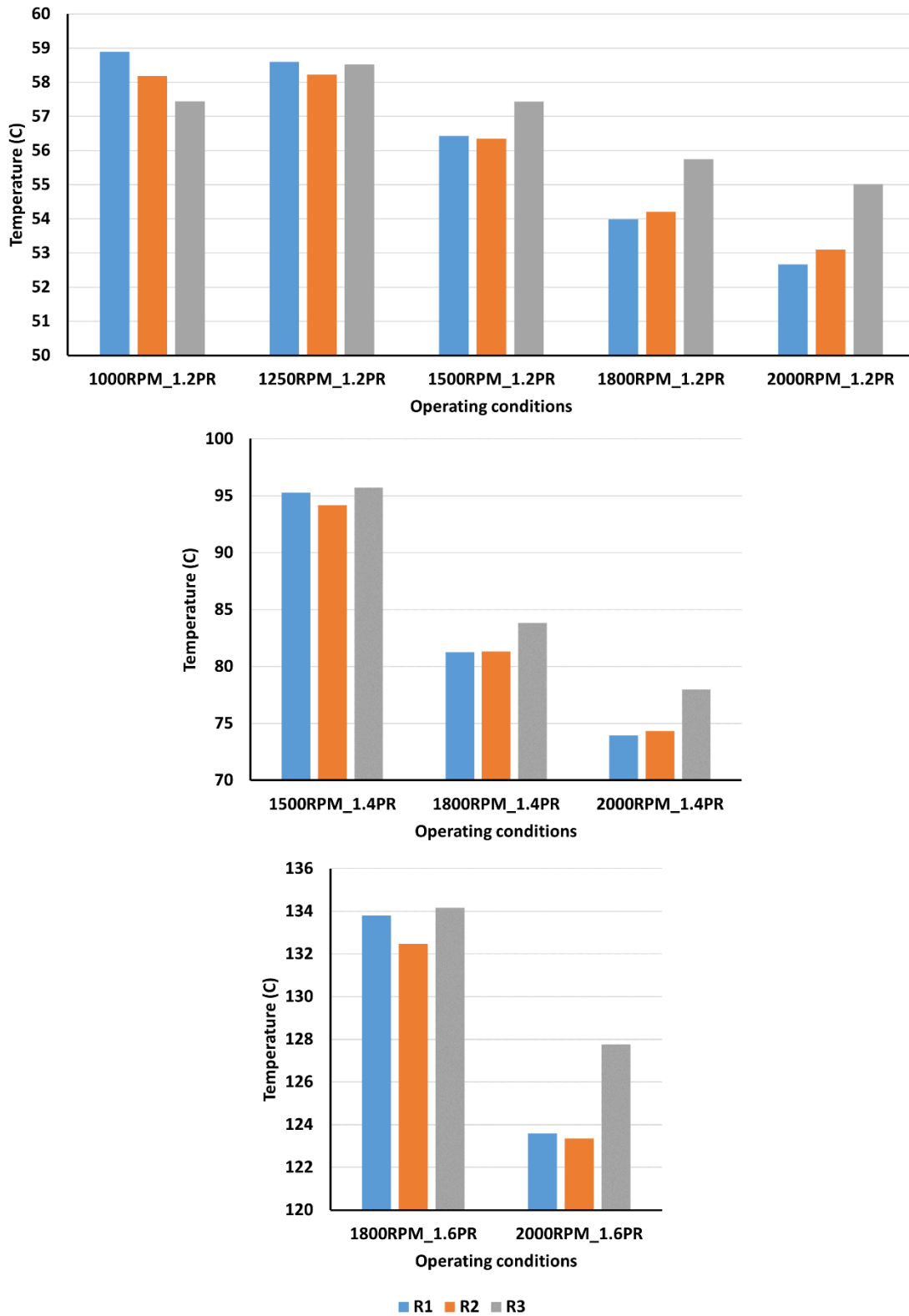


Figure 5.11 Temperature over location R1, R2, R3 at 1.2 PR, 1.4 PR and 1.6 PR

Transient measurements are carried out in the operating conditions of the machine to see the incremental behaviour of temperature over the entire casing surface.

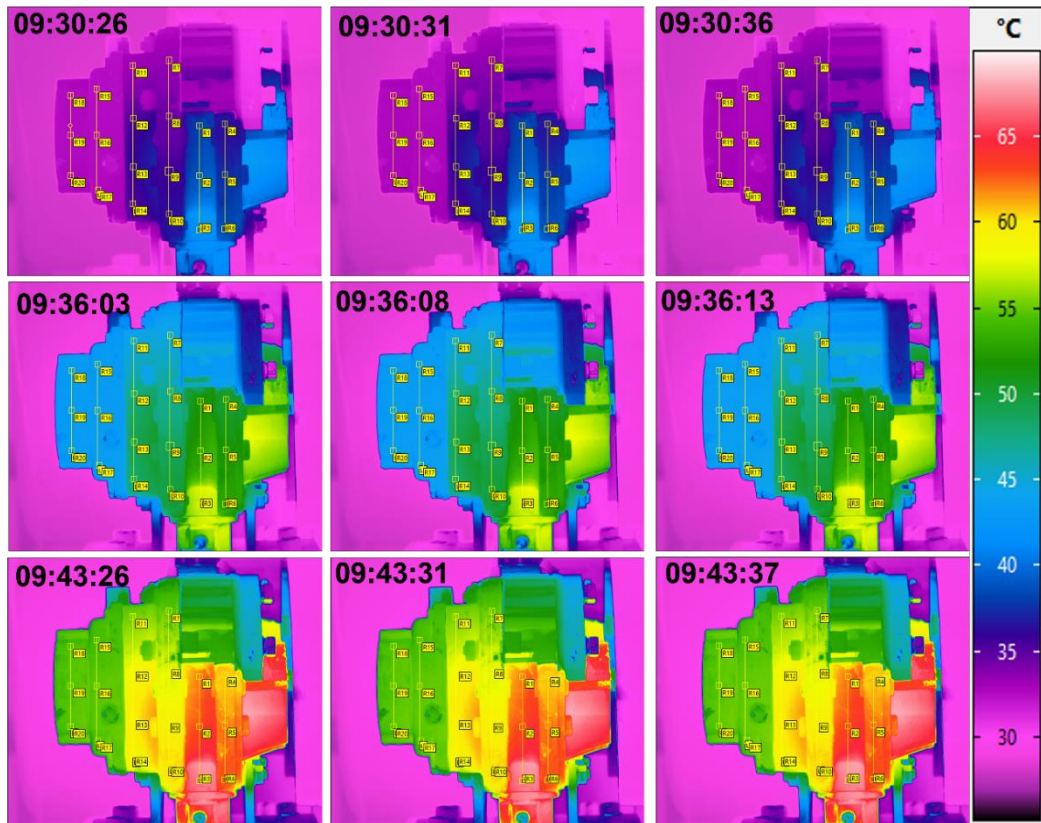


Figure 5.12 Temperature measurement at various time interval at 2000 RPM and 1.4 pressure ratio (Machine was started at 09:23:20)

Figure 5.12 shows temperature of the casing measured at various time intervals from the start of the experiment. It is clearly observed that temperature across the entire casing surface is increasing with time. Temperature near the discharge port is always higher and it is decreasing as points move away from the discharge. Gradual temperature increase is depicted in Figure 5.13.

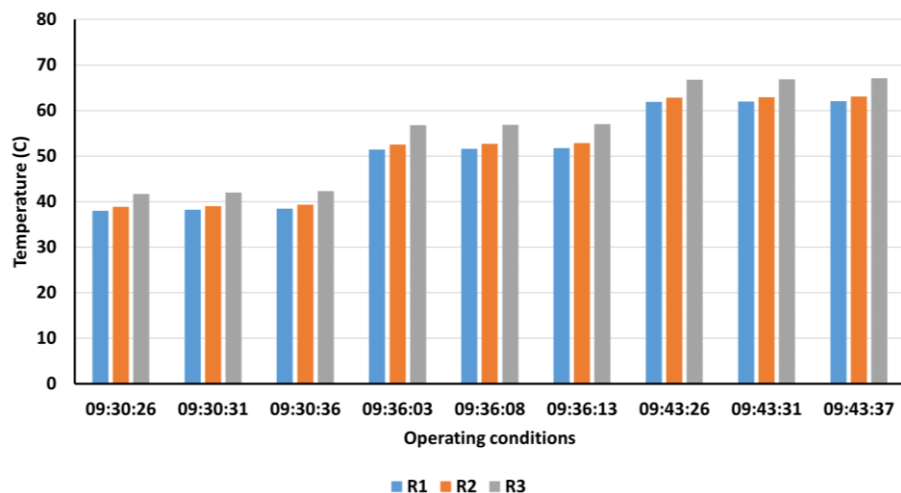


Figure 5.13 Temperature over the time at the location at R1, R2, R3 on casing surface at 2000RPM and 1.4 PR

5.3 Uncertainty in IR thermography measurements

Like any measurement technique, infrared thermography measurements are subject to various sources of uncertainty that can affect the accuracy, precision, and reliability of the results. These uncertainties can arise from factors such as emissivity variations, camera settings and calibration, motion blur. Therefore, it is essential to properly quantify the uncertainties associated with infrared thermography measurements.

below listed parameters contributes to the error in infrared thermography measurements,

1. Calibration uncertainty components in temperature measurement thermal imaging camera: This is the uncertainty mentioned in the calibration certificate, it is $\pm 1\%$ Range full-scale for camera used in this measurement. This uncertainty can be considered a normal distribution. Uncertainty is given at a 95% confidence level, with coverage factor $k = 2$, so divisor 2 is necessary to obtain standard uncertainty.

2. Thermal imaging camera equipment uncertainty due to multiple effects: Drift, linearity and stability can be considered. Employed camera for measurement has a cooled detector that is why drift is neglectable and stability is very high. While the non-linearity is covered by the calibration

3. Digital display resolution uncertainty and uncertainty due to detector electronics are covered in calibration as well.

4. Uncertainty due to the determination of the object's emissivity: It is important uncertainty component, and it is determined for the used experimental setup.

5. Uncertainty due to atmospheric transmission: normally this is neglectable for lab conditions (normal air) and we do not have special gases involved that damp the signal. Damping from normal air only applies for long range shots over 10 m distance.

6. Uncertainty due to motion blur: Motion blur is one of the factors that can contribute to uncertainty in infrared thermography measurements. Motion blur occurs when there is relative motion between the object being measured and the infrared camera during the measurement. This can cause the image of the object to appear blurred or distorted.

To convert the uncertainty of emissivity to temperature, we need to consider the impact of emissivity uncertainty on the measured temperature. It can be calculated by equation 5.1.

$$T_{\varepsilon} = \frac{\varepsilon * \Delta\varepsilon * T}{1 - \varepsilon * \Delta\varepsilon} \quad 5.1$$

where, T_{ε} is the uncertainty in temperature due to emissivity uncertainty, ε is the emissivity of the material being measured, $\Delta\varepsilon$ is the uncertainty in emissivity and T is the

temperature of the object being measured. In this study, emissivity of surface is 0.95 with applied matte black paint, variation in emissivity is 0.005 and maximum measured temperature is tabulated in Table 5.3. This component is considered the upper and lower limits in rectangular distribution.

Uncertainty in temperature due to motion blur can be calculated by equation 5.2,

$$T_b = \frac{k * v' * t * \Delta x}{L} \quad 5.2$$

where, T_b is the uncertainty in temperature due to motion blur, k is a proportionality constant, v' is the velocity of the object being measured, t is the exposure time of the camera Δx is the distance that the object moves during the exposure time, L is the length of the object that is imaged by the camera. Exposer time of camera is 187 μ s during the measurement. This component is considered the upper and lower limits in rectangular distribution.

Table 5.2 Uncertainty components in measurement by infrared thermography

Uncertainty sources	Value (°C)	Distribution	Divider	Standard uncertainty(K)
Camara calibration	T_{cal}	normal	2	$u(T_{cal}) = \frac{T_{cal}}{2}$
Emissivity	T_ε	rectangular	$\sqrt{12}$	$u(T_\varepsilon) = \frac{T_\varepsilon}{\sqrt{12}}$
Motion blur	T_b	rectangular	$\sqrt{12}$	$u(T_b) = \frac{T_b}{\sqrt{12}}$

Table 5.2 shows uncertainty components to be applied in measurement by infrared thermography. The combined standard uncertainty obtained for this measurement is calculated from equation 5.3, and the expanded uncertainty with coverage factor 2 from equation 5.4 [58]. Certainly, uncertainty depend upon motion blur and measured maximum temperature, calculated combined uncertainty at various measurement conditions are presented in Table 5.3. It is depicted that uncertainty ranges from $\pm 0.63^\circ\text{C}$ to $\pm 1.37^\circ\text{C}$. Temperature measured at same pressure ratio and various speed lies between uncertainty range but these measurements are still acceptable and valid because at the same time, temperature of air measured using RTD at the discharge of the Roots blower has same trend which is shown in Figure 5.14.

$$u(T_{ir}) = \sqrt{u(T_{cal})^2 + u(T_\varepsilon)^2 + u(T_b)^2} \quad 5.3$$

$$U(T_{ir}) = 2 u(T_{ir})$$

5.4

Table 5.3 Uncertainty at various measured condition

Speed	Pressure	IR measured maximum temperature	$U(T_{ir})$
1000	1.2	56.11	0.68
1240	1.2	55.24	0.67
1500	1.2	53.88	0.66
1800	1.2	51.82	0.64
2000	1.2	50.55	0.63
1500	1.4	97.01	1.04
1800	1.4	82.62	0.91
2000	1.4	75.05	0.84
1800	1.6	131.07	1.37
2000	1.6	129.72	1.35

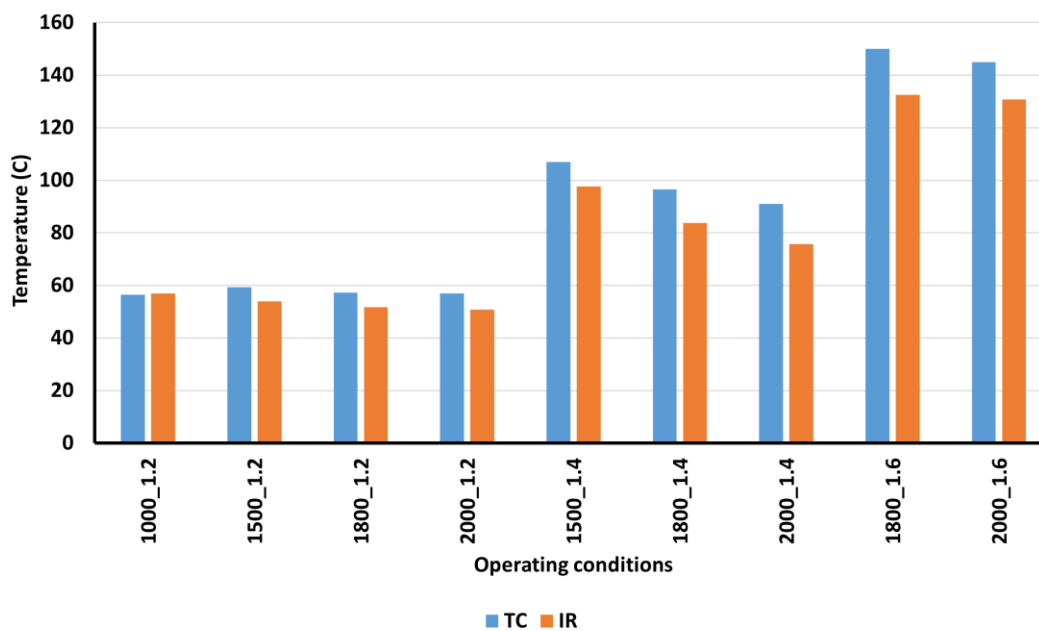


Figure 5.14 Comparison between measured temperature at discharge by thermocouple (TC) and measured temperature by infrared thermography (IR)

5.4 Summary

This chapter focuses on the IR thermography experimental study. The chapter begins with a description of the IR thermography experimental setup and procedures, including the setup of the IR thermography equipment and the experimental procedure for conducting the measurements. Obtained results of surface temperature measurements are discussed and finally, the chapter discusses the uncertainty associated with the IR thermography

measurements and presents an analysis of the possible sources of uncertainty. Next chapter describes PIV experimental study.

Chapter - 6 PIV Experimental Study

This chapter describes the experimental setup of PIV along with experimental procedures. It also discusses the measurement results and the uncertainty associated with the measurement.

6.1 PIV experimental setup and procedure

The PIV experimental setup is using the laser, high speed camera, optics and software from Dantec Dynamics, UK.

6.1.1 DAQ system

As shown in Figure 6.1, the same test rig used for PLIF test is also used for PIV. However, in the PIV experiments, seeding particles such as smoke were supplied at suction instead of fluorescence particles. New National Instrument-based data acquisition system is built for this PIV setup. The LabView FPGA (Field programmable gate Arrays) based programming is done to capture real-time measured data. An additional trigger mechanism is programmed to use signal from the shaft encoder for phase-lock. The detailed description of used sensors and respective National Instruments modules are listed in Table 4.2 and Table 6.1.

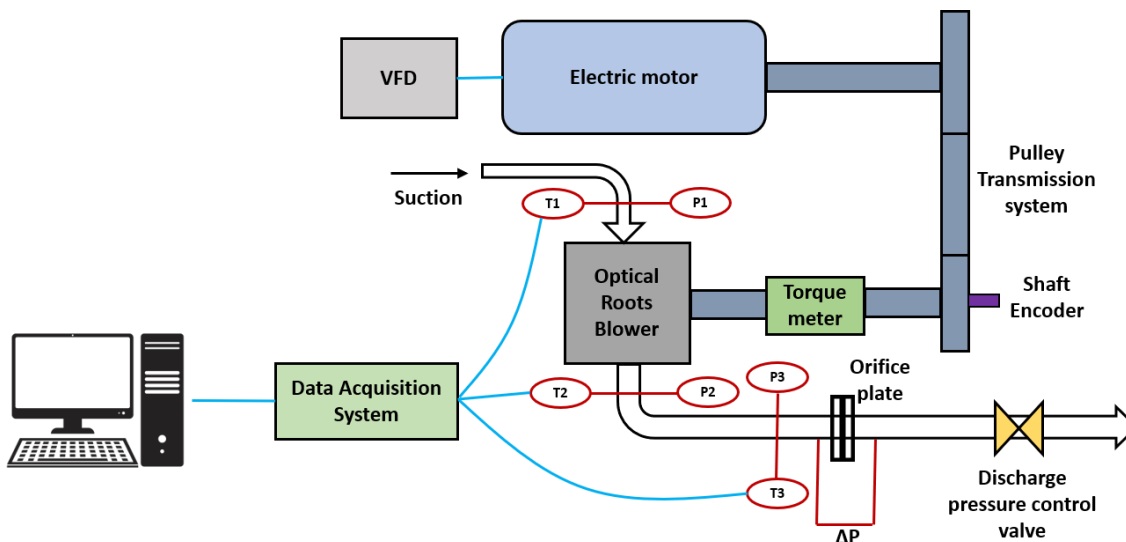


Figure 6.1 Schematic diagram of Roots blower test rig

Table 6.1 Specifications of the national instrument modules

NI Module	Measuring instrument
cRIO-9056, 1.33 GHz Dual-Core, Artix-7 75T FPGA, 8-Slot, RT, Non-XT	cRIO

NI 9401 8-Channel, 100 ns, TTL Digital Input/output Module	Shaft Encoder (Speed)
NI 9201 Spring Term, +/-10 V, 12-Bit, 500 kS/s, 8-Ch AI Module	Pressure sensors
NI 9212 MiniTC, 8 Ch-Ch Isolated, 24-bit TC Input C Series Module	Thermocouples
NI 9205 Spring Terminal, 32 Ch, +/- 200mv to +/-10v, 16-Bit, 250 Ks/S Ai C Series Module	Pressure sensors
NI 9216 Spring, 8-Ch RTD, PT100, 24-bit, 50S/s/ch AI module	RTD
NI 9237 4-Ch 50 kS/s/Ch, 24-Bit Bridge AI Module	Torque meter

The assembly of NI modules with NI cRIO-9056 is shown in Table 6.1. Various voltage supplies such as 24V, 12V, 10V and 5V are used to power up cRIO, pressure transducers, torque meter and shaft encoder, respectively. The electric box of power supply is kept separate to avoid any influence of electrical noise to the measured signal.



Figure 6.2 DAQ system with Power supply unit

6.1.2 Functional devices and seeding particles

6.1.2.1 Laser

The laser selected for this experiment was a 532 nm Litron Bernoulli laser, it is a dual pulsed laser common for PIV applications. Its maximum output energy is about 200mJ per pulse at frequency of 15Hz. This laser has a pulse-to-pulse energy stability better than 2% RMS. Figure 6.3 shows Laser with specification which was selected for the experiment.



Model	Bernoulli 200-15 PIV
Wavelength (nm)	532
Repetition Rate (Hz)	0-15
Pulse Energy (mj) ⁽¹⁾	200
Pulse Stability (±%)	2
Pulse Length (ns) ⁽²⁾	≤10
Near Field Beam Diameter (mm)	6.5
Beam Divergence (mrad) ⁽³⁾	<3.5
Shot-to-Shot Pointing Stability (μrad)	<100
Far Field Beam Overlap (μrad)	±100
Near Field Beam Overlap (μm)	±100
Polarisation	Linearly polarised, vertical plane
Spectral Purity (%)	>99.5
System Requirements	
Voltage (VAC)	110-250 (50-60Hz)
Power	Single Phase
Operating Ambient (°C)	5-35
System Data	
Laser Head Sealing ⁽⁴⁾	IP67
Laser PSU Sealing	IP21
Power Supply	LPU550B

Figure 6.3 Litron Bernoulli laser with specifications

6.1.2.2 Camera

In order to measure velocity fields using PIV technique, a double shutter camera HiSense zyla 5.5 MP camera, 8 bit having resolution of 2560 by 2160 pixels has been chosen from Dantec Dynamics. This camera is also suitable for PLIF measurements. It requires special attention during the connection of the cable and the frame grabber installation. Figure 6.4 shows HiSense Zyla 5.5 MP camera.



Figure 6.4 HiSense Zyla Camera (Dantec Dynamics)

Table 6.2 Characteristics of the selected PIV camera

Camera	Speed (8 bit) (fps)	Res. (MP)	Sensor resolution (Pixel x Pixel)	Interframe time (ns)	Pixel Size (μm)	Pixel depth (bit)	Lens Mount (type)
HiSense Zyla	40	5.5	2,560 x 2,160	150	6.5	12	F

6.1.2.3 Synchronizer and software

A high-performance synchronizer is selected together with an encoder input for cyclic synchronizer, and the software used for processing is Dynamic Studio with 2D PIV add

on. The synchronizer shown in Figure 6.5 has an important role for communication between the camera, laser, and the software. The timing setup of the camera and the laser pulse need to be adjusted carefully so that laser pulse coincides accurately with the camera capture.



Figure 6.5 Synchronizer

6.1.2.4 Optics

It is necessary to use laser optics to illuminate the flow field in a controlled manner as well as safely. The long light guide arm (2100mm) suitable for 532 and 266nm wavelength is selected to transfer the laser beam from the laser head to the area under consideration. In addition, a laser sheet optics is required to convert the laser beam to a laser sheet. For that, the UV Parallel Light Sheet Optics and beam waist adjuster are chosen. Figure 6.6 shows the light guide arm and the parallel optics.

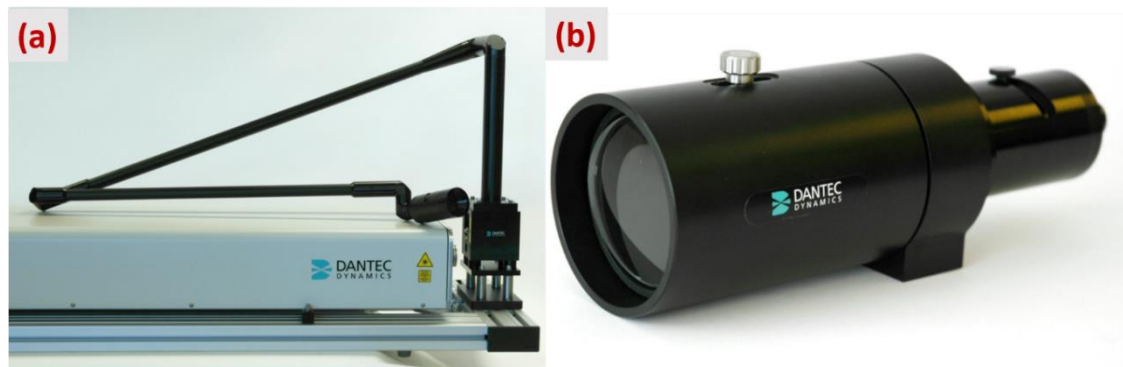


Figure 6.6 (a) Light guide arm (b) parallel optics

To get the better view of the clearance gap, it is decided to use a standard Distamax microscopic lens available with the Aeronautics department of City, University of London. It was also planned to replace the standard objective with a CF4 lens to get higher magnification.

6.1.2.5 Particles and Seeder

It was decided to try DEHS (Di-Ethyl-Hexyl-Sebacic) particles as a tracer for this study. The flow was seeded using Liquid Seeder (type FT700CE). Another option is to use

smoke of liquid glycol as a seeder. In the beginning the images were checked by seeding both each of particles separately to choose best fit for this application. Experiments were carried out using smoke because DEHS particles were depositing on the glass window in very short period of time which makes recorded images blurred.

6.1.3 Particle image velocimetry setup

It is required to have an optical access of the clearance gap for PIV, which requires an optical element transparent to 532nm light wavelength. For the present application it has to withstand temperatures and pressures of up to 200 °C and 3 barg respectively. Fused silica glass is the best suitable material which meets these requirements and same optical access arrangement as PLIF (Figure 4.3) is used for PIV.

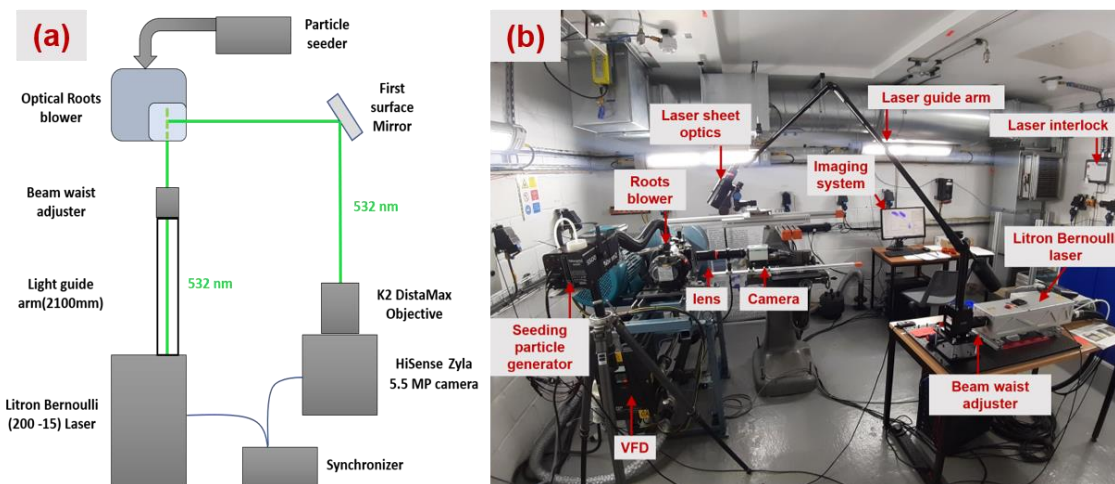


Figure 6.7 (a) PIV experiment setup layout (b) Actual PIV setup

Schematic of the designed PIV setup and the image of an actual PIV test setup is shown in Figure 6.7. Dual pulse Litron Bernoulli laser with 532nm wavelength is used. For imaging, HiSense zyla 5.5 MP camera with K2 DistaMax standard objective is used to obtain appropriate magnification of the small clearance gap. High performance synchronizer is used along with the encoder input for the cyclic synchronizer to trigger the laser and obtain an image at the same time precisely. A long light guide arm (2100mm) suitable for 532 and 266nm wavelength is selected to transfer the laser beam from the laser head to the area under study. In addition, laser sheet optics is required to convert the laser beam to a laser sheet. For that UV/Visible parallel light sheet optics and the beam waist adjuster were implemented. In this study smoke particles seeded using smoke generator are used as the tracer.

The flow was seeded with 0.2 – 0.5 μm diameter smoke particles generated using glycol-based liquid. The flow tracking ability of the seed was validated using the particle Stokes number,

$$St = \frac{\rho_P U_F d_P^2}{\mu_F L_F} \quad 6.1$$

Where, St is Stokes number, ρ_P is particle density, U_F is fluid bulk speed, d_P is particle diameter, μ_F is dynamic viscosity of the fluid and L_F is characteristic length of the flow. Calculated Stoke number for used particles is less than 1, so particles follow the fluid streamlines closely.

6.1.4 PIV measurements

PIV data are captured at and around the clearance gap. Figure 6.8, shows the measurement plane for PIV data recording which is projected 20mm from the face of the lobe inside the flow domain. Dimensions of the tip are presented in the inset of the Figure 6.8.

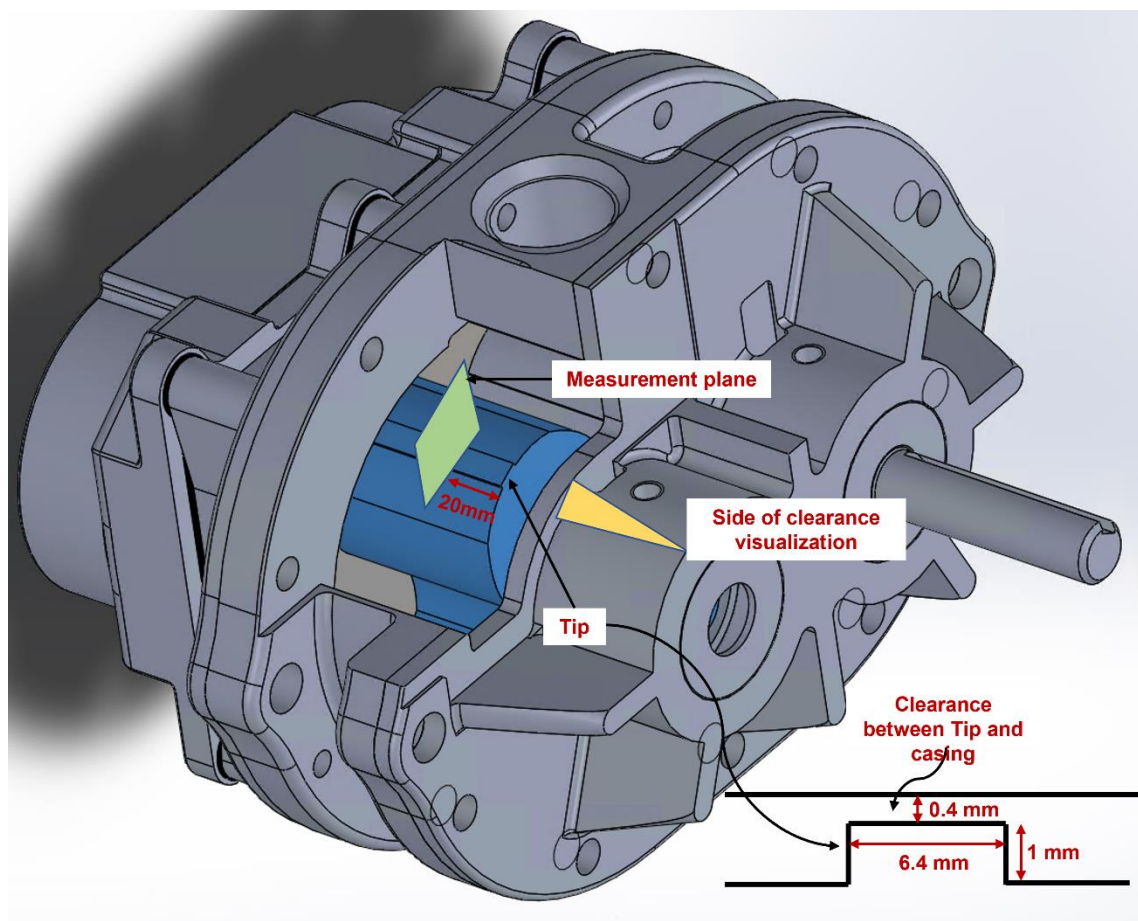


Figure 6.8 Measurement plane, position and tip step dimensions

As shown in the FOV (Field of view) in Figure 6.9, measurements are carried out at three different locations, using CF4 objective with K2-Distamax lens on camera. The primary

aim is to study the clearance flow, which required the camera to be focused at the tip and the flow field at two more areas. The first one is near the trailing edge side of the clearance which is connected with the suction chamber and the second is the leading-edge side of the clearance which is connected with the discharge chamber.

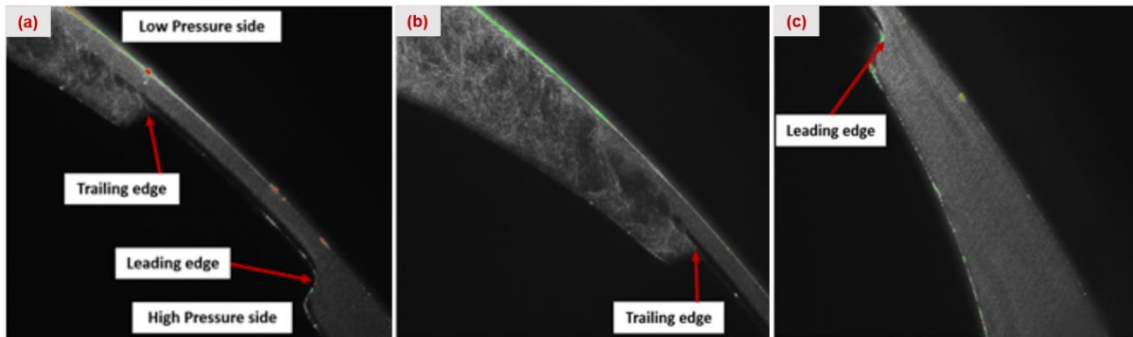


Figure 6.9 (a) FOV at clearance between tip and casing (b) FOV at trailing edge of clearance (c) FOV at leading edge of clearance

Measurements at all three locations are carried out at various machine operating conditions as listed in Table 6.3. Combinations of test conditions are created by varying machine speed from 1000 to 2000 RPM and pressure ratios from 1.2 to 1.6.

Table 6.3 Machine operating conditions

Speed (RPM)	Pressure Ratio
0	1.2
1000	1.2
1500	1.2
1800	1.2
2000	1.2
0	1.4
1500	1.4
1800	1.4
2000	1.4
0	1.6
1800	1.6
2000	1.6

All measurements are carried out at 45 degree of the crank angle and 20mm inside along the tip length. For each recording, minimum of 200 image pairs are captured. The time

interval between pulses (Δt) is kept at $0.2 \mu\text{s}$ for all measurements. Similarly, measurements are also carried out in the static condition (0 RPM) of the rotor. Rotor was locked at 45° angle and measurements are performed at three pressure ratios 1.2, 1.4 and 1.6 by generating higher pressure at the discharge port of the Roots blower.

6.1.5 PIV data processing

PIV data are recorded and post processed using Dynamic studio software from Dantec Dynamics. As per the principle of PIV technique, it is important to find out an optimal experimental setup before the actual test, as this is a trade-off between various setup parameters. It means experimental conditions should be carefully set to get desired aspect ratio of the flow. The size of the field-of-view (FOV) is the starting point for parameter selection. The number of pixels on the camera chip determines the spatial resolution and the number of vectors obtained. In this study the sensor size is 2560×2160 pixels. An adaptive window sizing is applied for the cross-correlation procedure. In this method, the window size was varied from 64×64 pixels to 32×32 pixels to maintain minimum of 8 particles in the window to calculate the vector with a 50% overlap during the cross-correlation procedure, as shown in Figure 6.12. An established rule-of-thumb is that the particle displacements between the first and the second frame should not exceed 8 pixels for the correlation. As a result, the time between the two consecutive laser pulses (Δt) has been adjusted to $0.2\mu\text{s}$. The light sheet width is 50mm and the centre portion of light sheet is focused on the FOV which is not more than 25mm wide. The uniformity of the light intensity is not so critical because it is not an intensity based measurement such as planar laser induced fluorescence[59].

Cross-correlation may sometimes lead to completely wrong velocity vectors. Therefore, pre-processing is performed on to the images to reduce the error of incorrect vectors. The minimum intensity is calculated from the ensembles of the 200 images and that was subtracted from each individual image to remove the background light. Raw image and image after subtracting background noise is shown in Figure 6.10.

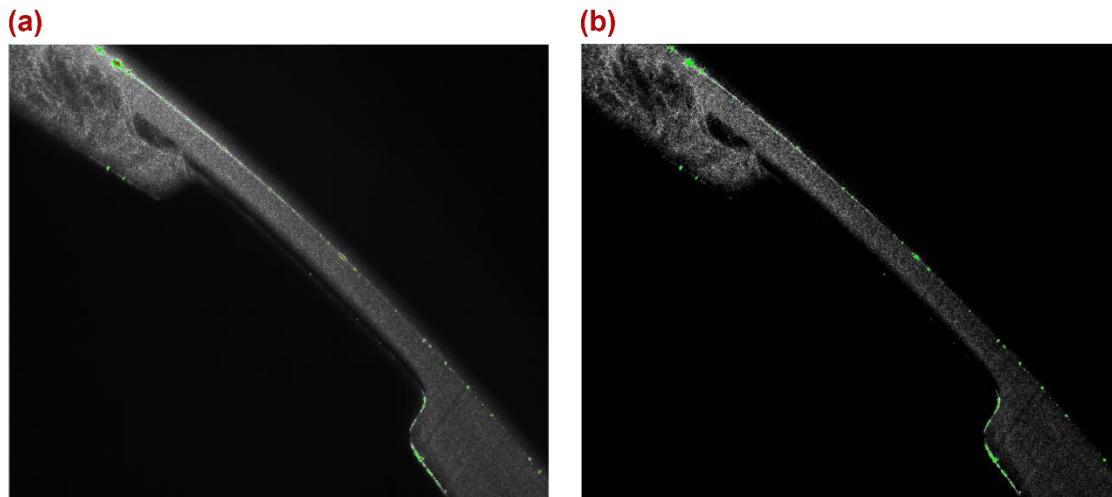


Figure 6.10 (a) Raw image (b) Image after subtracting background noise

PIV as an optical method requires calibration in order to derive pixel to pixel distance. In this case it is not possible to put calibration target, however, dimension of the object (tip of the lobe) is known which is used as a calibration. As shown in Figure 6.11, Point A and Point B are placed at the known distance of Tip length for scaling.

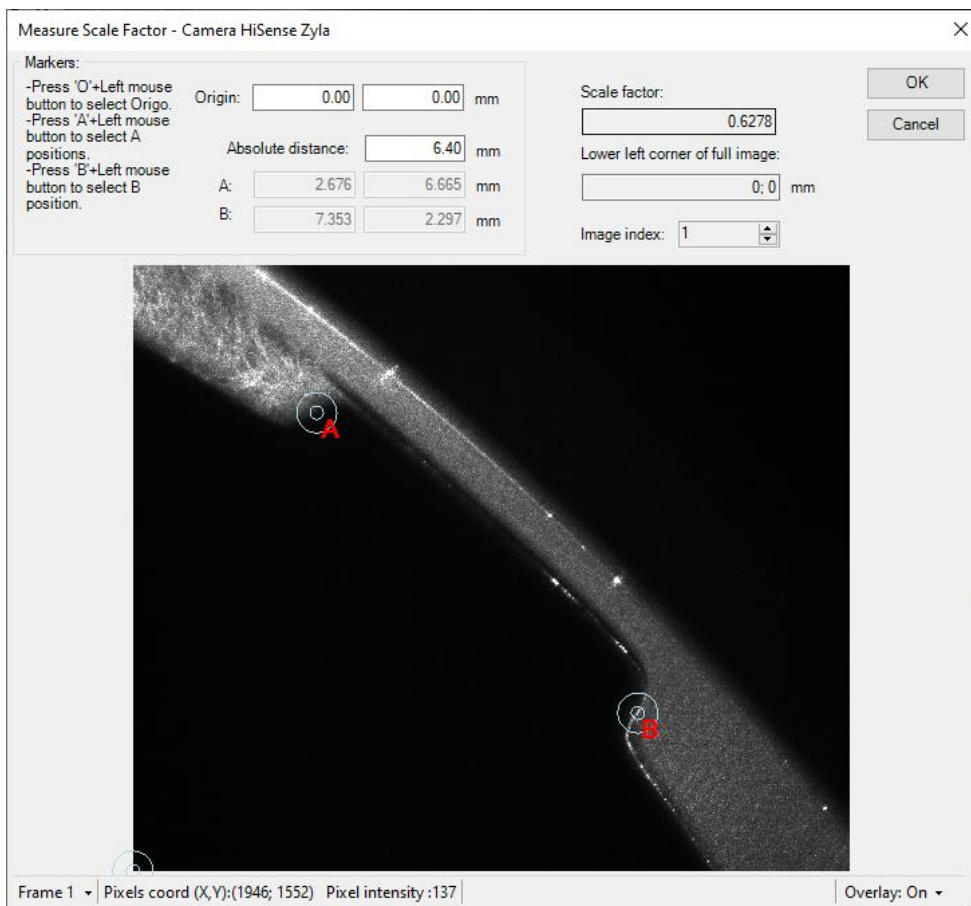


Figure 6.11 Scaling of PIV data

Pixel locking can cause the error in measurement as well, therefore, recorded images were evaluated to avoid pixel locking. Pixel locking is a bias error source, and it is a tendency

for the measured location and displacement of a particle image to be biased towards integer value. To improve the measurement results, coherence filter-based post processing is applied to the calculated raw velocity field. The coherence filter modifies a velocity vector if it is inconsistent with the dominant surrounding vectors. Figure 6.12 shows the cross-correlation method employed to derive velocity vectors. Based on rule of thumb it is required to have at least 8 to 10 particles inside the interrogation window.

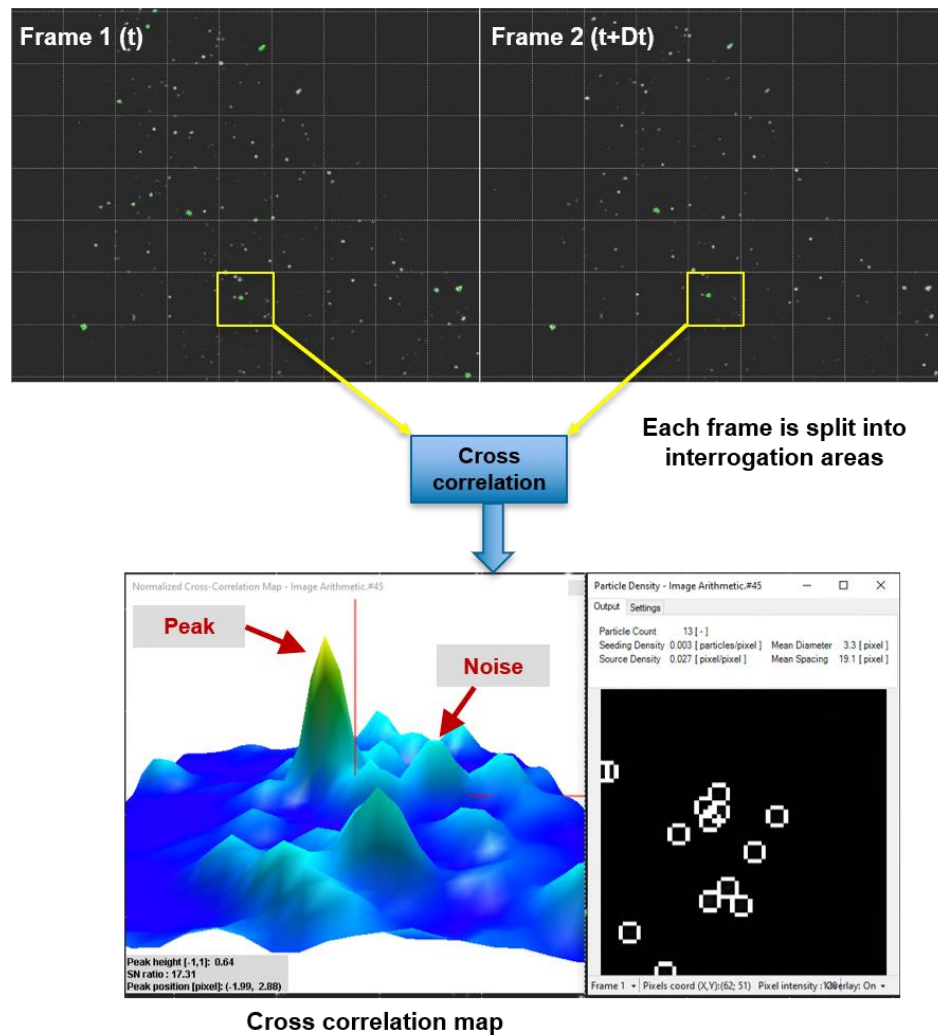


Figure 6.12 Cross correlation map for PIV

6.2 PIV measurements and results

This section is dedicated to the presentation of PIV measurements. It discusses observations from captured images, velocity field and other derived quantities at all three locations shown in Figure 6.13.

6.2.1 Measurement of the flow field in the clearance gap between the tip and casing

Firstly, recorded images are analysed to review the flow structure. Figure 6.13 shows the instantaneous raw images at various operating conditions. Seeded particles are not present over the near surface of the tip which is observed by black strip over the tip. It is because of the extremely high velocity gradient at the boundary of this void region, which is visible at the entrance of the tip, as indicated in Figure 6.13 by yellow circles. This high velocity flow is entering into the low-pressure chamber at the trailing end of the tip and is creating vortices. It is therefore interesting to analyse the velocity vector field in these regions.

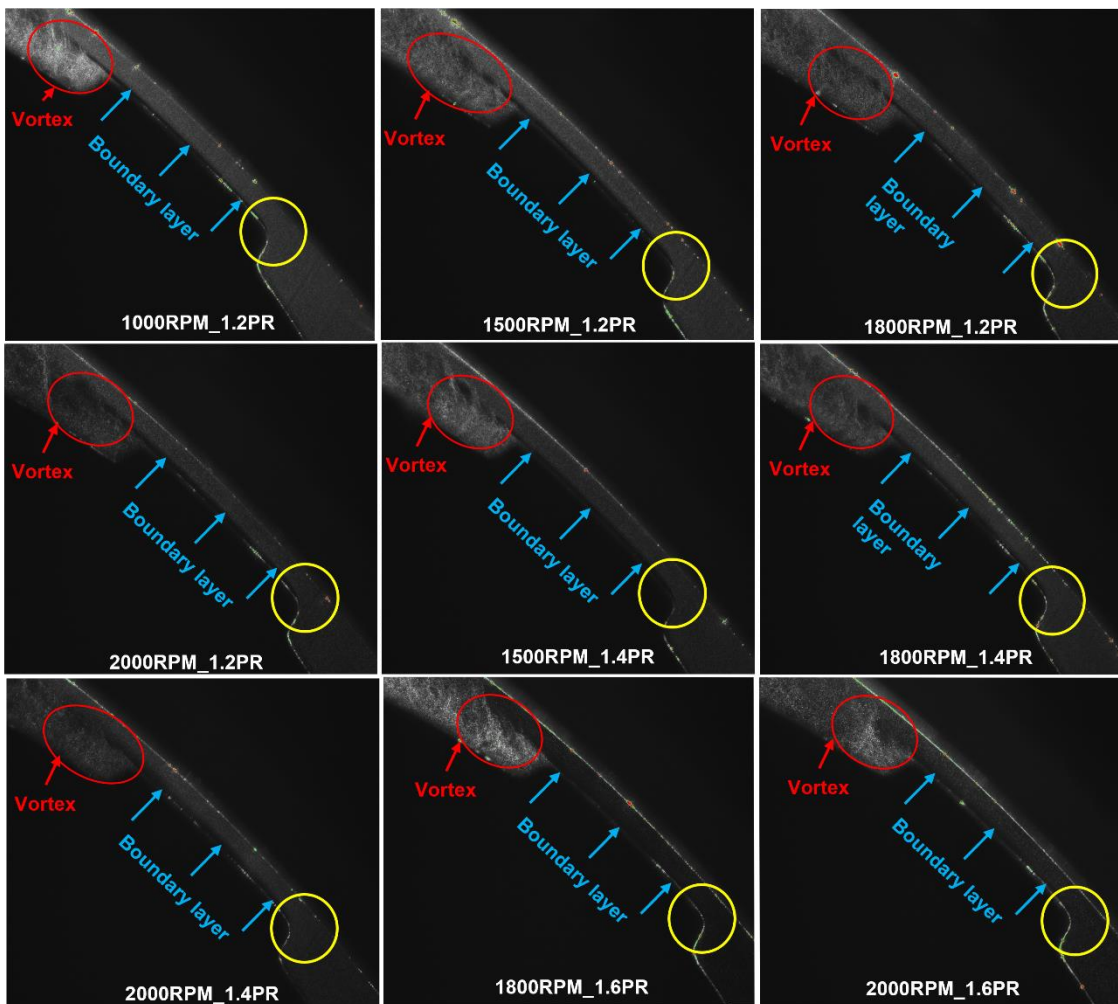


Figure 6.13 Raw images of flow field at various operating conditions

6.2.2 Results at the clearance between tip and casing

Velocity fields are obtained from the recorded image pairs as per the procedure described in section 6.1.5. Velocity fluctuations are calculated using Reynolds decomposition,

$$u' = u - \bar{u}$$

6.2

where, u' is velocity fluctuation, u is instantaneous velocity and \bar{u} is mean velocity.

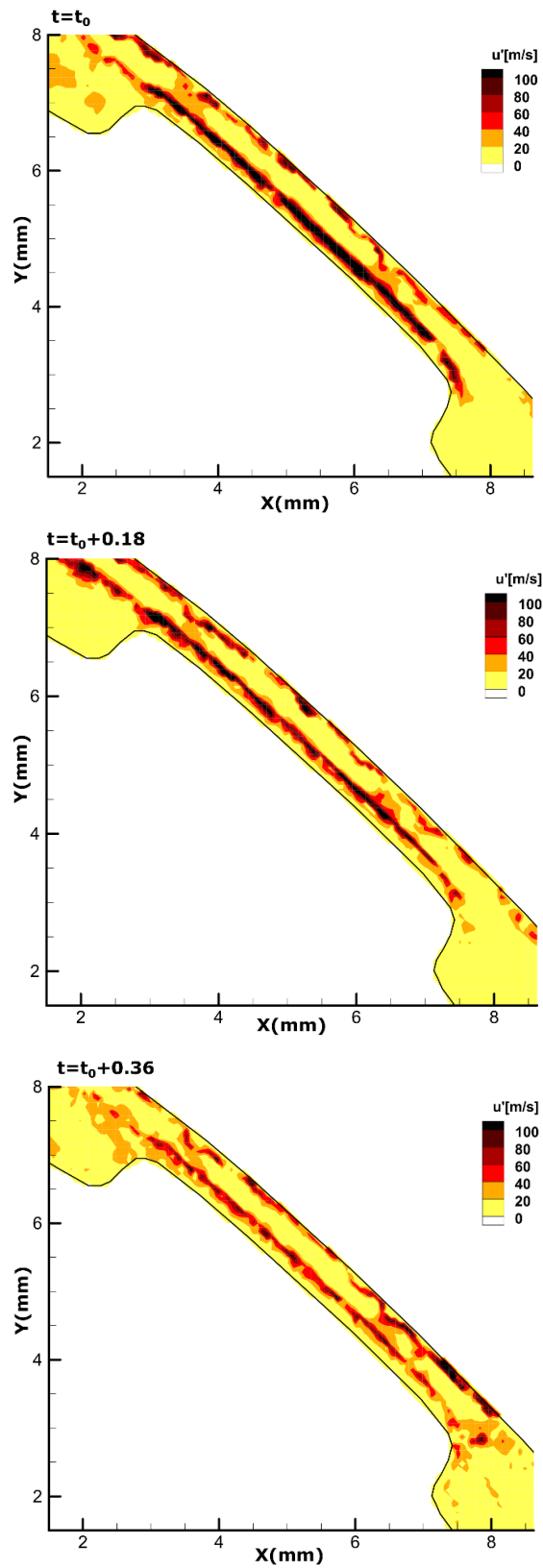


Figure 6.14 Velocity fluctuations in the streamwise region at reference frames: $t = t_0, t_0+0.18$ s, t_0+36 s for 1000RPM and 1.2PR

Velocity fluctuations at several reference frames for 1000RPM and 1.2 PR are shown in Figure 6.14. The high velocity fluctuations are observed in the region where the seeding particles start appearing above the tip. However, velocity pattern is in streamlines and very small fluctuation is observed in the middle of the tip and casing surface. This allows to derive mean velocity from the instantaneous vector fields to produce more informative vector plots.

Time averaged velocity plots are produced using 10 instantaneous vector fields for each measurement condition as shown in Figure 6.15 to Figure 6.17 for all operating conditions listed in Table 6.3. From the contours, it is clearly noticeable that velocity in the clearance gap is increasing with increase of pressure ratio. It is useful to perform statistical analysis to see the effect of speed and pressure difference on velocity within the clearance. For that, the average velocity is calculated at the exit of the tip using velocity profiles obtained from measured PIV data. Velocity near the surface of the tip was not measured using PIV because of the absence of particles in this region, so extracted velocity profiles just near to the surface doesn't represent true values. Therefore, integral average is carried out only on the true values of the profile in the clearance. Comparison of the average velocity is presented in Figure 6.18. It was found out that for the same pressure ratio, the velocity in the static condition is higher than velocities at all rotating condition. This shows the effect of the rotation of the lobe on the velocity in the clearance gap. As speed increases velocity in the clearance decreases. Also, with the increase in pressure ratio, difference between velocity in the static condition and rotating condition is getting smaller. Therefore, mass flow rate through clearance gap at the same pressure ratio will be different in stationary condition and rotating condition of the machine.

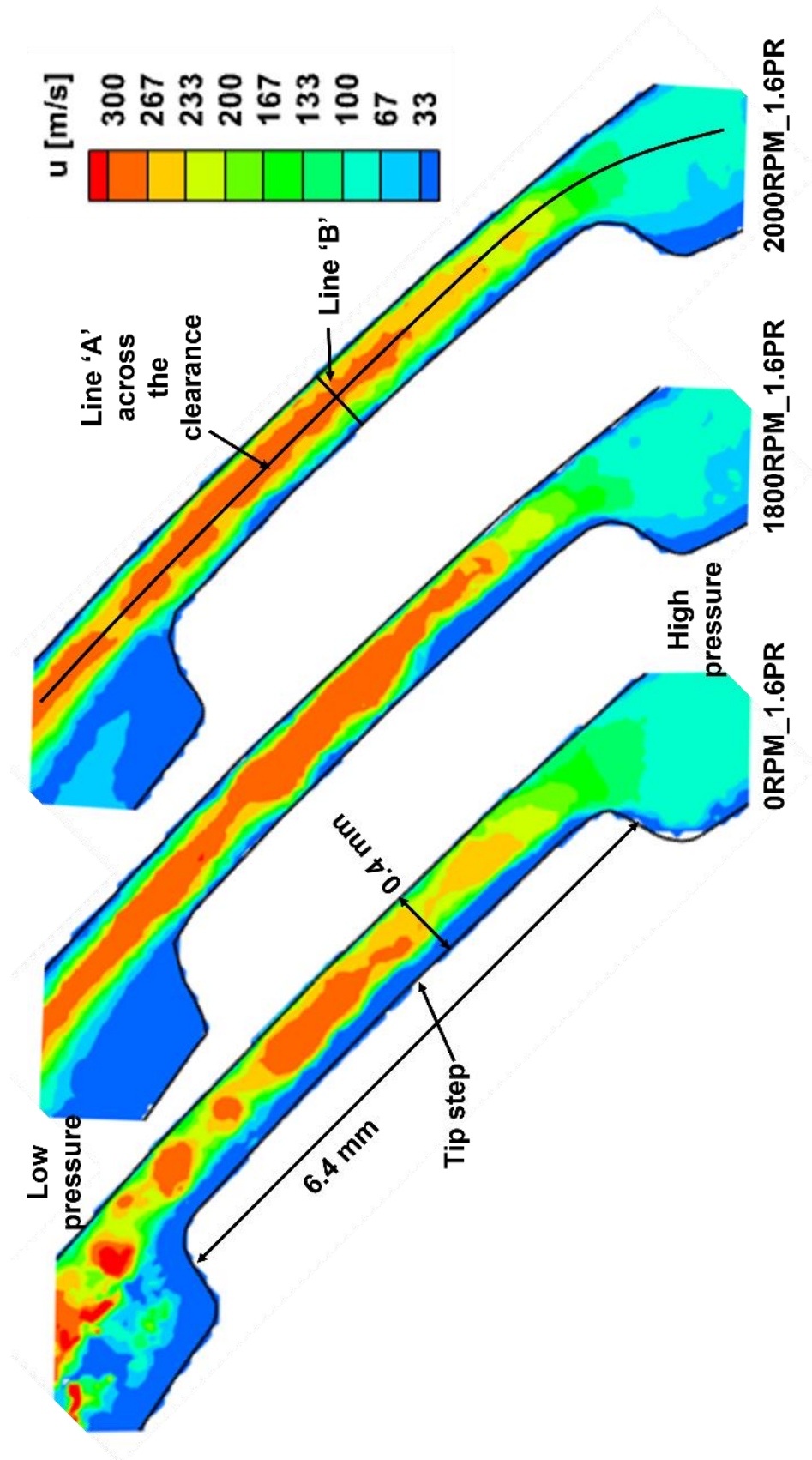


Figure 6.15 Time averaged velocity magnitude at 1.6 PR and various speeds

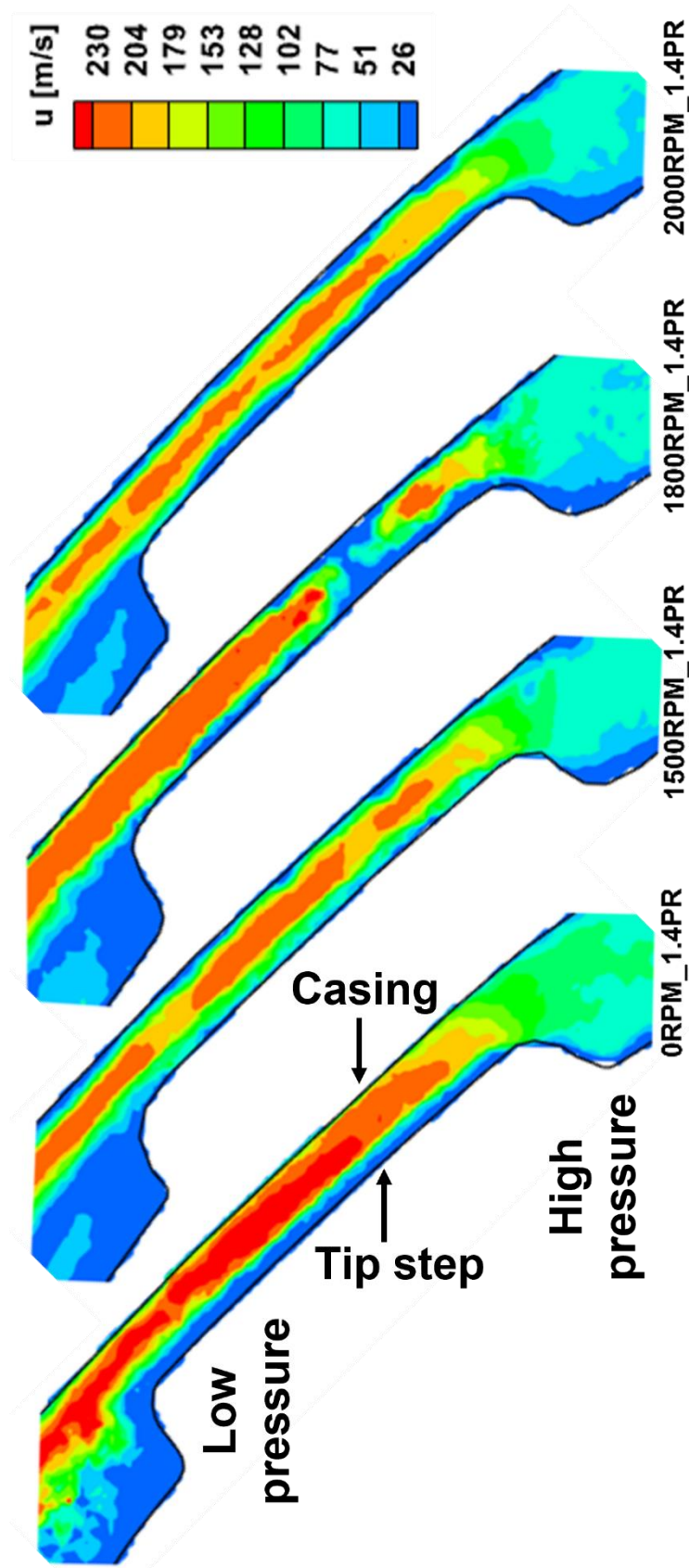


Figure 6.16 Time averaged velocity magnitude at 1.4 PR and various speeds

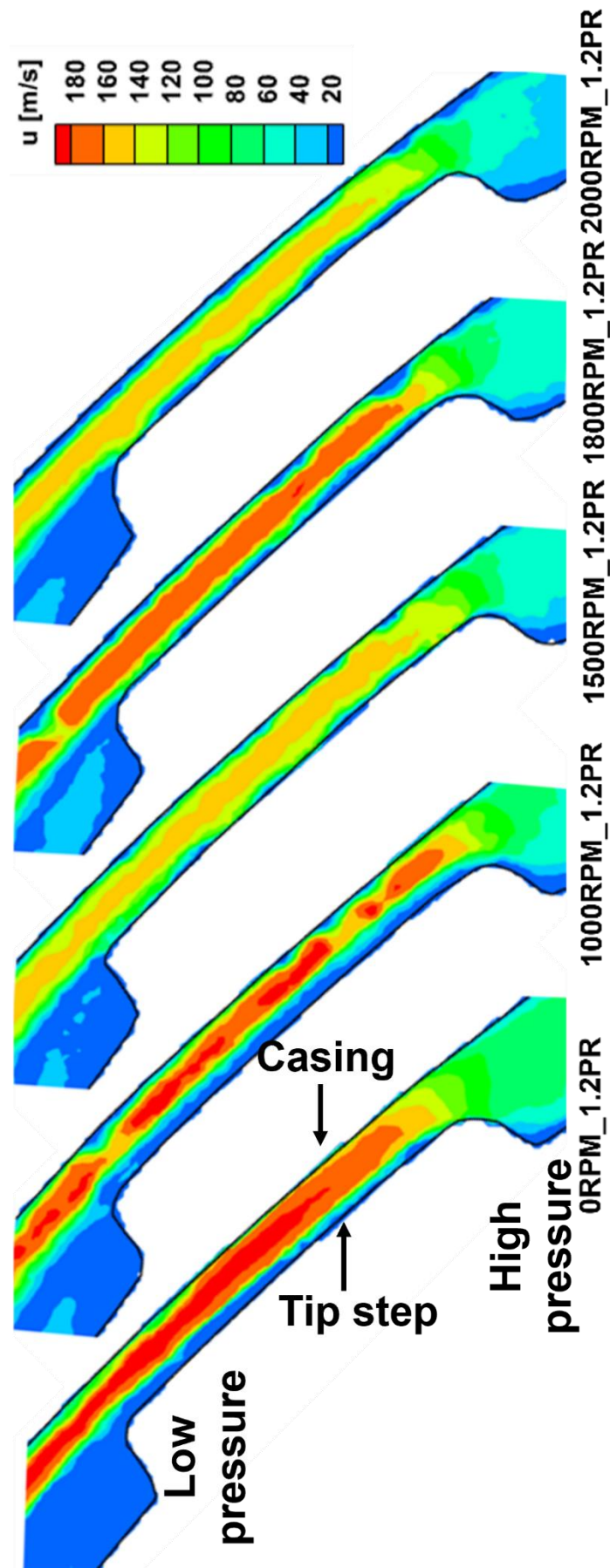


Figure 6.17 Time averaged velocity magnitude at 1.2 PR and various speeds

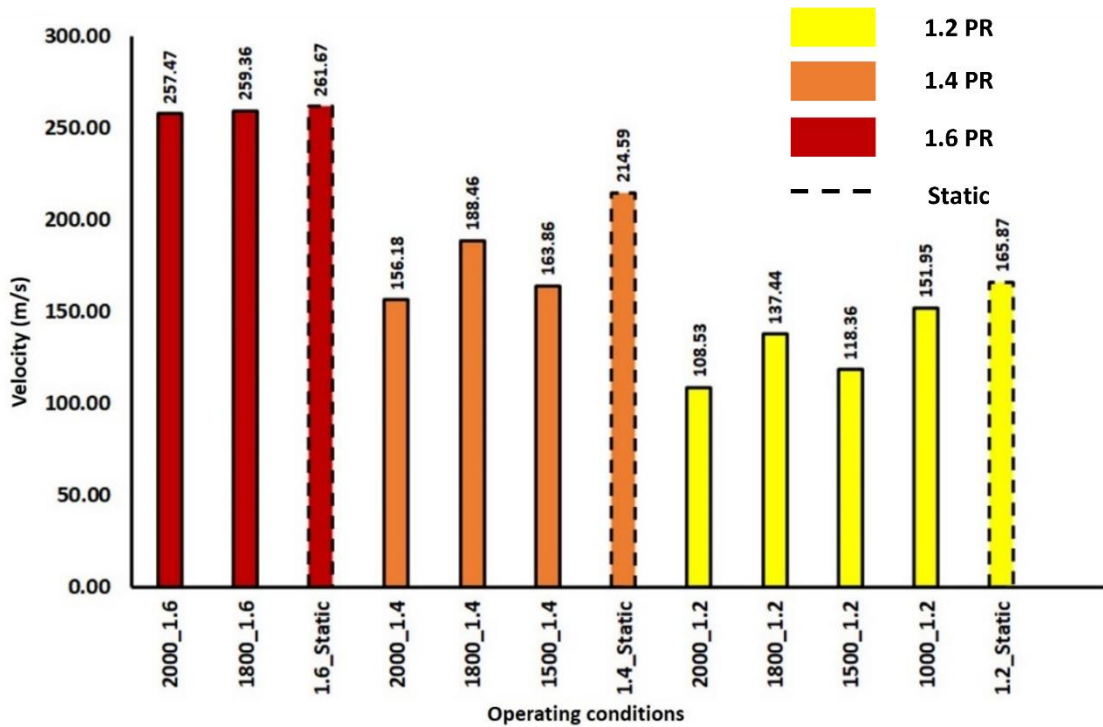


Figure 6.18 Comparison of the average velocity in the clearance gap at all measured conditions

Average velocity profiles plotted for all running conditions are shown in Figure 6.19. The maximum velocity is increasing with the increase in pressure ratio. It is interesting to note that the velocity profile in the static condition of the rotor is wider than in all running conditions. Velocity near the casing wall is higher in static conditions. This, it confirms that the rotational speed has influence on velocity inside the clearance.

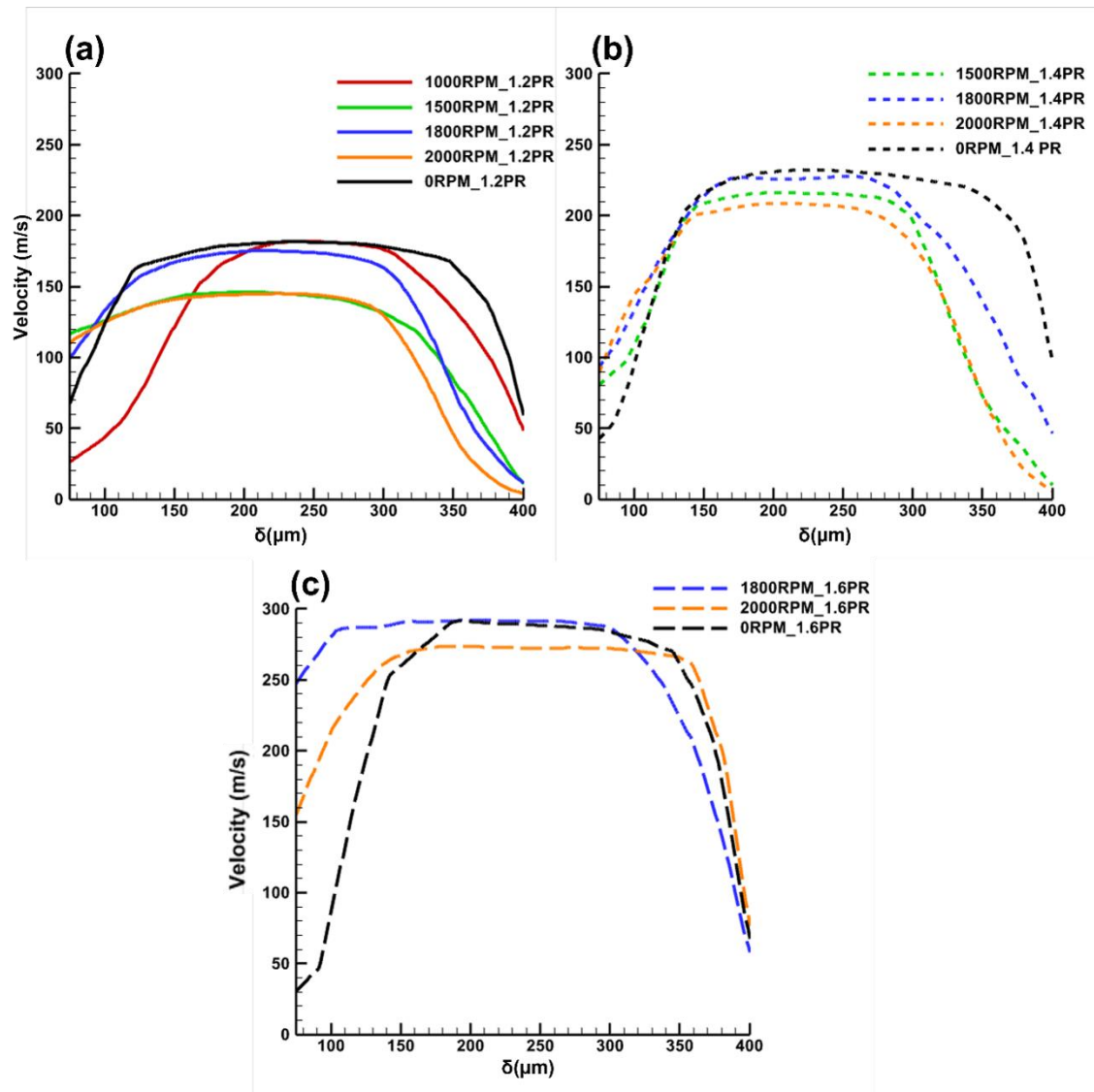


Figure 6.19 Velocity profile across the clearance from rotor tip to casing obtained by averaging 3 profiles considered above the centre of the clearance (a) at 1.2 PR (b) at 1.4 PR (c) at 1.6 PR

The volume flowrate through the clearance is calculated using measured velocity. As shown in Figure 6.20, volume flow rates derived using entire velocity profile following similar trend as the average velocity profile. However, the calculated volume flow rate ignoring boundary layer over the rotor tip is decreasing for all rotational speeds at the pressure ratio 1.6. The volume flow rate is lower in the static condition than the rotating conditions. It shows that the thickness of boundary layer has the significant effect on the mass flow rate through the clearance gap. Therefore, there is potential to reduce the leakage flow rate by developing thicker boundary layer.

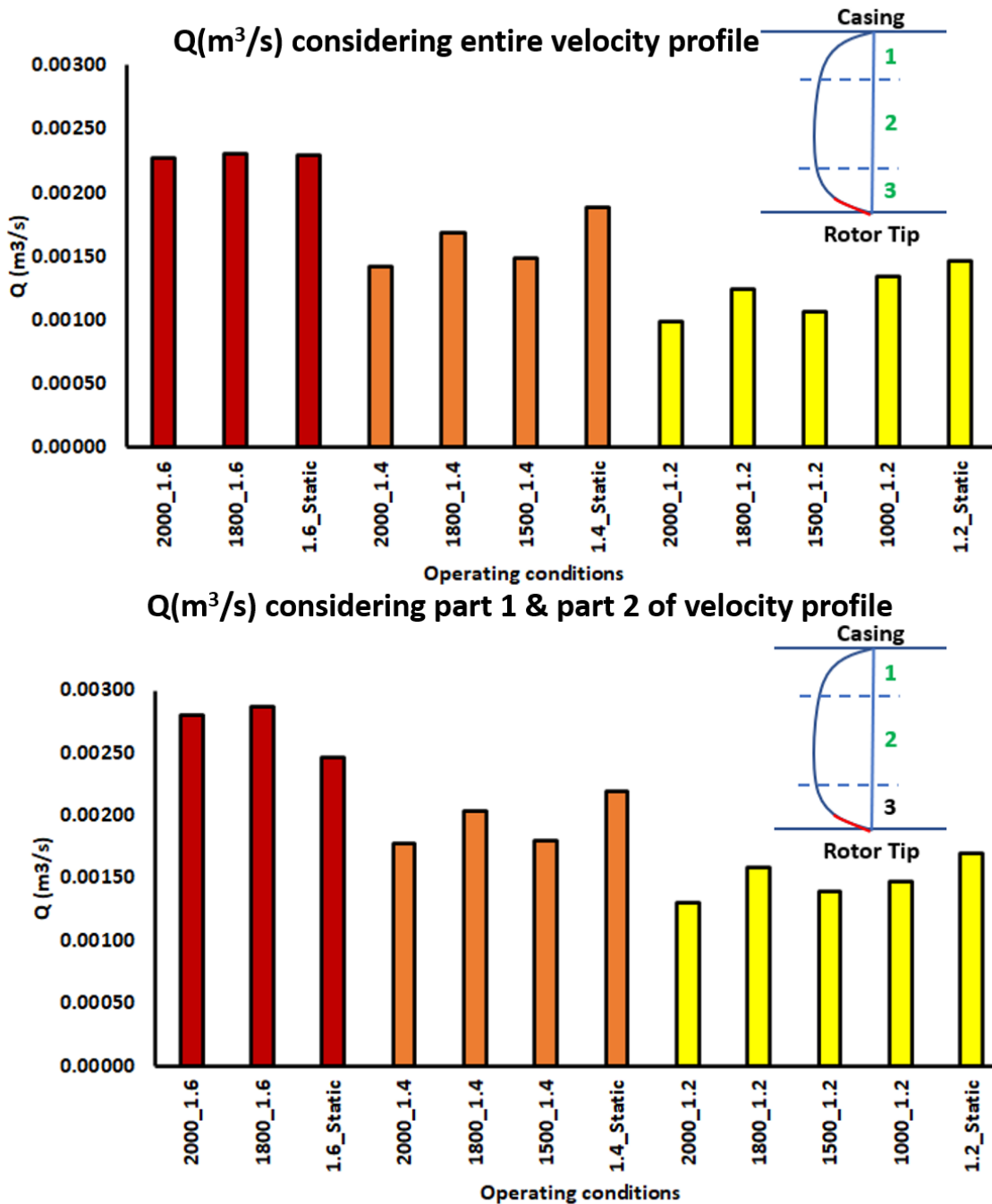


Figure 6.20 Comparison of volume flow rate calculated using the entire velocity profile and partial velocity profile

Shear gradient region observed in the static condition is thinner than in dynamic conditions, which shows that at lower pressure ratio, viscous effects are dominant while at higher pressure ratios, the pressure difference across the gap is dominant. There is no significant change in the position of the separation location. However, flow can be blocked by thick separation region.

Calculated Reynold number is between 8000 to 20000 for all operating conditions, it means flow through the clearance is turbulent. Also, the calculated Knudsen number is lower than 0.001, which indicates the continuum flow.

Flow rate through clearance gap is calculated using equation 6.3 [60] which includes the effect of clearance height, clearance depth and form factor. The observed flow, calculated with a discharge coefficient of 0.35, is found to be within $\pm 5\%$ of the measured flow in static conditions. Notably, this discharge coefficient value is lower than the typical value of 0.65 commonly observed in conventional orifice measurements.

$$\dot{m} = C_d \delta L \sqrt{\frac{\rho_1 P_1 (PR^2 - 1)}{2 \ln PR + (\xi_1 + \xi_2) + \lambda \Sigma}} \quad 6.3$$

where, \dot{m} is mass flowrate, C_d is coefficient of discharge, L is depth of gap, ρ_1 density, P_1 is pressure at upstream, PR is pressure ratio, ξ_1 and ξ_2 are factors for contraction and expansion, λ is friction factor, Σ is shape factor.

6.2.3 Results at the exit of the tip (trailing edge)

The high-speed jet which leaves the trailing edge of the tip is entering into the suction chamber. Vorticity is generally present at solid boundaries, and it may be generated within a flow wherever there is an unbalanced torque on fluid elements, such as when pressure and density gradients are misaligned. Region of high vorticity are prone to homogeneous mixing due to faster mixing by air circulation. Figure 6.21 shows the instantaneous velocity vectors at $t = t_0$, $t_0 + 0.09$ s and $t_0 + 0.18$ s, super imposed on the vorticity contour at 2000 RPM and 1.2, 1.4 & 1.6 PR. Vorticity is derived from the measured planar data. The planar data gradients in the z -direction cannot be calculated, so only rotation around the z -axis can be determined using equation 6.4,

$$\omega_z = \frac{\partial V}{\partial x} - \frac{\partial U}{\partial y} \quad 6.4$$

where, ω_z is rotation around z axis, x is direction in x axis, y is direction in y axis, V is velocity component in y direction, U is velocity component in x direction. Vorticity in a point is defined as the local rotation of the velocity field, which is calculated using equation 6.4, and Dantec Dynamic Studio software is used to calculate it from the velocity field as this software provide function to calculate vorticity directly from velocity field. In the trailing region of the tip, noticeable level of vorticity is observed along with vortex rings. This region has interesting dynamics, vortices are formed after separation at the end of the tip and travelling downstream of the tip. The pattern of shedding from the trailing edge is not simple and the high frequency fluctuation can be seen due to the

unsteady flow. It is clearly visible that the flow field is highly dynamic when the flow exits from the trailing edge of the tip. Here, two air layers lying close to the each other and moving in opposite direction with different speed which creates vortex and this phenomenon are similar to Kelvin-Helmholtz instability [61]. Vorticity contours in Figure 6.21 indicate that the vorticity is getting stronger with the increase in pressure ratio, also vortex size is evolving and getting bigger as it moves away from the tip edge, which indicates the rolling up process of the vortex rings. Vortices are responsible for mixing between the leaked gas and the gas that is already existing in the chamber. However, it is depicted in the Figure 6.22, vortex in the stationary condition of the rotor at the same pressure ratios are absent, which shows that rotation of the rotor has influence on vortex generation. During running conditions of the machine, rotor drags the fluid along with its surface which interacts with the high velocity leakage coming out at trailing edge of the tip and create highly dynamic vortex field.

Swirl strength is also derived from the velocity vector field to evaluate the behaviour of flow in vortices, as presented in Figure 6.23. Interesting nature of successive negative and positive swirl strength is observed. Intensity of swirl strength is getting decreased as flow moves away from the trailing edge during running conditions while intensity remains strong even far from the trailing edge in static conditions. The sharp long strip of swirl strength contour is observed in static conditions. Also swirl strength seems to be increasing with pressure ratio.

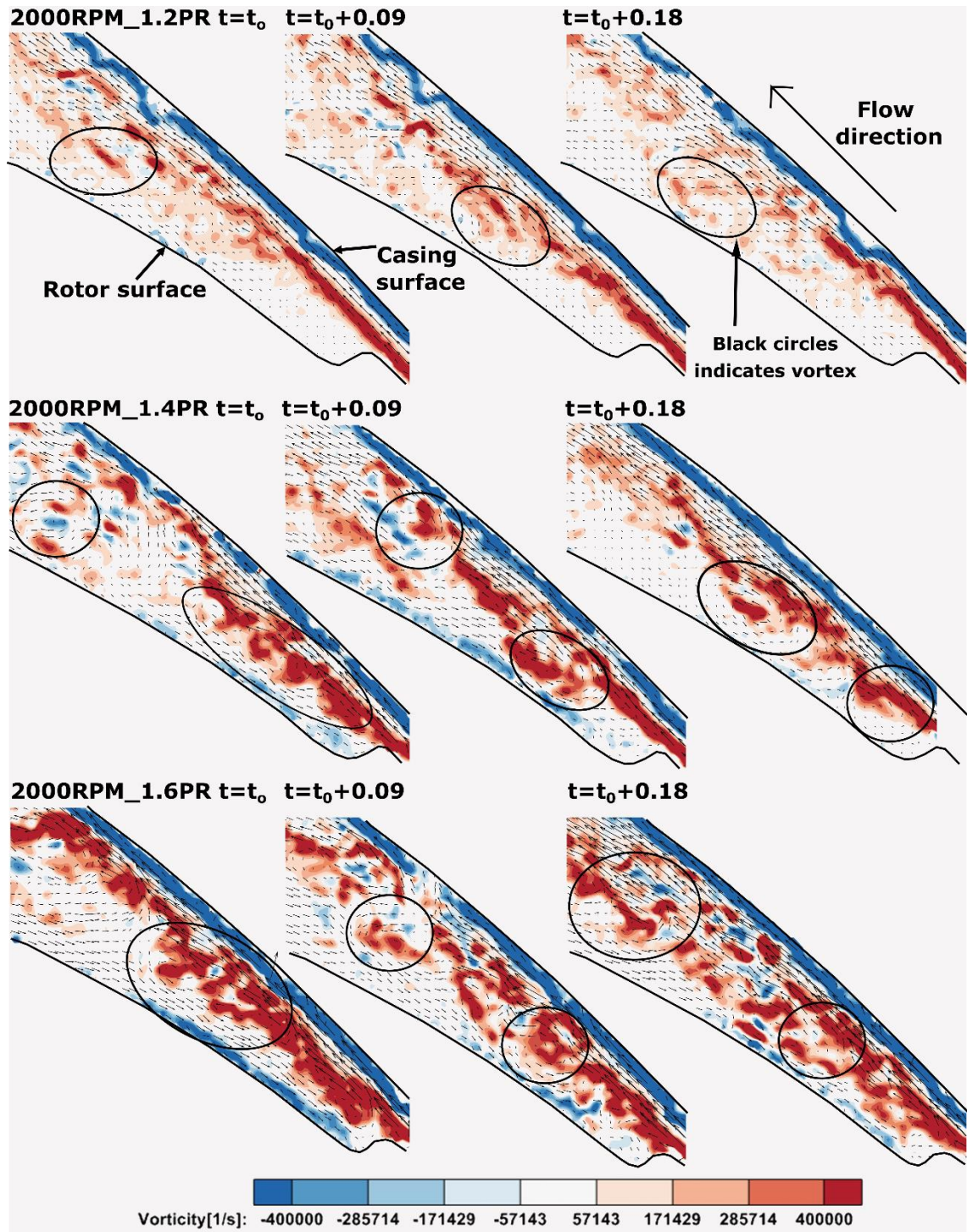


Figure 6.21 Instantaneous vorticity contours: $t = t_0, t_0+0.09$ s, t_0+18 s at 2000 RPM and 1.2, 1.4 & 1.6 PR super imposed with velocity vectors

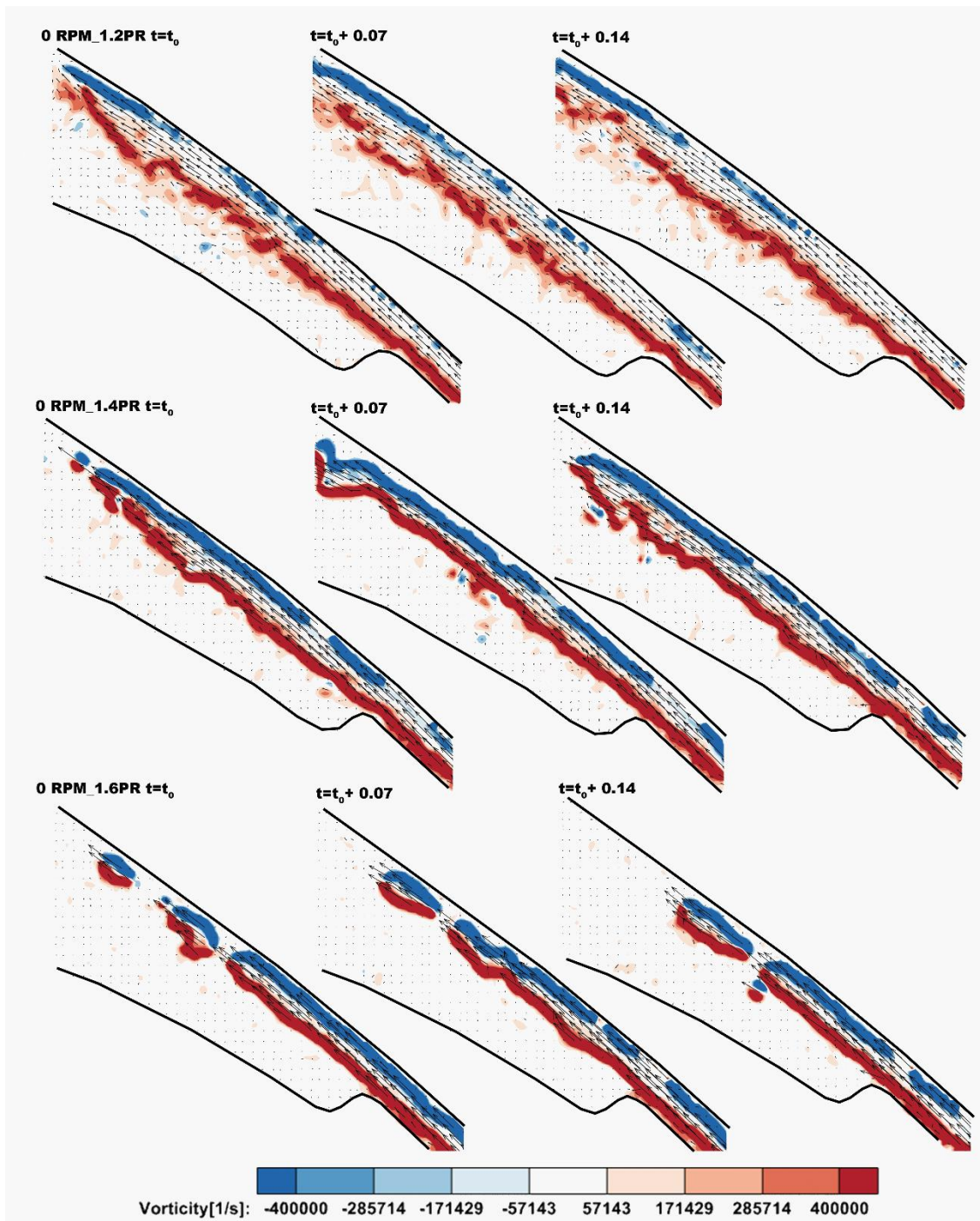


Figure 6.22 Instantaneous vorticity contours: $t = t_0$, $t_0+0.07$ s, $t_0+0.14$ s at 0 RPM and 1.2, 1.4 & 1.6 PR super imposed with velocity vectors

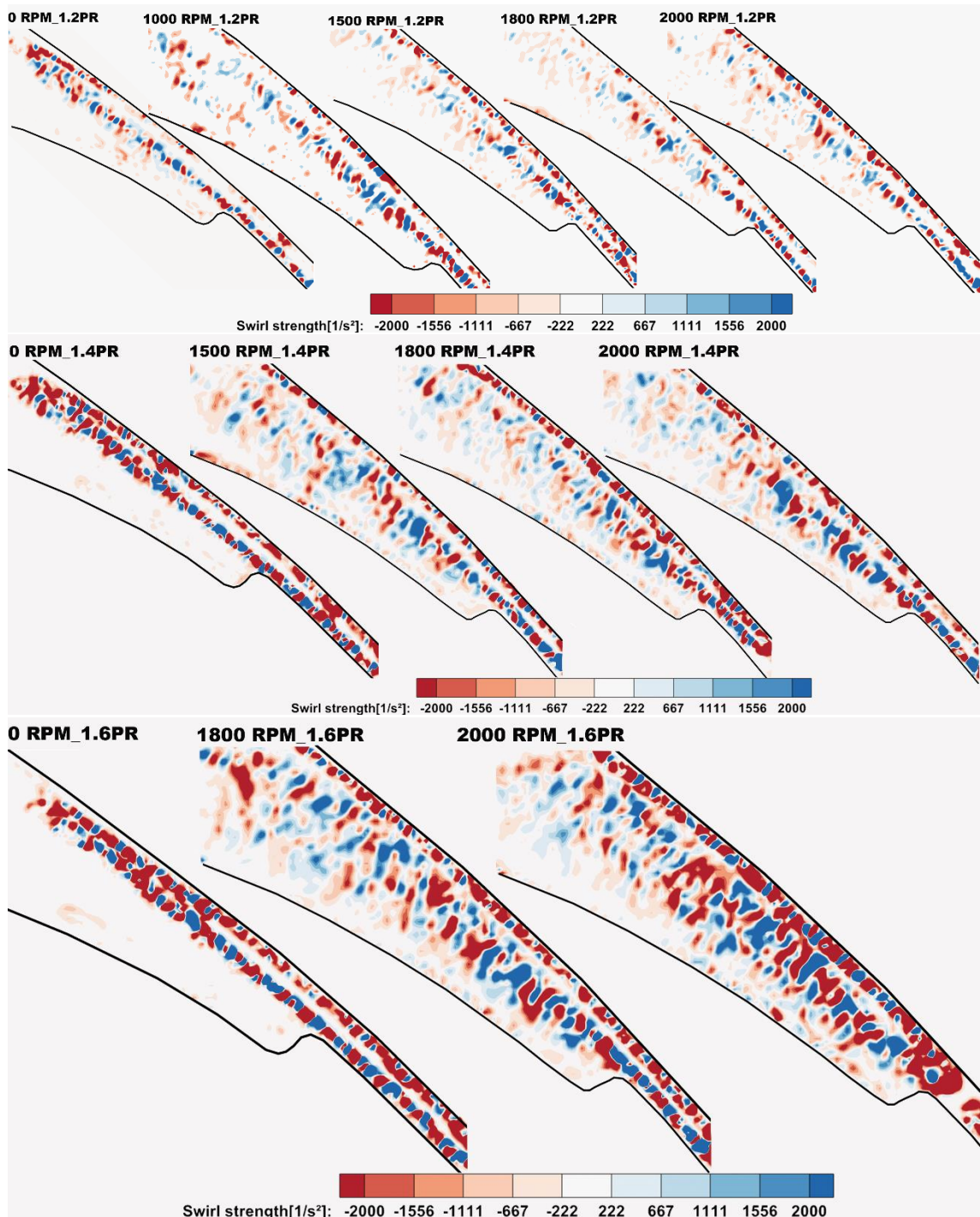


Figure 6.23 Swirl strength at all measured conditions at trailing edge of the tip (contours are derived from the average of 10 instantaneous plots)

Strength of vortex generated at the exit of the tip shows how strong or weak the leakage flow is. Also, the vortex inside the leakage gap is beneficial while the one at the exit is not because the recirculation zone can obstruct the leakage flow.

6.2.4 Results at the entrance of the tip (Leading edge)

Velocity measurement is also carried out for the flow field at the entrance of the tip. Shear in the fluid flow can be derived from velocity gradient, and it is directly proportional to

the velocity gradient. To provide further insights into the flow structures, the velocity gradient in the x-y plane is calculated using equation 6.5. The derivative in the z-direction cannot be calculated for the planar data obtained by measurements and therefore it is neglected.

$$\tau_z = \frac{\partial V}{\partial x} + \frac{\partial U}{\partial y} \quad 6.5$$

where, τ_z is a total shear in x-y plane. Figure 6.24 shows the result for the total shear contour derived from the velocity vector field. From the 2D measured data from the PIV, total shear is obtained using Dynamic Studio software, which uses equation 6.5 to calculate velocity gradient in the measured plane. It is observed that regions of high shear gradient are concentrated around the surface of the lobe. Shear grows as moves further towards leading edge of the tip; thick shear layer is depicted at the base of the tip. While on the casing surface negative shear is observed in all cases. These positive extreme values show the flow attaches to the rotor surface more than the casing surface.

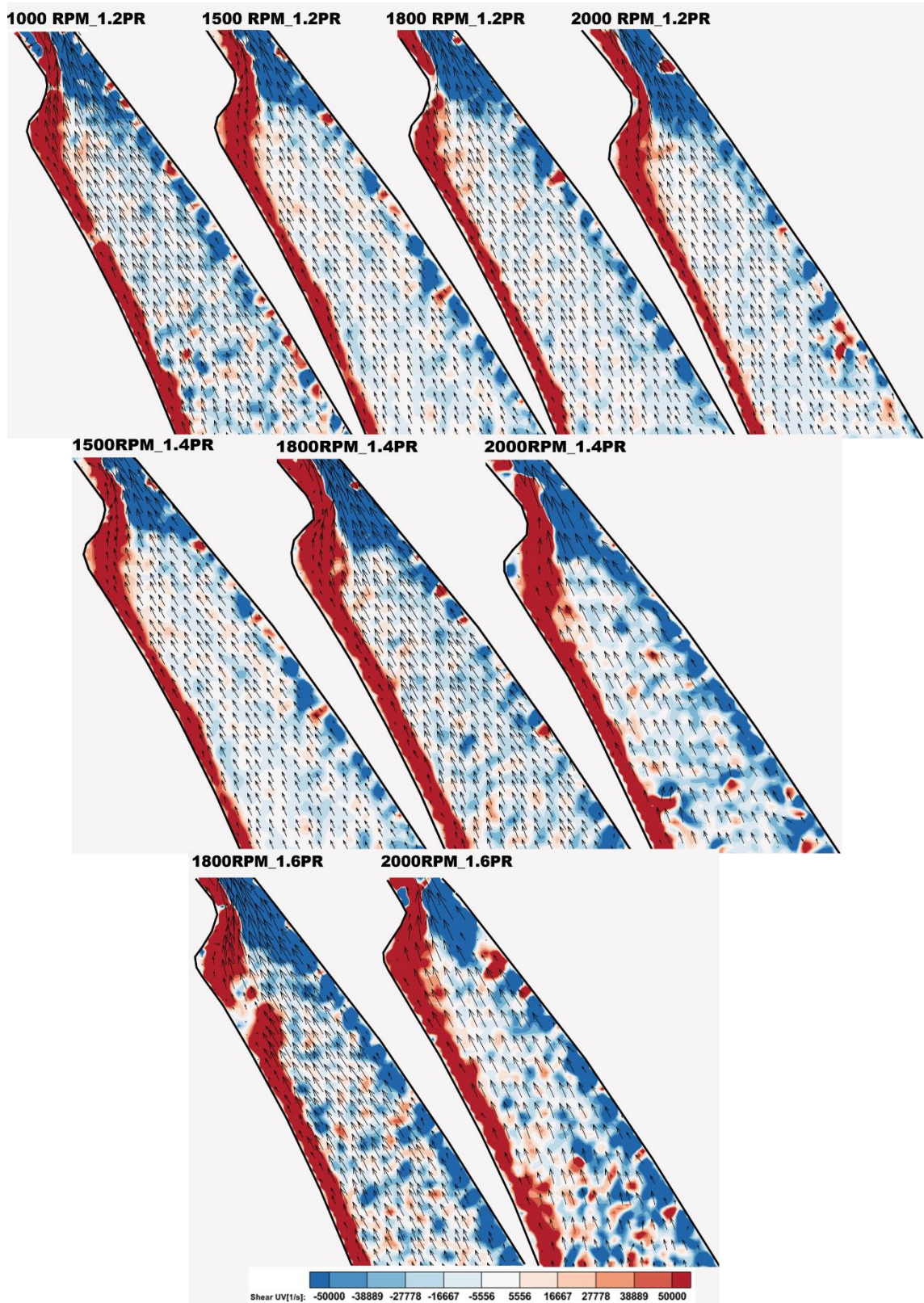


Figure 6.24 Contour of velocity gradient for all the operating conditions over the average flow field of 10 instantaneous vector field superimposed with velocity vectors

6.3 Uncertainty in PIV measurements

Errors in PIV measurements may be introduced due to the specific flow facility used, setup of the experimental apparatus and choices of the data evaluation methods. Wieneke [62] stated that, while all error sources are included in the recorded images, some of them remain ‘hidden’ and their uncertainty cannot be quantified. It should be noted that, whenever possible, the experimenter should design and conduct the experiment in such a way that measurement errors are avoided or minimized. Since not all errors can be avoided or reduced, the experimenter should use post processing of recorded images to quantify the uncertainty associated with the most relevant remaining error sources. Errors due to system installation and alignment can occur if the measurement plane is not properly aligned with the desired flow direction, in current setup proper care is taken to align laser illuminated measurement plane with camera. Error can also be introduced by improper timing and synchronization between camera and laser pulses. In this study, in the beginning of experiments it is checked and confirmed that laser pulses and camera frames are well synchronized. Peak locking is also the error that one should consider during the PIV measurement. It occurs mainly when the particle image is small compared to the pixel size (particle image diameter not exceeding one pixel) and has the effect of biasing the measured particle image displacement towards the closest integer pixel value. As a result, the measured velocity may be overestimated or underestimated depending on the sub-pixel length of the particle image displacement. For each measurement, peak locking effect is checked to ensure that measurements are good.

To quantify the uncertainty in measurement, direct method known as particle disparity is employed, which extract the measurement uncertainty directly from the image plane. In the particle disparity [63], the standard uncertainty of the measured particle image displacement is quantified considering the contribution of individual particle images to the cross-correlation peak. The basic idea is that, in case of perfect match among particle images of an image pair, the cross-correlation function features a sharp correlation peak, whose width is proportional to the particle image diameter; in this case, the measurement uncertainty is the minimum. Conversely, when the particle images do not match perfectly, a residual positional disparity is present, which has the effect of broadening the cross-correlation peak and in turn yield higher uncertainty of the measured displacement. The approach matches the particle images of two corresponding interrogation windows at the best of the velocity estimator and computes a positional disparity between matched particles. The method provides the (standard) uncertainty of each velocity component

without requiring any assumption on the flow and imaging conditions. However, it relies upon the identification and location of individual tracer particle images.

Uncertainty for each measurement is derived using particle disparity method. Uncertainty is presented directly in terms of velocity values instead of pixel values for better understanding. It is observed for all the measured conditions that uncertainty ranges from 0 to 7 m/s for entire flow field. Figure 6.25 shows the scaler map of uncertainty at 1000 RPM and 1.2 PR. It is important to note that maximum average uncertainty value over the velocity profile across the clearance gap is 3.4 m/s. Uncertainty over the flow field at the exit of the clearance (Figure 6.26) ranges from 0 to 10 m/s while at the entrance of the clearance (Figure 6.27) it ranges from 0 to 7 m/s. The validity of the comparisons made in the previous section remains intact, considering the associated uncertainties in the measurements.

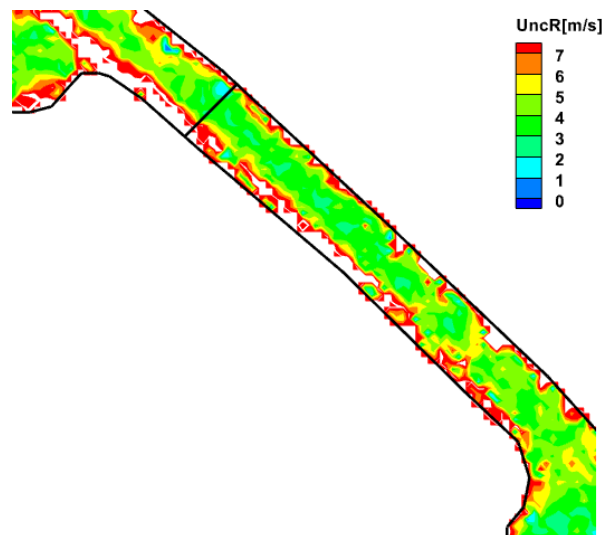


Figure 6.25 Scaler map of uncertainty inside the clearance at 1000RPM and 1.2 PR

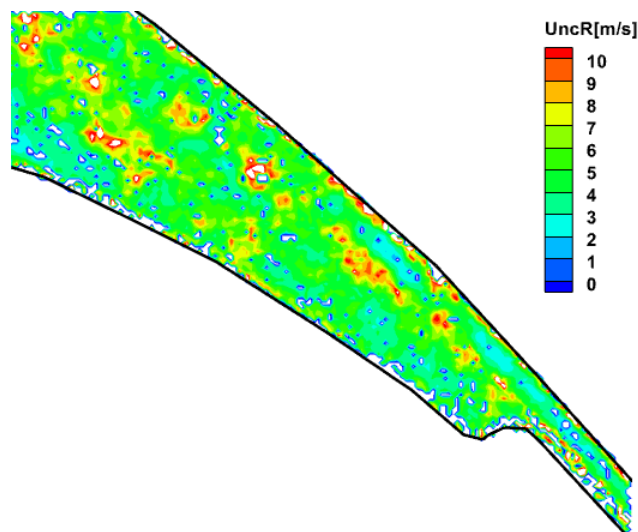


Figure 6.26 Scaler map of uncertainty at the exit of the clearance at 1000RPM and 1.2 PR

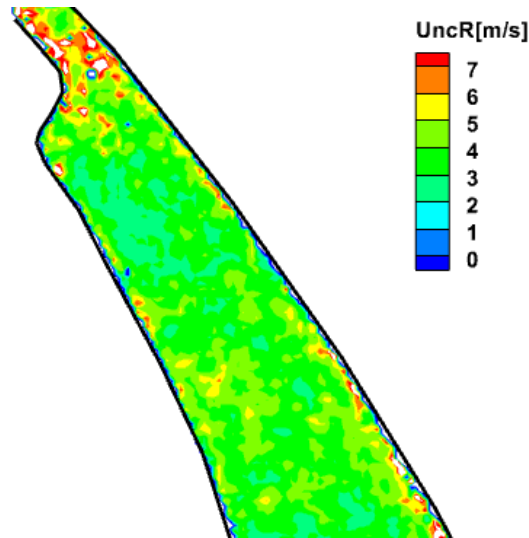


Figure 6.27 Scaler map of uncertainty at the entrance of the clearance at 1000RPM and 1.2 PR

6.4 Summary

This chapter describes the experimental study of Particle Image Velocimetry (PIV). The chapter starts with a detailed explanation of the PIV experimental setup and procedures, which includes the DAQ system, functional devices and seeding particles, PIV setup, and PIV measurements. The chapter further explains the data processing techniques used for PIV measurements. The main focus of this chapter is on PIV measurements and results, which include measurements of the flow field in the clearance gap between the tip and casing, results at the clearance between the tip and casing, results at the exit of the tip (trailing edge), and results at the entrance of the tip (Leading edge). Finally, the chapter concludes with PIV uncertainty quantification. Next chapter discuss the results analysis in detail.

Chapter - 7 Combined result analysis and CHT comparison

This chapter discusses behaviour of the flow field inside and around the clearance gap using streamlines, vorticity and turbulence intensity. This is enabled by a good spatial accuracy of the PIV measurements. Measured temperature field over the lobe surface and conjugate heat transfer analysis is also presented.

7.1 Flow field inside the clearance between tip and casing

The primary aim of this part of the study is to measure the flow field inside the clearance gap in order to find aspects which could reduce leakage flows. The plane shown in Figure 6.8 is in the middle of the rotor tip and is assumed to be a symmetry plane of the leakage flow.

Data are obtained at the operating conditions as listed in Table 6.3. The mean velocity field obtained along the measurement plane at 2000 RPM and 1.6 pressure ratio is presented with a streamline in Figure 7.1. The stream traces for all other conditions have similar behaviour.

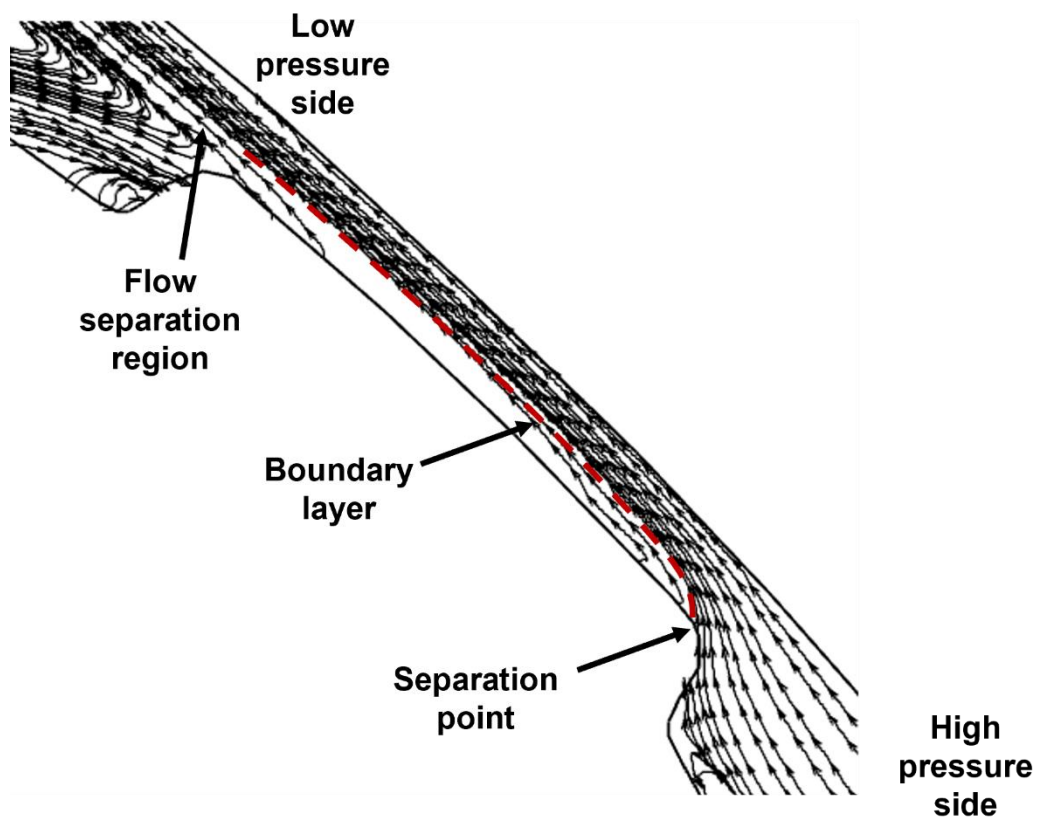


Figure 7.1 Visualization of the mean velocity field inside the clearance at 2000 RPM and 1.6 PR

The flow which enters from the high-pressure side experiences a strong deviation because of the restriction of the tip step, which causes separation at the edge of the tip and leads to generation of a boundary layer over the tip. This boundary layer exists over the entire span of the tip and when it exits from the tip it again causes separation of the flow, which leads to creating vortices at the exit of the tip. These flow structures are known features from the widely studied flows, such as flow over the square obstacle and flow over the step [64], [65], but they were never exactly measured in the particular flow conditions of a positive displacement machine.

The magnitude of mean velocity component in the measured plane are reported in Figure 6.15, Figure 6.16 and Figure 6.17. From the velocity magnitudes, a strong acceleration of the flow in the region above the edge of the tip at the entrance on high pressure side is observed. The tip step imposes blockage to the flow. Since the flow is compressible, velocity magnitude close to sound velocity is observed. After entering the clearance passage, gas velocities increase to the maximum value. To compare velocities between the operating conditions, velocity is extracted along the line A (Figure 6.15), which start from higher pressure region and end in the lower pressure region. The location of Line A and Line B is shown in Figure 6.15. Velocity along the line A is plotted in Figure 7.2, Figure 7.3 and, Figure 7.4. It is observed that the rate of increase in the average velocities along the line “A” are different for different speeds at pressure ratio of 1.2 while they are almost the same at higher pressure ratio of 1.6. It means that the speed of the rotor has higher effects on the velocity at the entrance of the clearance at low pressure ratios that at higher pressure ratios. Once the velocity field is developed it remains almost constant until the gas reaches to the exit of the clearance gap. However, it is observed that measured velocity values at the exit of the gap are different for different speeds at the same pressure ratio. Flow exits from the clearance at a very high velocity, interacts with the fluid in the low-pressure domain along the rotor surface and starts to create vortices at the exit of the tip.

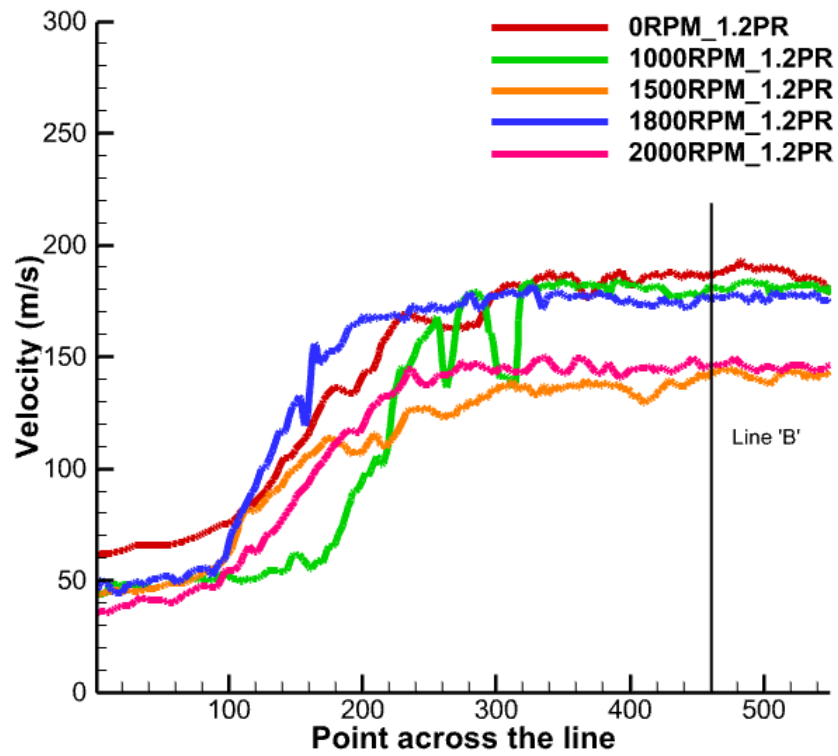


Figure 7.2 Velocity over the line 'A' across the clearance at 1.2 PR and various speed

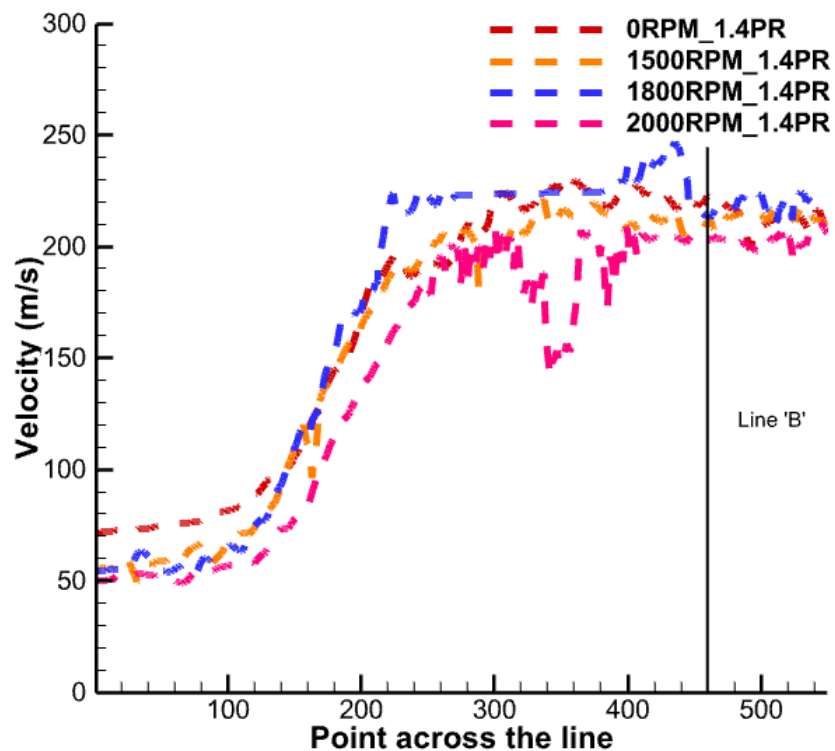


Figure 7.3 Velocity over the line 'A' across the clearance at 1.4 PR and various speed

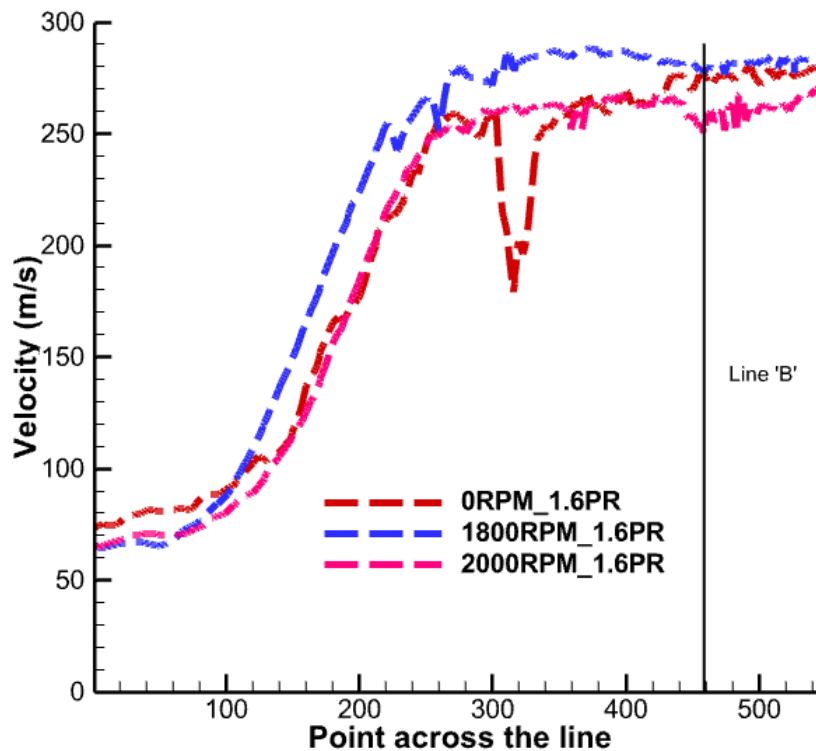


Figure 7.4 Velocity over the line ‘A’ across the clearance at 1.6 PR and various speed

7.2 Flow field at the exit of the clearance

Measurements of the flow field at the exit of the tip, shows several flow structures. Figure 7.5 shows the velocity vector field, streamlines and vorticity contour for the flow coming out from the clearance at 2000 RPM and 1.6 PR. From the vector field it is observed that the flow coming out from the clearance as a jet at higher velocity. These vortices are clearly identified using the streamlines of this flow. As a vortex moves away from the exist end of the tip, it grows in size. Computed vorticity shows high intensity where the flow exits from the tip and its magnitude is decreasing as it moves away from the tip end. Similar structure is observed for the measurement at all other operating conditions. To be able to compare the strength of the secondary flow, profiles of the mean vorticity are extracted along the line ‘C’ (Figure 7.5) for all operating condition. The location and shape the Line ‘C’ is chosen in such a way that it follows the path of large vorticity change, which starts from the top of the trailing edge of the tip and spreads in between the casing and lobe surface. The comparison is given in Figure 7.6. It is observed that vorticity is higher at the exit of the clearance, and it is decreasing as the gas moves away from the tip edge. Also, there is an influence of pressure ratio on the vorticity, if pressure

ratio is higher vorticity at the exit of the tip is higher but for all the conditions vorticity dropped down to the same level as flow moves away from the tip.

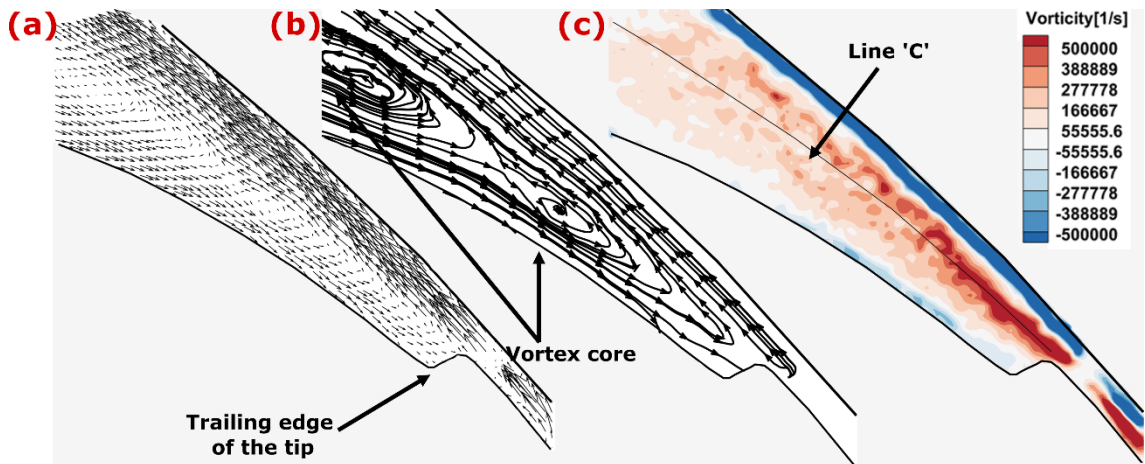


Figure 7.5 (a) velocity vector (b) streamlines (c) vorticity contour for 2000RPM and 1.6 PR

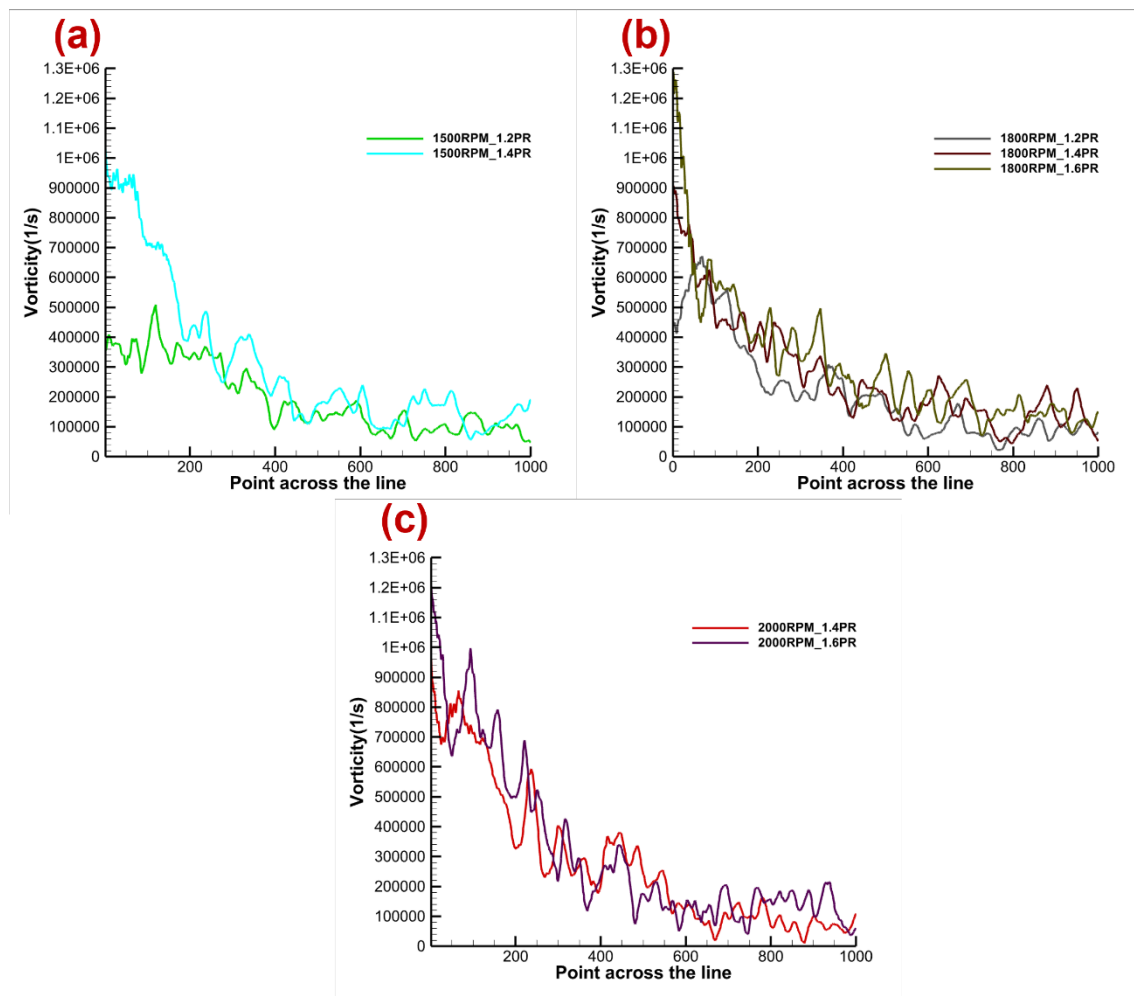


Figure 7.6 Vorticity at all the measured condition

Higher turbulence is observed in the region at the exit of the tip due to separation of flow. Highest values of turbulence are observed at higher pressure ratios. This can be observed

in Figure 7.7 , Figure 7.8 and Figure 7.9. However, the turbulence intensity at the exit of the clearance gap is highest for the static condition. The high turbulence level is not concentrated in the same axis of the flow stream as for static conditions when the rotors rotate. At the same pressure ratio, during running condition of the machine, turbulence intensity in the vicinity at exit from the tip increases with the increase in speed.

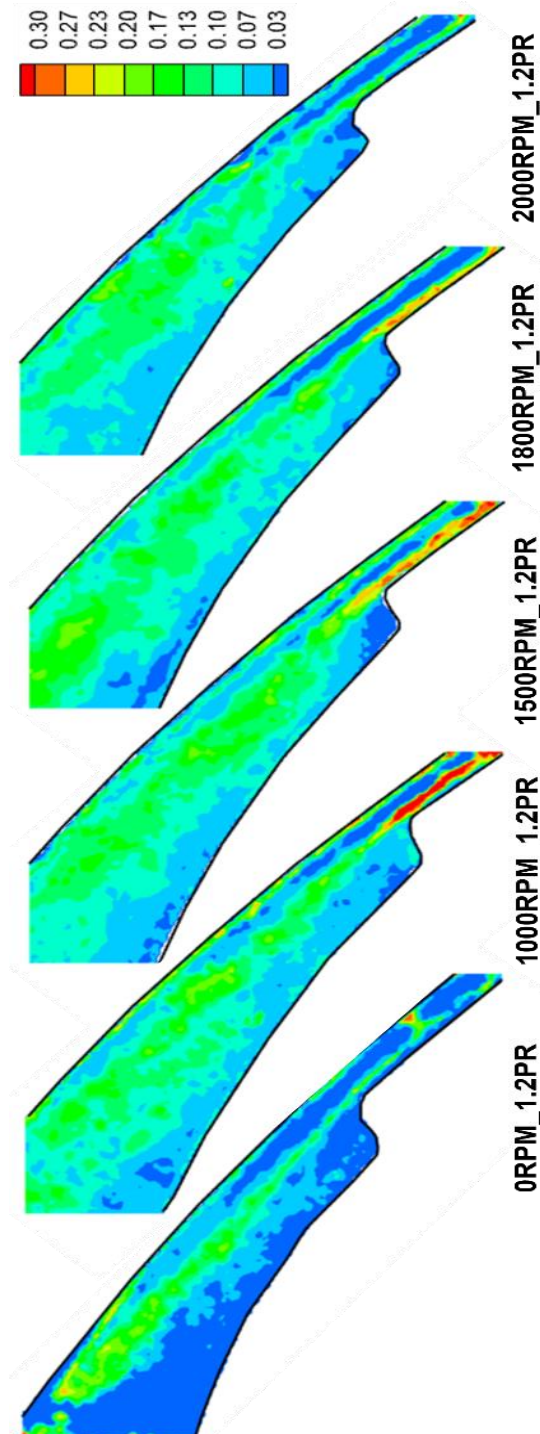


Figure 7.7 Turbulence intensity at 1.2 PR and various speed

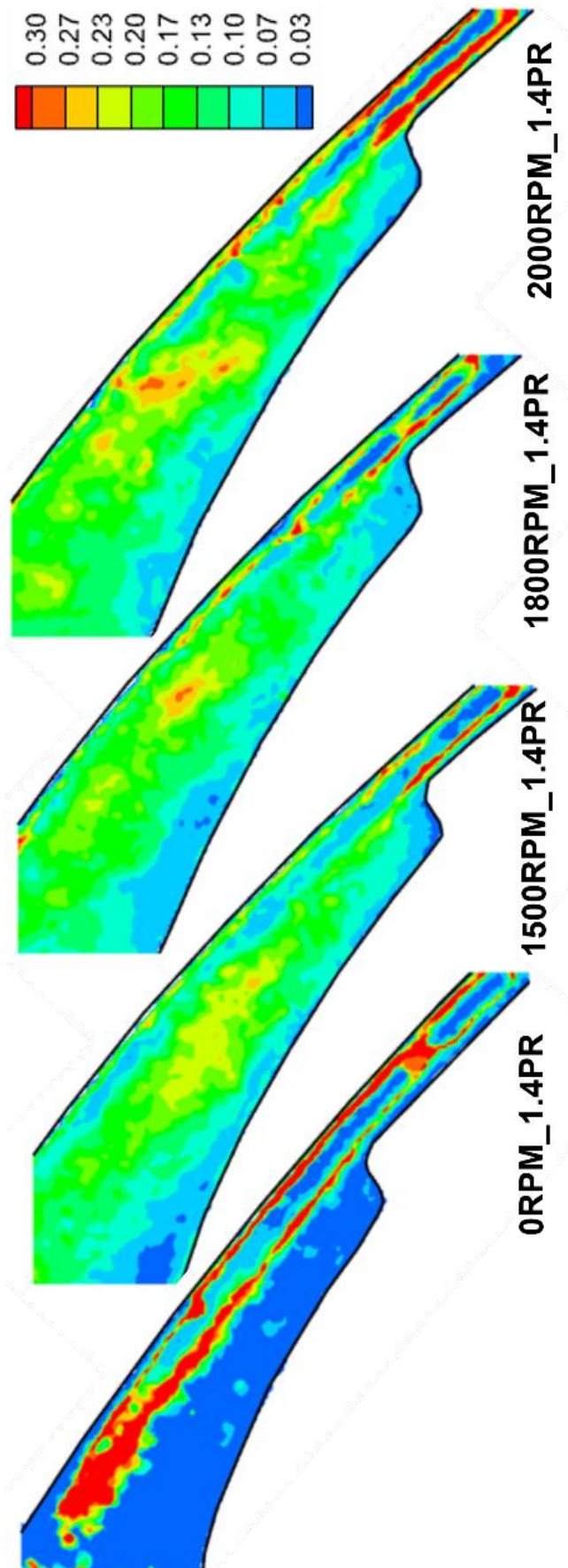


Figure 7.8 Turbulence intensity at 1.4 PR and various speed

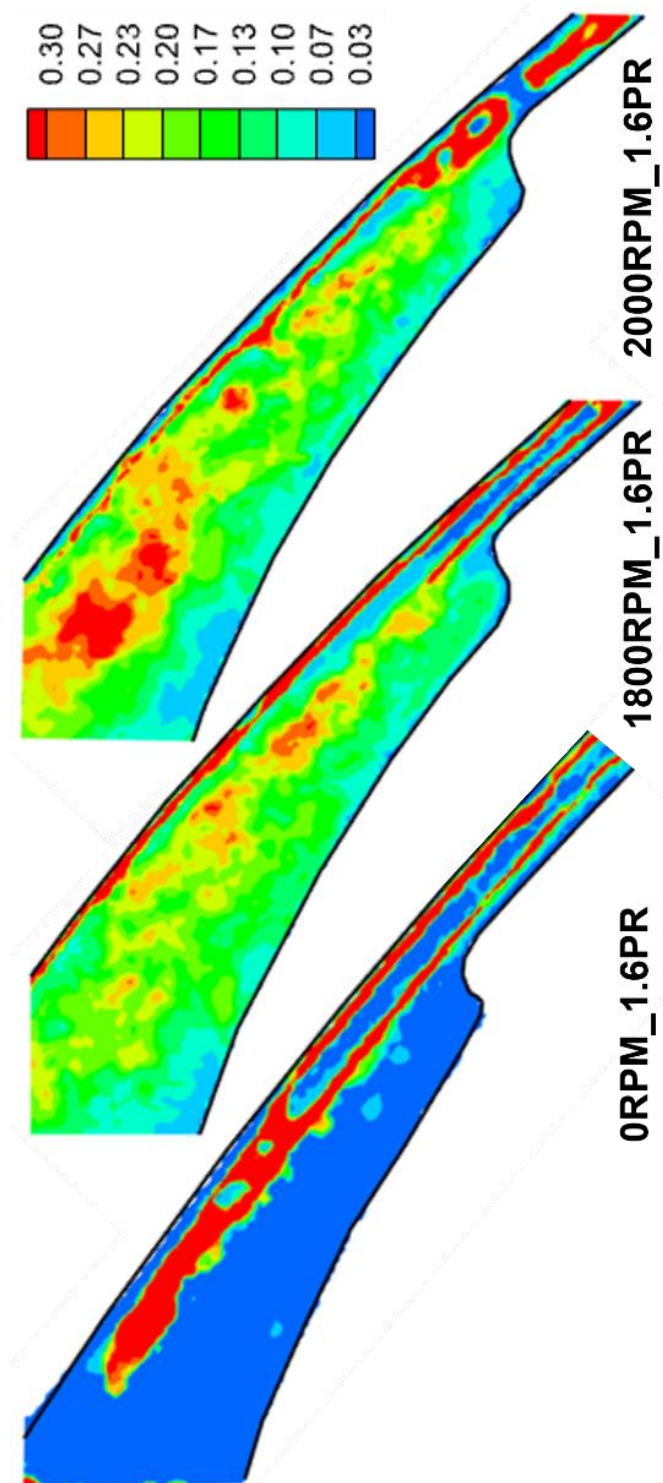


Figure 7.9 Turbulence intensity at 1.6 PR and various speed

Results show strong anisotropic character of turbulence. At lower pressure ratio, the turbulent flow occupies smaller region at the exit of the tip while the size of this region is increasing with pressure ratio.

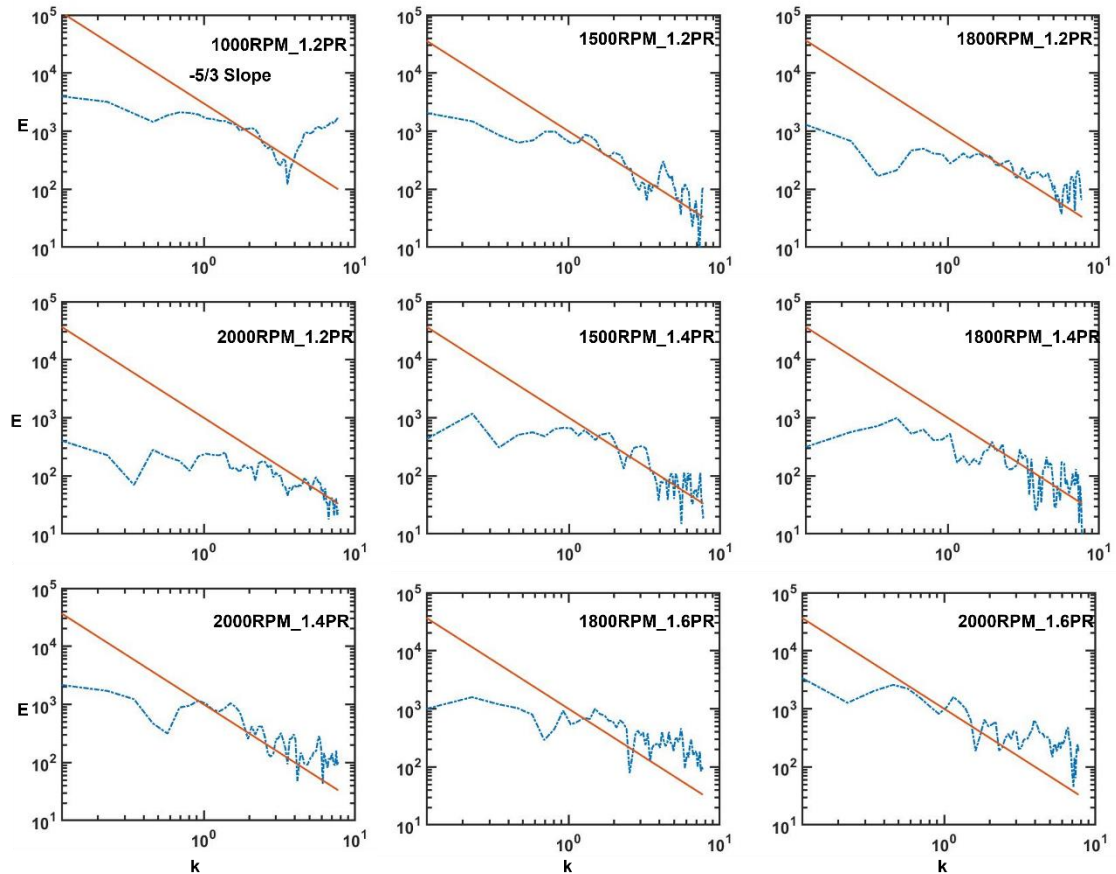


Figure 7.10 Energy spectrum Log-Log curve for all measured conditions

This compressible wall bounded flow follows Kolmogorov's $-5/3$ slope reasonably well (orange line in the plots of energy spectrum(E) vs wavenumber(k)). It shows that vortex shedding, and occurrence of intermittent fluctuations are captured well in measurements. In addition, it shows the energy cascade in the measured flow.

7.3 Flow field at the entrance of the tip

Velocity vector field, streamline and vorticity contour from the measurements at the entrance to the tip are shown in Figure 7.11. Velocity is increasing as the flow moves towards the leading edge of the tip because the flow area is getting drastically reduced. Streamlines show the flow path in this region. The vorticity field in this region shows behaviour similar to a vorticity map found in the flow through a tube; Vorticity is positive on the lobe surface) and it is negative on the casing surface.

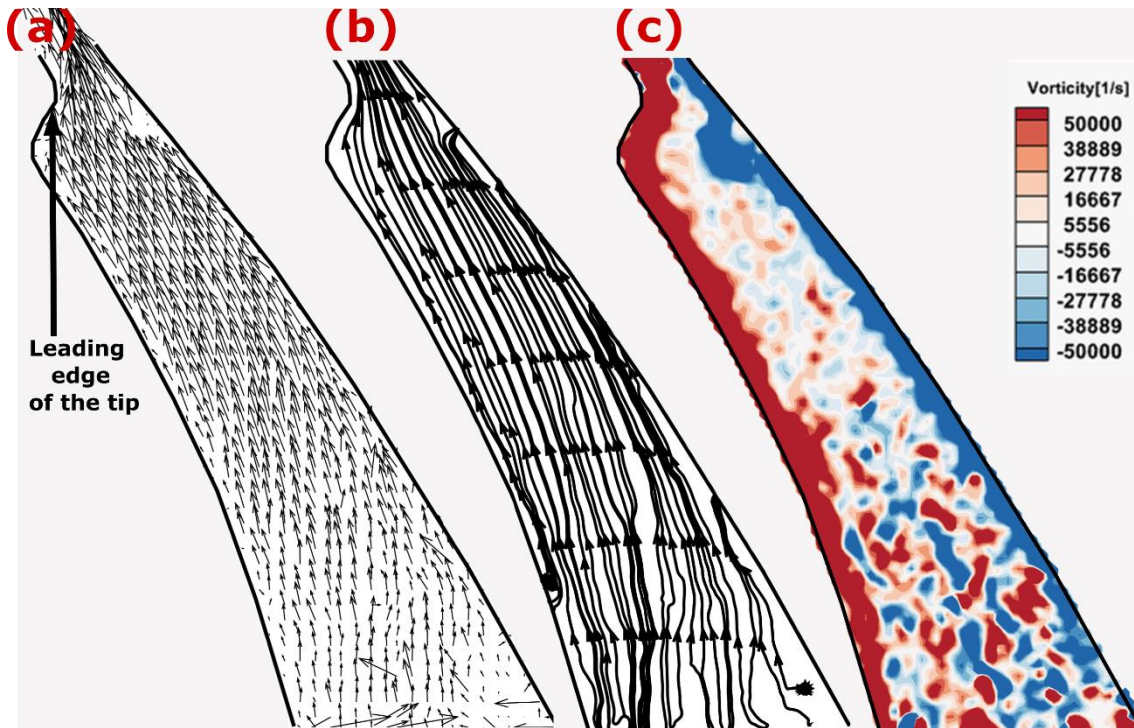


Figure 7.11 (a) Velocity vectors (b) Streamlines (c) Vorticity contour at 2000RPM and 1.6 PR

Magnitudes of the turbulence intensity are presented in Figure 7.12 to Figure 7.14. The turbulence intensity is higher at lower speed and is reduced with the increase in speed. Also, it is dependent upon the pressure ratio, it is increasing with the increase of the pressure ratio.

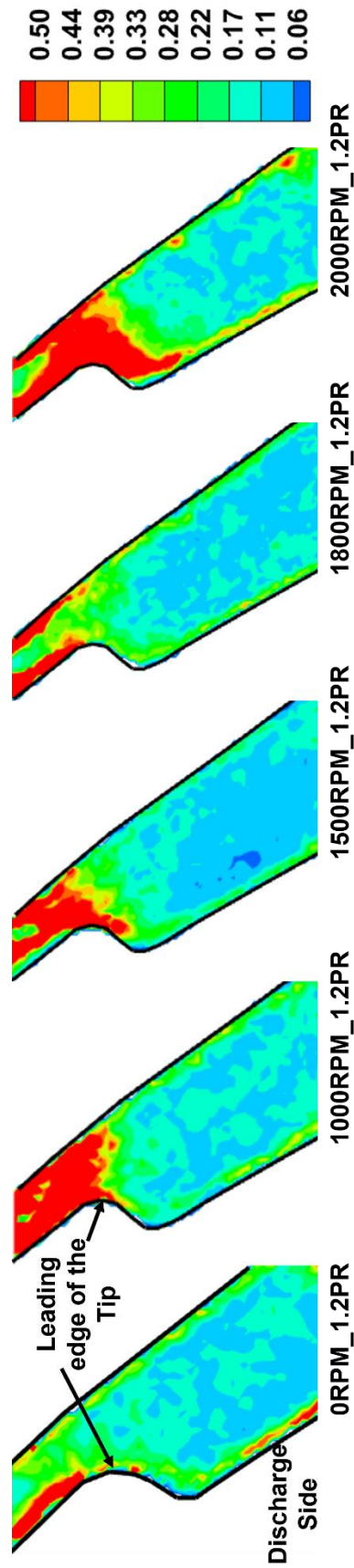


Figure 7.12 Turbulence intensity at 1.2 PR

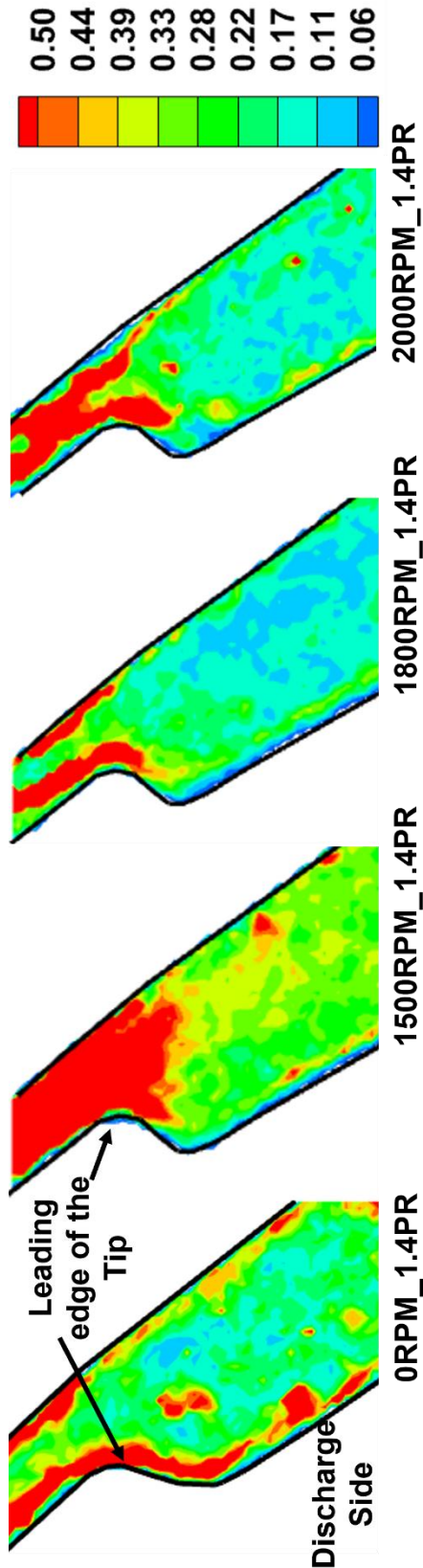


Figure 7.13 Turbulence intensity at 1.4 PR

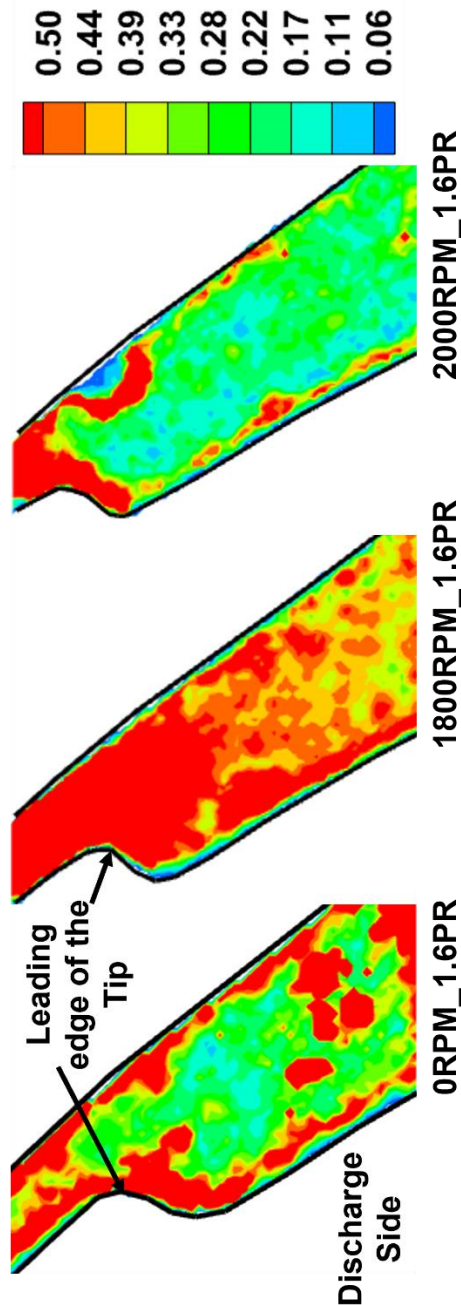


Figure 7.14 Turbulence intensity at 1.6PR

7.4 Temperature and flow field over the Tip

The link between the flow field inside the clearance gap and the lobe surface temperature field is of interest in this part of the study. Streamlines of the flow field and the temperature map at the same measured plane are presented in Figure 7.15. The surface temperature on the high-pressure side is higher than at the low-pressure side and reduces gradually over the surface of the length of the tip. Temperature across the surface of the rotor is plotted in Figure 7.16, Figure 7.17 and Figure 7.18. The line L1 along which the temperature is extracted is shown in Figure 7.16. The temperature along the rotor tip

surface is reducing with the increase in speed at a constant pressure ratio. One potential reason is decrease in the leakage losses at higher speed, which is supported by measured velocity in clearances. However, the nature of temperature distribution along the line L1 which passes across the tip is observed to be same at constant pressure ratio for various speeds.

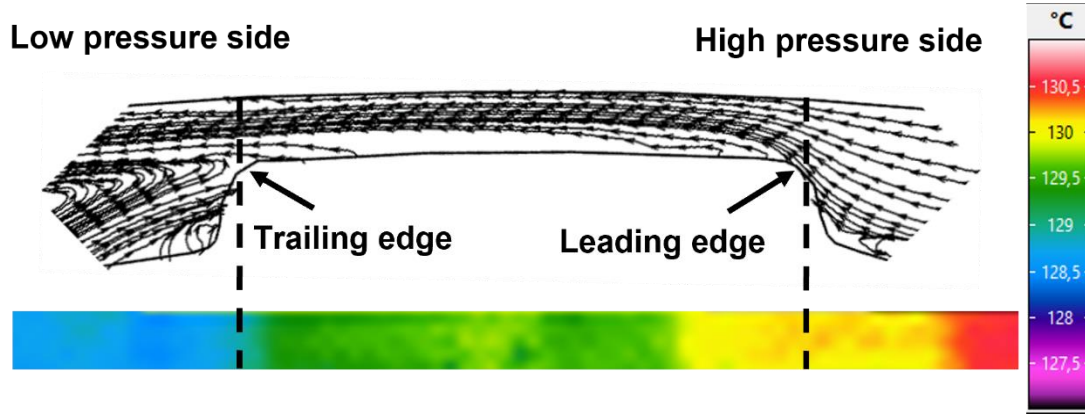


Figure 7.15 Streamlines of flow field and measured surface temperature map of lobe in same plane at 2000 RPM and 1.6PR

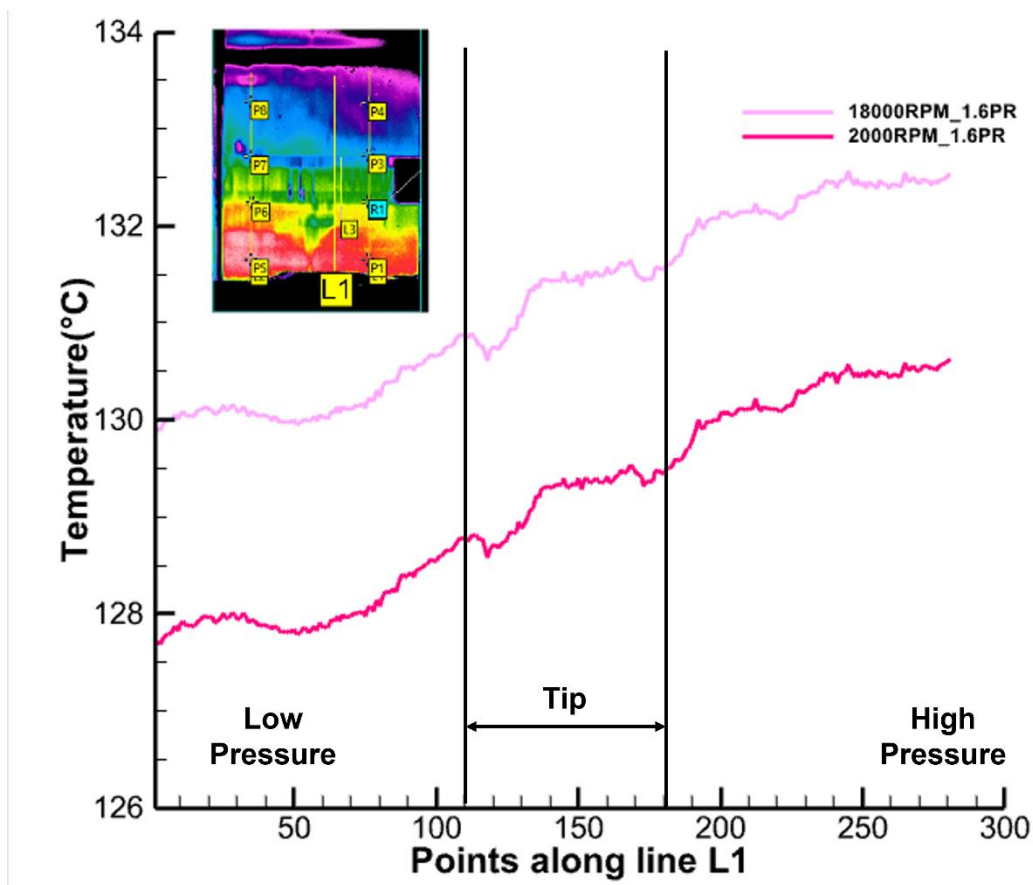


Figure 7.16 Temperature along line L1 at 1.6PR and various speeds

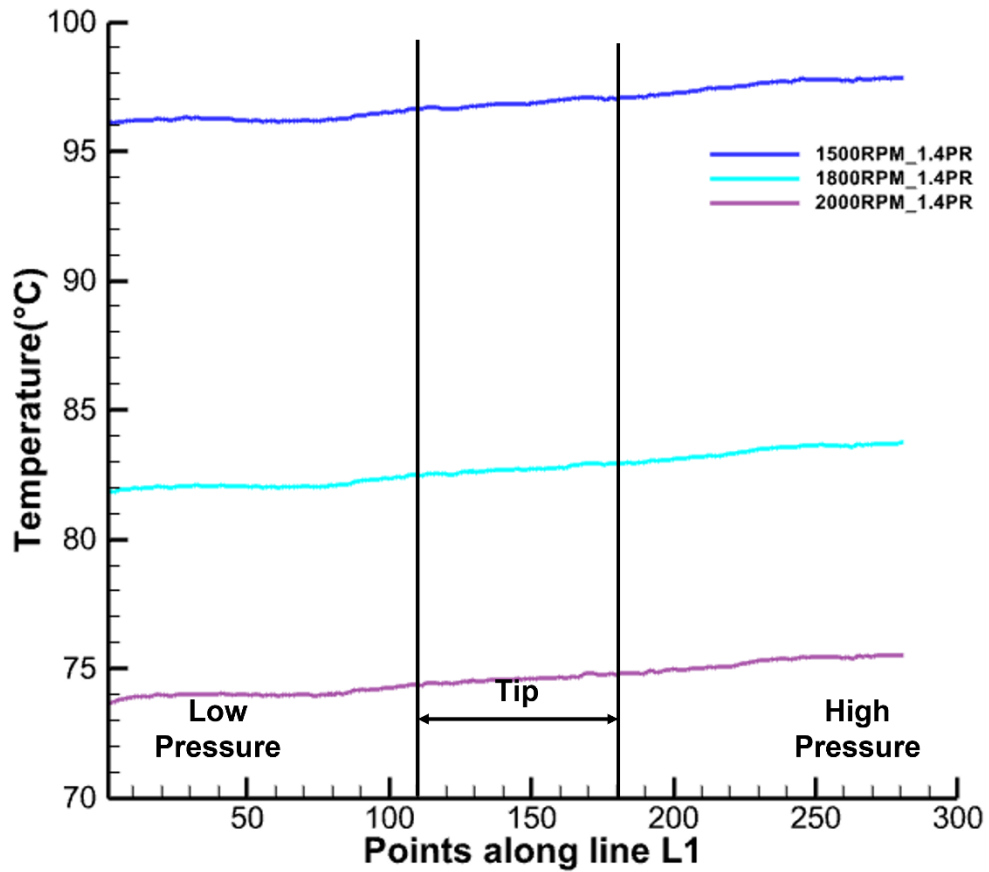


Figure 7.17 Temperature along line L1 at 1.4 PR and various speeds

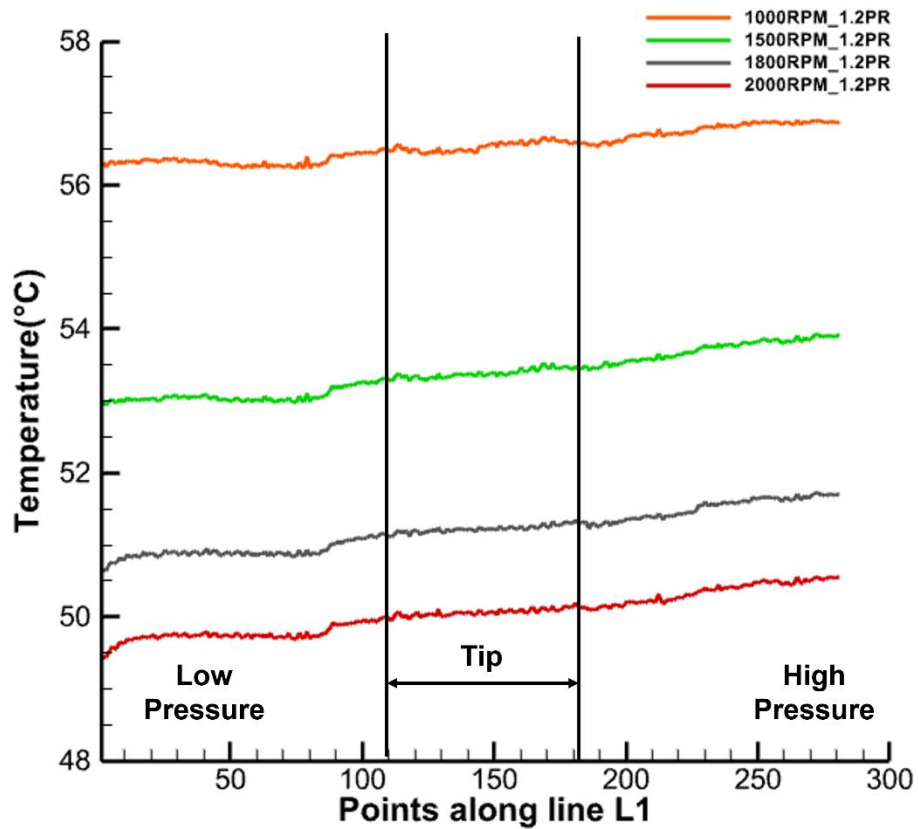


Figure 7.18 Temperature along line L1 at 1.2 PR and various speeds

Conjugate Heat Transfer based CFD model has been developed and used to analyse heat transfer from hot pressurized air to rotors, casing and surrounding components for a Roots blower application [66]. The surface temperatures calculated using this new model are also in good agreement with the experimental data sets. This work is presented in Appendix A, because the work related to numerical simulation was carried out by author's colleagues.

7.5 Conjugate heat transfer analysis results

In this section, IR thermography experimental data are compared with the simulation results. Methodology used for numerical model is described in the Appendix A. In total, five different operating conditions were simulated, and the results are validated using the available experimental data obtained using high speed infrared thermography. The imposed convective boundary conditions on outer walls have the same parameters h' and T_{∞} where, h' is the heat transfer coefficient and T_{∞} is the free stream temperature of air surrounding the blower. The heat transfer coefficient value of $10 \text{ W}/(\text{m}^2\text{K})$ was assigned to the outer walls of the blower, as found for turbulent isoflux plates (Equation 7.1)The surrounding air temperature is $25 \text{ }^{\circ}\text{C}$ as measured in the test cell.

$$Nu_x = \frac{h'x}{k} = 0.0308 Re_x^{0.8} Pr^{1/3} \quad 7.1$$

For all simulations, iterations were performed until residuals dropped to an acceptable level of $10\text{e-}3$. In Table 7.1, the results of CHT model are presented for each operating condition. Conduction in solid domain is accelerated by using time-scale factor to achieve compressor run time of 70 minutes as specified in Table 7.1. It can be noted that the flow validation has been preserved. Mass flow rate for each operating point matches the measurement results. The highest achieved mass flow rate is 0.0098 kg/s , while the lowest is 0.0036 kg/s . The calculated discharge air temperatures are lower than temperatures obtained from the non-conjugate analysis. This is expected due to heat transfer from the hot pressurized air to the rotors and casing. This heat eventually dissipates into the surrounding air. The highest discharge air temperature is $143 \text{ }^{\circ}\text{C}$, while the lowest is $51 \text{ }^{\circ}\text{C}$. A comparison with data in Table 7.1 indicates that the deviation is within 1 to $4 \text{ }^{\circ}\text{C}$. By calibrating the leakage gap size, the flow and power validation has already been achieved in the non-conjugate CFD model. This validation has been kept throughout the conjugate heat transfer simulation for all operating conditions. The main objective of CHT model was to validate rotor and housing surface temperatures.

The infrared thermography setup was first used to record the surface temperature data of the rotor lobes. As shown in Figure 7.19(a), an optical access was used, and camera was phase locked to take images at specified rotor position. These images have been used for comparison with the CHT model results in Figure 7.20 to Figure 7.24.

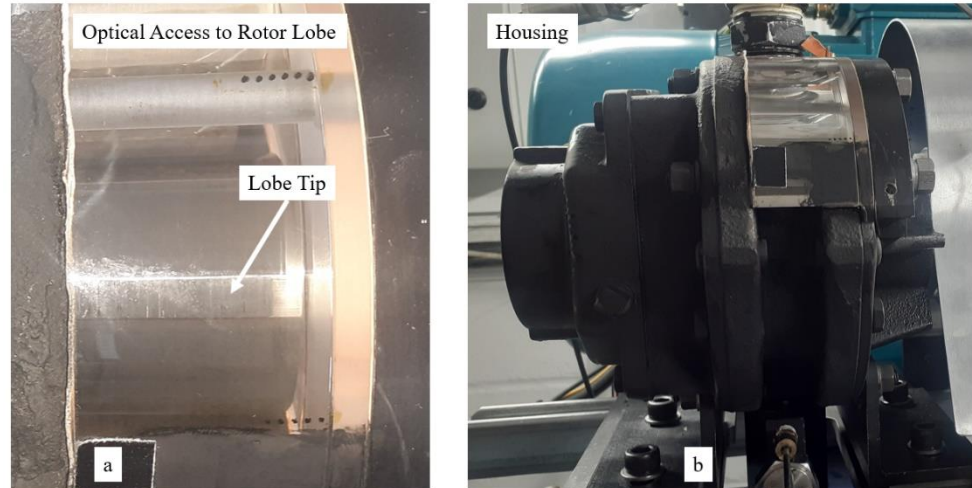


Figure 7.19 Thermography camera views a) Rotor lobe surface, b) Housing surface

The arrangement was modified, and the infrared camera was setup to record the surface temperature of the housing as shown in Figure 7.19(b). In this position, a view of the low temperature at the suction, high temperature at the discharge and the temperature distribution over the housing gets captured in one view. These images were used for comparison with the CHT model results in Figure 7.25.

Table 7.1 Conjugate heat transfer analysis results

	1000 rpm 1.2 PR	1500 rpm 1.2 PR	2000 rpm 1.2 PR	2000 rpm 1.4 PR	2000 rpm 1.6 PR
Solid initialization temperature [°C]	37	52	52	72	117
Solid time [min]	70	70	70	70	70
Flow time [s]	0.84	0.56	0.42	0.42	0.42
Exit temperature	51	58	57	84	143
Mass flow [kg/s]	0.0036	0.0066	0.0098	0.0083	0.00735

A qualitative comparison between the numerical results obtained by CHT simulation and provided experimental data is presented here. The experimental data presented in thermograms in the Figure 7.20 to Figure 7.24 are at the surface of the male rotor for each test condition. Comparison of rotor lobe surface temperature for 1.2 pressure ratio at 1000, 1500 and 2000 rpm rotor speed are shown in Figure 7.20, Figure 7.21, Figure 7.22

respectively. These three operating conditions are at lower pressure ratio and mostly in good agreement with experimental data. The highest deviation is observed for 1000 rpm and 1.2 pressure ratio and is around 10% with respect to the measured range (Figure 7.20).

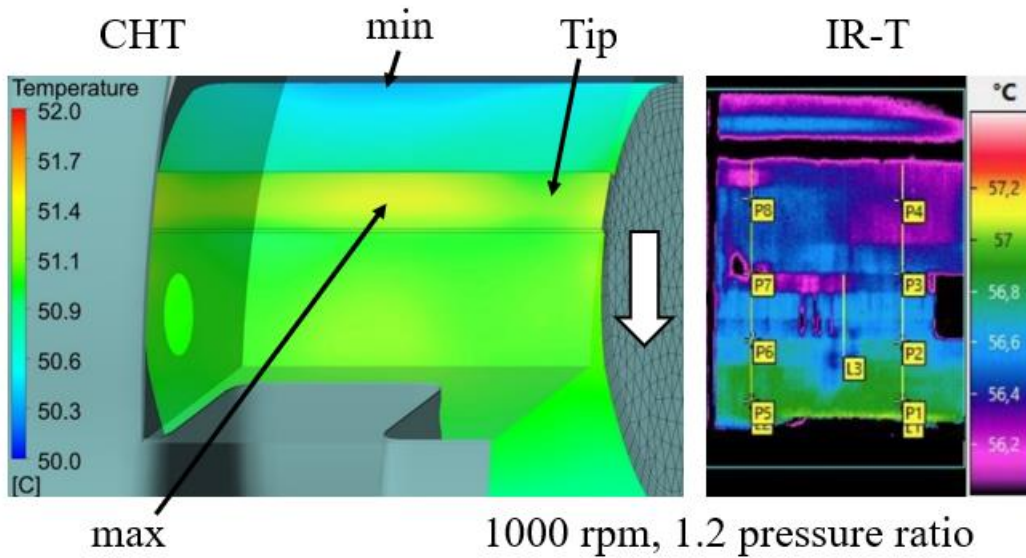


Figure 7.20 Surface temperature on the rotor lobe at 1000 rpm, 1.2 pressure ratio

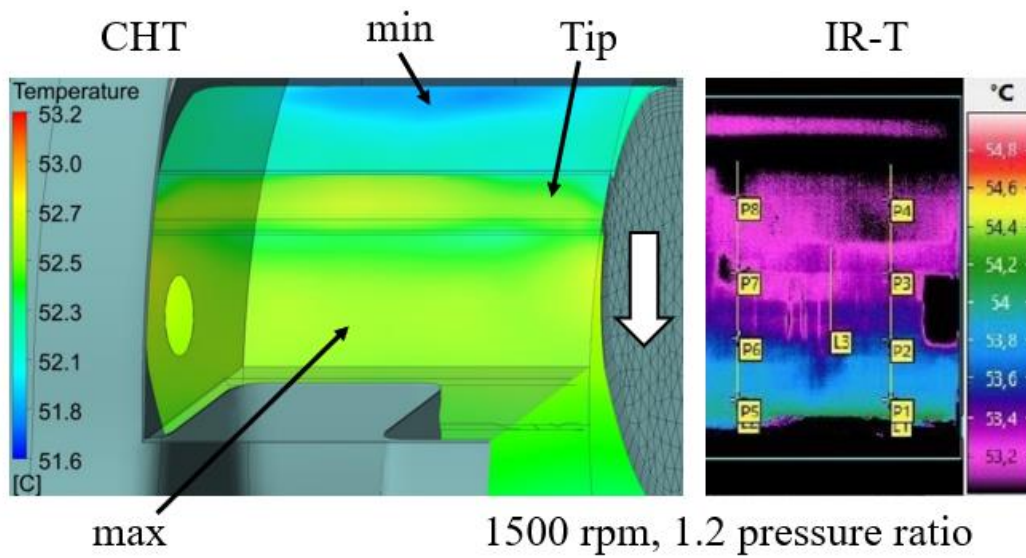


Figure 7.21 Surface temperature on the rotor lobe at 1500 rpm, 1.2 pressure ratio

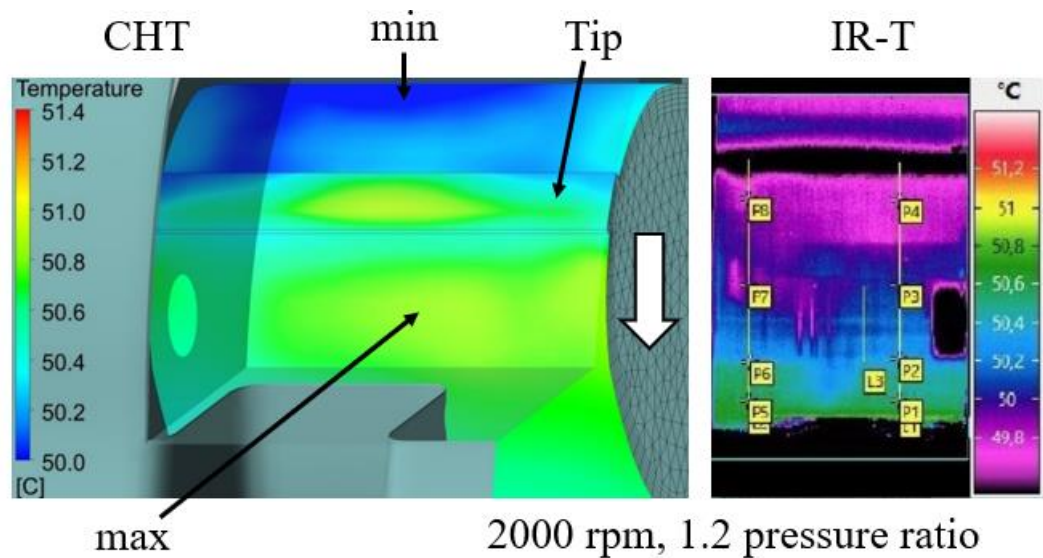


Figure 7.22 Surface temperature on the rotor lobe at 2000 rpm, 1.2 pressure ratio

Figure 7.23 and Figure 7.24 show the lobe surface temperature for 1.4 and 1.6 pressure ratio at 2000 rpm rotor speed. These are the higher-pressure ratio conditions, so higher temperatures are expected. Comparison with thermograms show that the transient CHT model was able to predict the results in the same range of temperature. However, it can be observed that the temperature profile on the tip is slightly different. There is a clear increase in temperature in the middle of the tip which is caused by very intense leakage flow in this area. There are also thermal traces from the axial gap leakage flow on the suction side. These are visible from both sides of the lobe. Quantitative range of the surface temperatures are well aligned with the thermograms on the right side but there is a difference in the qualitative variation of temperature field.

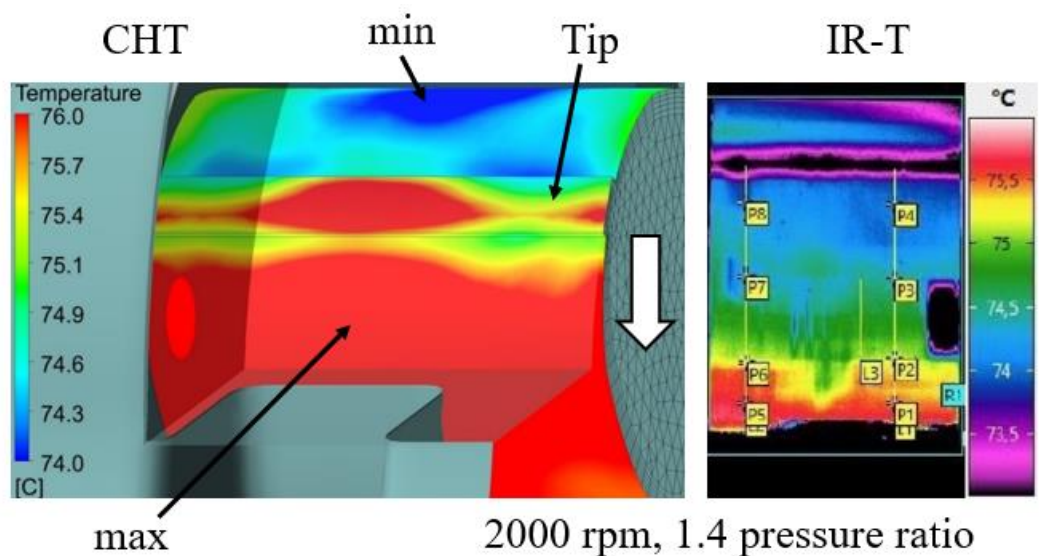


Figure 7.23 Surface temperature on the rotor lobe at 2000 rpm, 1.4 pressure ratio

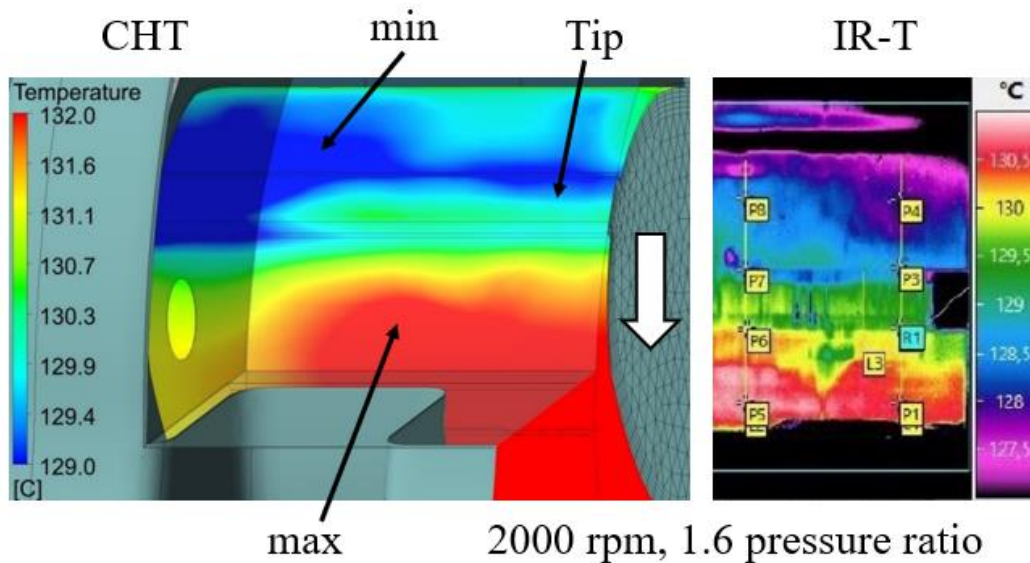


Figure 7.24 Surface temperature on the rotor lobe at 2000 rpm,1.6 pressure ratio

In Table 7.2, a comparison between the numerical results obtained by CHT simulation and IR Thermography data is presented for the rotor lobe regions of minimum and maximum temperatures. The general trend is that CHT model is under-estimating both minimum and maximum temperature at 1000 and 1500 rpm, 1.2 pressure ratio. While at 2000 rpm, both minimum and maximum temperatures are over-estimated by the CHT model. The highest difference between the recordings is about 5.7 °C at 1000 rpm and 1.2 pressure ratio. On an average the difference between CHT model and IR thermography temperature is about 1.85 °C for the rotor lobe.

Table 7.2 Comparison of IR Thermography and CHT results on rotor lobe

	Minimum Temperature [°C]			Maximum Temperature [°C]		
	IR-T	CHT	Difference	IR-T	CHT	Difference
1000 rpm 1.2 PR	56.4	50.3	5.7	57.2	52	5.2
1500 rpm 1.2 PR	53.2	51.6	1.6	54.8	53.2	1.6
2000 rpm 1.2 PR	49.8	50	0.2	51.2	51.4	0.2
2000 rpm 1.4 PR	73.5	74	0.5	75.5	76	0.5
2000 rpm 1.6 PR	127.5	129	1.5	130.5	132	1.5

Figure 7.25 presents instantaneous temperature on the exterior surfaces of the blower for the two highest pressure ratios 1.4 (Figure 7.25 a) and 1.6 (Figure 7.25 b) at 2000 rpm

rotor speed. Exterior surface temperatures obtained by numerical analysis are in good agreement with infrared thermography measurements. There is a slight qualitative difference in temperature variation on the right side of the blower where the gear box is located, but it is within acceptable deviation.

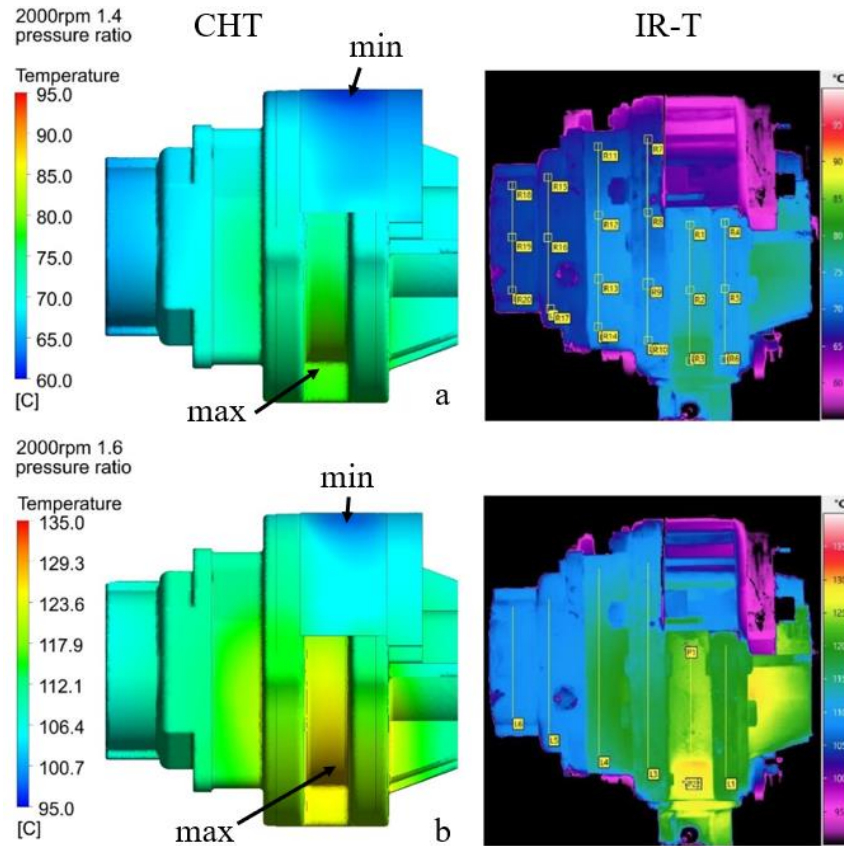


Figure 7.25 Surface temperature on the blower housing at 2000 rpm, 1.4 and 1.6 pressure ratio

Table 7.3 Comparison of IR Thermography and CHT results on housing

	Minimum Temperature [°C]			Maximum Temperature [°C]		
	IR-T	CHT	Difference	IR-T	CHT	Difference
1000 rpm 1.2 PR	54.0	55.0	1.0	58.0	59.0	1.0
1500 rpm 1.2 PR	50.0	52.0	2.0	57.0	56.0	1.0
2000 rpm 1.2 PR	47.0	50.0	3.0	57.0	53.0	4.0
2000 rpm 1.4 PR	60.0	65.0	5.0	85.0	80.0	5.0
2000 rpm 1.6 PR	95.0	100.7	5.7	135.0	129.3	5.7

In Table 7.3, a comparison between the numerical results obtained by CHT simulation and IR Thermography data is presented for the regions of minimum and maximum temperatures on the housing (Figure 7.25). For the housing, the general trend is that CHT

model is over-estimating the minimum temperature and under-estimating the maximum temperatures. The span of the temperature range is thus smaller in the CHT model data indicating more uniformity as compared to the measurement. The highest difference between the recordings is 5.7 °C at 2000 rpm and 1.6 pressure ratio. On an average the difference between CHT model and IR thermography temperature is about 3.34 °C for the housing which is slightly higher than that for the rotor lobe.

7.6 Summary

In this chapter observations of flow field inside the clearance gap, at the exit of the clearance gap and the entrance of the clearance gap are presented along with temperature analysis over the lobe surface temperature. Numerical conjugate heat transfer analysis is presented and compared it with experimental data. Secondary flow features such as boundary layer, vortexes and turbulence intensities are compared between stationary and operating condition of the machine. Significant difference in flow features between stationary condition and rotating condition is observed. Numerical CHT model also shows the good agreement with experimental data.

Chapter - 8 Conclusion, Recommendations and Contributions to Knowledge

8.1 Conclusion

This research focused on experimental measurements of the flow field and heat transfer in the leakage gap of the Roots blower. In this respect various experiment techniques are explored and three techniques: PLIF, IR Thermography and PIV are identified and used to measure temperature field, surface temperature and flow field of leakage flows. PLIF experiments were performed in LaVision, Germany while setup for PIV and IR thermography were developed at City, University of London along with the new National Instruments based DAQ system.

Feasibility study of PLIF proves that this technique can be used to measure temperature field inside the clearance gap, however improvements are needed to get accurate and reliable results. It was learned that the image mapping is critical and necessary to derive the temperature field. A proper temperature calibration process is also required.

High speed Infrared thermography can be used to measure the surface temperature of the lobe in running condition of the machine. Measurement results show that the surface temperature of the lobe exposed to the discharge port is always higher than the lobe surface exposed to the suction port, and that the difference is increasing with the increase in pressure ratio. However, at the same pressure ratio temperature is decreasing with the increase of rotational speed, which shows the impact of the leakage flow rate at various operating conditions on the temperature of the lobe. Measurements of the casing surface temperature are carried out at various speeds and pressure ratios at steady state condition and also carried out in transient condition. Measurements show higher temperature on the discharge port side while temperature is decreasing away from the discharge port. Same pattern of temperature change is observed on the discharge side of casing, such as at the same pressure ratio temperature is decreasing with the increase in speed. This experimental data is used to validate the CHT numerical model developed for the Roots blower.

PIV experiments with good spatial resolution enabled the velocity field measurement to be analysed in various flow areas in the clearance gap and around it. PIV experiments reveal the flow physics inside the clearance. Analysis of the flow through the clearance gap indicates the influence of the rotational speed on the average velocity of the flow

which affect the flowrate through the clearance gap. Average velocity in static condition is found to be higher than at all running conditions.

The flow field is captured inside the clearance gap, exit of the tip in the trailing edge and the entrance of the tip on the leading edge. PIV measurement confirms the presence of secondary flow in the leakage flow region. When flow enters the clearance gap from the high-pressure chamber, higher velocity gradient of air flow is observed over the rotor surface than on the casing surface. Velocity is significantly increased when the flow enters into the clearance gap over the tip. At the entrance of the tip, flow separation is observed due to the very high velocity and a boundary layer is observed over the entire span of the tip without any reattachment. Flow exits from the trailing edge of the tip as a jet. Vortices with the structure similar to ‘Kelvin-Helmholtz Instability’ are present. The size of vortices grow as they move away from the trailing edge. In summary, Figure 8.1 represents flow structures observed in the leakage flow of Roots blower using PIV measurement. This includes the boundary layer over the tip, vortex at the exit of the tip, high shear gradient over the surface of the lobe on the high-pressure side, velocity fluctuations in the high-pressure chamber near the entrance to the clearance gap.

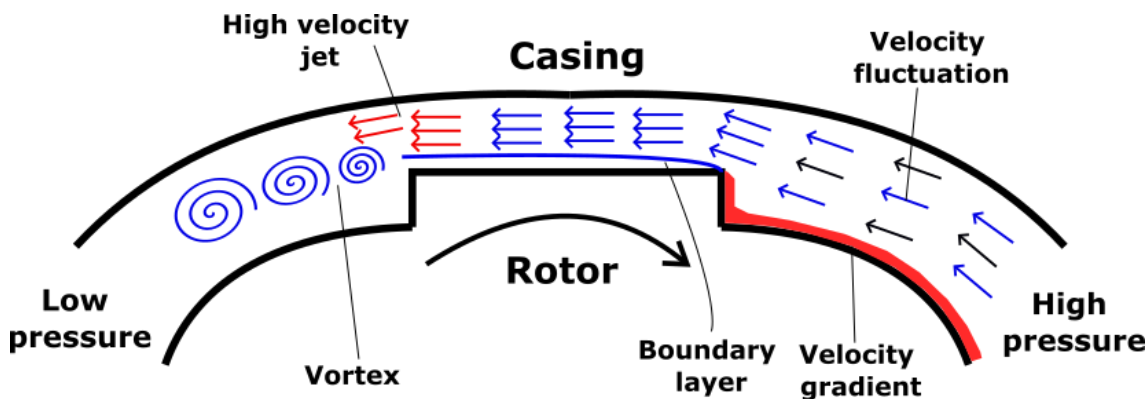


Figure 8.1 Schematic of flow structures found from the measurement in leakage flows

Produced set of experimental results provides good basis to validate the simulation leakage flow models. The observed flow field also suggests that the leakage flowrate can be reduced by disrupting the boundary layer which could be achieved by changing the geometry of the tip.

The outcome of this study is being used in project SECRET (Smart Efficient Compression: Reliability and Energy Targets) which is supported by an award from Royal Academy of Engineering and Howden UK.

8.2 Recommendations for future work

8.2.1 PIV experiments with various tip geometries

PIV measurement data in the clearance gap with a flat tip shows the boundary layer over the entire span of the tip and high-speed flow in the clearance gap. The leakage flow can be reduced by applying different tip features, either by increasing the boundary layer thickness which can reduce flow velocity and ultimately reduce the clearance flow rate, or by generating vortex in the platform of the tip which can act as a blockage. Suggested leakage reduction methods are supported by literature [67]. It shows that the cavity tip can be helpful to reduce the leakage flow by keeping same clearance gap while generating vortex on the tip. It is recommended that as the next step, experiments could be performed with the tip shapes shown in Figure 8.2 to observe the effect of the tip geometry on the leakage flow. Reason behind using cavity tip is to generate vortex inside the cavity of the tip which can act as blockage to the leakage flow. Primarily experiments can be carried out with Roots blower but afterwards it can be extended to screw machines.

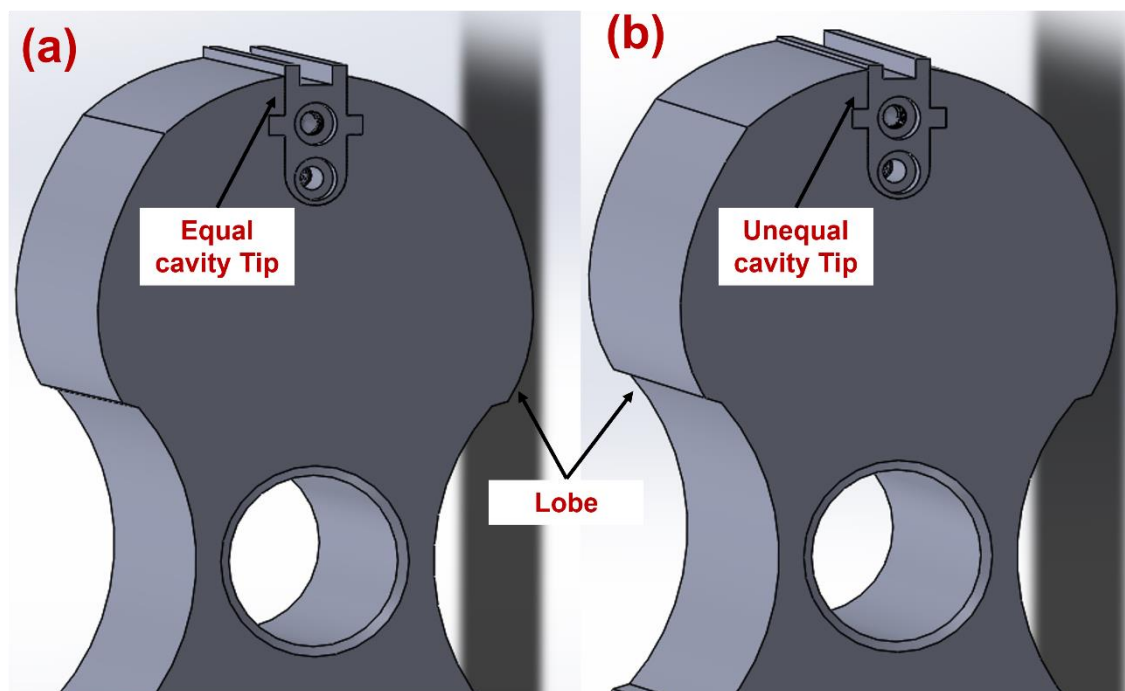


Figure 8.2 Various tip geometries

8.2.2 PLIF Experiments

Based on the feasibility study of PLIF, improvement areas are identified to perform PLIF, such as use of a DualScope camera instead of two cameras to eliminate the error cause due to the image mapping, use of nitrogen to improve signal to noise ratio and

development of robust temperature calibration method. The Suggested improvements in equipment are explained below.

8.2.2.1 Laser

UV laser is required in LIF experiment to illuminate the fluorescence. In current application, 266nm wavelength of the laser beam is required. It is preferable to utilize existing laser of 532 nm wavelength to avoid the cost of new UV laser. For that it is required to convert beam wavelength from 532nm to 266nm. But this conversion causes an 80% reduction in energy output, which is not preferable for PLIF. So, it is recommended to use Quantel Q-smart 850 laser which can provide 100mJ energy at 266nm wavelength.

8.2.2.2 Camera, Synchronizer, and optics

The same equipment explained in section 6.1.2 can be used as in the PLIF experiment except the laser which needs to be changed. However, an image intensifier and a dual scope optics is required for this experiment. Dual scope is a device which can divide camera sensor in two equal parts which renders unnecessary the need to use two independent cameras. Image Intensifier Unit 25 mm Multi alkali, H series and dual scope for two simultaneous measurements could be used. The arrangement of the dual scope optics and camera is shown in Figure 8.3. For temperature calibration it is recommended to supply pre-heated gas with known temperature. It is also recommended to use nitrogen as a working fluid which can boost the LIF signal 5 to 10 times higher than for air.



Figure 8.3 Dual scope with camera

8.2.2.3 Fluorescence tracers and Optical Filters

Various fluorescence tracers such as anisole, toluene, naphthalene, and acetone are suitable for gas-based application. Based on the literature search and the feasibility study which was carried out for PLIF, anisole is selected for this application. Comparison of

signals based on literature [42] is shown in Figure 8.4 depicts the better performance of Anisole.

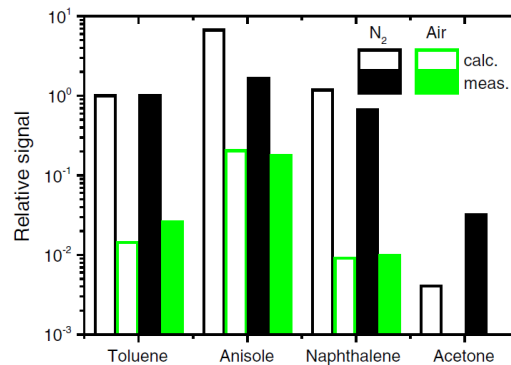


Figure 8.4 Measured and calculated signals per volume in N₂ and air (acetone only in N₂) relative to those of toluene in N₂ at room temperature[42].

8.3 Contributions to knowledge

The goal of this research is to experimentally study leakage flows through clearance gap of the Roots blower to understand flow physics and heat transfer phenomenon in the clearance gaps during the actual running conditions of the machine in order to improve reliability and the performance of the machine. In this regards, current research has delivered following listed contributions,

- It is demonstrated from the current study that PLIF is suitable technique to measure the temperature field inside the clearance. High speed IR thermography is successful to capture lobe surface temperature during the running condition of the machine and PIV is successful to capture flow fields inside the clearance during the running condition of the machine.
- State of the art experimental setup of PLIF, IR thermography and PIV techniques developed and utilised to generate the experimental measurements. Detailed design and setup procedure can be leveraged to study the similar flow phenomenon in other engineering rotary systems.
- Measured data are analysed and flow features such as boundary layer, flow acceleration and vortices are observed inside the clearance. Similarly, lobe surface and casing surface temperature of Roots blower are measured running conditions of the machine. This understanding has provided learning into the active control methods to reduce leakage losses in rotary PDMs, such as implementation of cavity shape can be useful to generate vortex on the platform of the tip, which can

block the leakage flow. In addition, this database provides the good basis for validation of numerical models developed in parallel with this study.

- Author has published two journal paper, four conference papers and one extended abstract based on the current study. All published papers are listed below,

Publications in journals as an author:

- Study of leakage flow in oil-free positive displacement rotary machines using particle image velocimetry, *Accepted in the Journal of Experimental Thermal and Fluid science*. doi: 10.1016/j.expthermflusci.2023.110886.
- The use of laser-induced fluorescence to measure temperature in the leakage gaps of oil-free positive displacement rotary machines, *Measurement: Journal of the International Measurement Confederation*, 2021. doi: 10.1016/j.measurement.2021.110057.

Publications in conferences as an author:

- Infrared-Thermography and numerical investigation of conjugate heat transfer in Roots blower, *26th International Compressor Engineering Conference at Purdue*, 2022.
- Development of State-of-the-art Experimental Technique to Investigate Temperature Field in Leakage Flows of Positive Displacement Machines, *25th International Compressor Engineering Conference at Purdue*, 2021.
- On Measuring Velocity and Temperature in Leakage Flows of Oil Free Rotary Positive Displacement Machines, *7th International Conference, New Technologies, Development and Application*, 2021.
- Experimental and Numerical Study of Flow Dynamics in the Leakage Gaps of Oil-Free Positive Displacement Machines, *Proceedings of the 8th World Congress on Momentum, Heat and Mass Transfer (MHMT'23)*.

Publications as a Co-author in journals and conferences:

- Analysis of Conjugate Heat Transfer in a Roots Blower and validation with Infrared Thermography, *International Journal of Thermofluids*, 2022.
- Systematic engineering design approach for improvement of oil-free twin-screw compressors, *International Conference on Screw Machines 2022*.
- Experimental investigation of screw compressor clearance monitoring techniques, *26th International Compressor Engineering Conference at Purdue*, 2022.

References

- [1] D. Vittorini, G. Bianchi, and R. Cipollone, “Energy saving potential in existing volumetric rotary compressors,” *Energy Procedia*, vol. 81, pp. 1121–1130, 2015, doi: 10.1016/j.egypro.2015.12.137.
- [2] R. Cipollone, “Carbon and energy saving markets in compressed air,” *IOP Conf. Ser. Mater. Sci. Eng.*, vol. 90, no. 1, 2015, doi: 10.1088/1757-899X/90/1/012085.
- [3] I. Mattei, “Issue 4, Vane Magazine, December 2015,” no. 4, 2016.
- [4] S. Rane, “Grid Generation and CFD Analysis of Variable Geometry Screw Machines,” City University London, 2015.
- [5] U. C. C. United Nations Climate Change Conference, “the Glasgow,” *Cop26 Glas. Clim. Pact*, p. 28, 2021.
- [6] A. Kovacevic, N. Stosic, E. Mujic, and I. K. Smith, “Analysis of clearances in combined screw machines,” *Am. Soc. Mech. Eng. Adv. Energy Syst. Div. AES*, vol. 45, no. January, pp. 35–41, 2005, doi: 10.1115/IMECE2005-79325.
- [7] J. S. Fleming and Y. Tang, “The analysis of leakage in a twin screw compressor and its application to performance improvement,” *Proc. Inst. Mech. Eng. Part E J. Process Mech. Eng.*, vol. 209, no. 2, pp. 125–136, 1995, doi: 10.1243/PIME_PROC_1995_209_239_02.
- [8] M. Janicki and K. Kauder, “The influence of clearance flows on the working behaviour of screw compressors simulation results,” *VDI Berichte*, no. 1932, pp. 3–17, 2006.
- [9] R. Sachs, “Experimental investigation of Gas flows in screw machines,” University of Dortmund, 2002.
- [10] Q. Zhang, D. O. O’Dowd, L. He, A. P. S. Wheeler, P. M. Ligrani, and B. C. Y. Cheong, “Overtip shock wave structure and its impact on turbine blade tip heat transfer,” *J. Turbomach.*, vol. 133, no. 4, pp. 1–8, 2011, doi: 10.1115/1.4002949.
- [11] N. Stosic, “On heat transfer in screw compressors,” *Int. J. Heat Fluid Flow*, vol. 51, pp. 285–297, 2015, doi: 10.1016/j.ijheatfluidflow.2014.10.026.
- [12] P. K. Kauder and D. D. Stratmann, “Theoretical Gas Flow through Gaps in Screw-type Machines,” 2002.
- [13] J. Vimmr and O. Fryč, “Numerical simulation of leakage flow between moving rotor and housing of screw compressor.”
- [14] D. Guerrato, J. M. Nouri, N. Stosic, C. Arcoumanis, and I. K. Smith, “Flow measurements in the discharge port of a screw compressor,” *Proc. Inst. Mech. Eng. Part E J. Process Mech. Eng.*, vol. 222, no. 4, pp. 201–210, 2008, doi: 10.1243/09544089JPME200.
- [15] A. Kovacevic, M. Arjneh, S. Rane, N. Stosic, and M. Gavaises, “Flow

- visualization at suction of a twin screw compressor,” *Int. Conf. Screw Mach. Dortmund Ger.*, 2014.
- [16] A. Kovacevic, N. Stosic, and I. Smith, “The influence of rotor deflection upon screw compressor performance,” *VDI Berichte*, no. 1715, pp. 17–27, 2002.
- [17] D. Buckney, “Clearance management in twin screw compressors,” City, University of London, 2017.
- [18] N. Stosic, I. K. Smith, and A. Kovacevic, “Estimation and Control of Heat Transfer in Screw Compressor Rotors,” pp. 441–446, 2008, doi: 10.1115/imece2004-60516.
- [19] U. Daemgen, P. Hadamitzky, and J. Dohmann, “Thermal expansion in liquid-injected screw compressors,” *IOP Conf. Ser. Mater. Sci. Eng.*, vol. 425, no. 1, pp. 3–11, 2018, doi: 10.1088/1757-899X/425/1/012010.
- [20] J. D. Coull and N. R. Atkins, “The Influence of Boundary Conditions on Tip Leakage Flow,” vol. 137, no. June, pp. 1–10, 2015, doi: 10.1115/1.4028796.
- [21] Q. Zhang and L. He, “Overtip choking and its implications on turbine blade-tip aerodynamic performance,” *J. Propuls. Power*, vol. 27, no. 5, pp. 1008–1014, 2011, doi: 10.2514/1.B34112.
- [22] J. Maynard, A. P. S. Wheeler, J. Taylor, and R. Wells, “Unsteady structure of compressor tip leakage flows,” *J. Turbomach.*, vol. 145, no. May, pp. 1–27, 2022, doi: 10.1115/1.4055769.
- [23] G. Singh, S. Sun, A. Kovacevic, Q. Li, and C. Bruecker, “Transient flow analysis in a Roots blower: Experimental and numerical investigations,” *Mech. Syst. Signal Process.*, vol. 134, p. 106305, 2019, doi: 10.1016/j.ymsp.2019.106305.
- [24] S. Sun, G. Singh, A. Kovacevic, and C. Bruecker, “Experimental and Numerical Investigation of Tip Leakage Flows in a Roots Blower,” *Designs*, vol. 4, no. 1, p. 3, 2020, doi: 10.3390/designs4010003.
- [25] Roland Muller, “Gap flow with heat transfer in vacuum pumps,” 2013.
- [26] Q. Zhang, “Impact of Wall Temperature on Turbine Blade Tip Aerothermal Performance,” vol. 136, no. May 2014, pp. 1–9, 2018, doi: 10.1115/1.4026001.
- [27] H. Jiang and Q. Zhang, “Experimental evidence of temperature ratio effect on turbine blade tip heat transfer,” no. c, 2018, doi: 10.1115/1.4041811.
- [28] T. James Macbeth, “Conjugate Heat Transfer and Average Versus Variable Heat Transfer Coefficients,” 2016.
- [29] T. L. Perelman, “On conjugate problems of heat transfer,” vol. 3, no. 1, pp. 293–303, 1961.
- [30] W. K. S. Chiu, C. J. Richards, and Y. Jaluria, “Experimental and Numerical Study of Conjugate Heat Transfer in a Horizontal Channel Heated From Below,” *J. Heat Transfer*, vol. 123, no. 4, p. 688, 2002, doi: 10.1115/1.1372316.

- [31] G. Croce, M. A. Coppola, and O. Rovenskaya, “Conjugate heat transfer performance for gaseous flows in short micro channels,” *ASME 2014 12th Int. Conf. Nanochannels*, pp. 1–6, 2014.
- [32] S. Joneydi, “Analytical Solution of Conjugate Turbulent Forced Convection Boundary Layer Flow Over Plates,” *Therm. Sci.*, vol. 20, no. 5, pp. 1499–1507, 2016, doi: 10.2298/tsci140115062j.
- [33] N. Degen, “An Overview on Schlieren Optics and its Applications,” *Electron. Instrum. Cust.*, vol. 17, pp. 3–6, 2010.
- [34] A. Martínez-González, J. A. Guerrero-Viramontes, and D. Moreno-Hernández, “Temperature and velocity measurement fields of fluids using a schlieren system,” *Appl. Opt.*, vol. 51, no. 16, p. 3519, Jun. 2012, doi: 10.1364/ao.51.003519.
- [35] G. S. Settles and M. J. Hargather, “A review of recent developments in schlieren and shadowgraph techniques,” *Meas. Sci. Technol.*, vol. 28, no. 4, 2017, doi: 10.1088/1361-6501/aa5748.
- [36] F. Scarano, “Overview of PIV in supersonic flows,” *Top. Appl. Phys.*, vol. 112, pp. 445–463, 2008, doi: 10.1007/978-3-540-73528-1_24.
- [37] R. A. Humble, F. Scarano, B. W. Van Oudheusden, and M. Tuinstra, “PIV Measurements of a Shock Wave / Turbulent Boundary Layer Interaction 2 . Apparatus and Experimental Technique,” *13th Int. Symp. Appl. Laser Tech. to Fluid Mech. Lisbon, Port.*, no. May 2014, pp. 1–11, 2006.
- [38] M. Raffel, C. Willert, S. Wereley, and J. Kompemhans, *Particle Image Velocimetry*, Second \ed. Springer, New York.
- [39] “Dantec Dynamics.” <https://www.dantecdynamics.com/solutions-applications/solutions/fluid-mechanics/particle-image-velocimetry-piv/measurement-principles-of-piv/>
- [40] C. Schulz and V. Sick, “Tracer-LIF diagnostics: Quantitative measurement of fuel concentration, temperature and fuel/air ratio in practical combustion systems,” *Prog. Energy Combust. Sci.*, vol. 31, no. 1, pp. 75–121, 2005, doi: 10.1016/j.pecs.2004.08.002.
- [41] P. Kranz *et al.*, “In-Cylinder LIF Imaging, IR-Absorption Point Measurements, and a CFD Simulation to Evaluate Mixture Formation in a CNG-Fueled Engine,” *SAE Int. J. Engines*, vol. 11, no. 6, pp. 1221–1238, 2018, doi: 10.4271/2018-01-0633.
- [42] S. Faust, M. Goschütz, S. A. Kaiser, T. Dreier, and C. Schulz, “A comparison of selected organic tracers for quantitative scalar imaging in the gas phase via laser-induced fluorescence,” *Appl. Phys. B Lasers Opt.*, vol. 117, no. 1, pp. 183–194, 2014, doi: 10.1007/s00340-014-5818-x.
- [43] R. Mathie, “Unsteady and Conjugate Heat Transfer in Convective-Conductive Systems,” no. August, p. 278, 2012, [Online]. Available: <http://ethos.bl.uk/OrderDetails.do?uin=uk.bl.ethos.570056>

- [44] J. Cernecky, J. Koniar, and Z. Brodnianska, “The Effect of Heat Transfer Area Roughness on Heat Transfer Enhancement by Forced Convection,” *J. Heat Transfer*, vol. 136, no. 4, p. 041901, 2014, doi: 10.1115/1.4025920.
- [45] P. Dancova, P. Psota, and T. Vit, “Measurement of a Temperature Field Generated by a Synthetic Jet Actuator using Digital Holographic Interferometry,” *Actuators*, vol. 8, no. 1, p. 27, Mar. 2019, doi: 10.3390/act8010027.
- [46] C. Herman and E. Kang, “Experimental Visualization of Temperature Fields and Study of Heat Transfer Enhancement in Oscillatory Flow in A Grooved Channel,” *Heat Mass Transf.*, vol. 37, pp. 87–89, Jul. 2001, doi: 10.1007/978-94-011-1090-7_16.
- [47] P. C. Lee and C. Pan, “Boiling heat transfer and two-phase flow of water in a single shallow microchannel with a uniform or diverging cross section,” *J. Micromechanics Microengineering*, vol. 18, no. 2, 2008, doi: 10.1088/0960-1317/18/2/025005.
- [48] Vinod Narayanan, “Temperature measurements and surface visualization in microchannel flows using infrared thermography,” *ICMM2003-1117*, 2003.
- [49] V. E. Srinath and H. Je-Chin, “A transient liquid crystal thermography technique for gas turbine heat transfer measurements,” *Meas. Sci. Technol.*, vol. 11, no. 7, p. 957, 2000, [Online]. Available: <http://stacks.iop.org/0957-0233/11/i=7/a=312>
- [50] J. Speakman, “Infrared thermography: Principles and applications,” no. September, 2019.
- [51] V. Le Saux and S. Wode, “Performance Comparison between ImageIR ® 8300 hp and ImageIR ® 10300 on a Thermoelastic Stress Analysis Experiment Performance Comparison between ImageIR ® 8300 hp and ImageIR ® 10300 on a Thermoelastic Stress Analysis Experiment,” vol. 3722.
- [52] O. Breitenstein and S. Sturm, “Lock-in thermography for analyzing solar cells and failure analysis in other electronic components,” *Quant. Infrared Thermogr. J.*, vol. 16, no. 3–4, pp. 203–217, 2019, doi: 10.1080/17686733.2018.1563349.
- [53] I. Jonsson, V. Chernoray, and R. Dhanasegaran, “Infrared Thermography Investigation of Heat Transfer on Outlet Guide Vanes in a Turbine Rear Structure,” *Int. J. Turbomachinery, Propuls. Power*, vol. 5, no. 3, 2020, doi: 10.3390/ijtpp5030023.
- [54] B. Cukurel, T. Arts, and C. Selcan, “Conjugate heat transfer characterization in cooling channels,” *J. Therm. Sci.*, vol. 21, no. 3, pp. 286–294, 2012, doi: 10.1007/s11630-012-0546-1.
- [55] Q. Zhang and L. He, “Turbine blade tip aero-thermal management: Some recent advances and research outlook,” *J. Glob. Power Propuls. Soc.*, vol. 1, no. 1985, p. K7ADQC, 2017, doi: 10.22261/jgpps.k7adqc.
- [56] T. L. Liu and C. Pan, “Infrared thermography measurement of two-phase boiling flow heat transfer in a microchannel,” *Appl. Therm. Eng.*, vol. 94, pp. 568–578, 2016, doi: 10.1016/j.applthermaleng.2015.10.084.

- [57] D. A. Rothamer, J. A. Snyder, R. K. Hanson, and R. R. Steeper, “Two-wavelength PLIF diagnostic for temperature and composition,” *SAE Int. J. Fuels Lubr.*, vol. 1, no. 1, pp. 520–533, 2009, doi: 10.4271/2008-01-1067.
- [58] C. García-López and G. Álvarez-Tey, “Evaluation of the Uncertainty of Surface Temperature Measurements in Photovoltaic Modules in Outdoor Operation,” *Sensors*, vol. 22, no. 15, 2022, doi: 10.3390/s22155685.
- [59] B. Patel, A. Kovacevic, A. Charogiannis, and Md nahinul Alam, “Development of State-of-the-art Experimental Technique to Investigate Temperature Field in Leakage Flows of Positive Displacement Machines,” in *International Compressor Engineering Conference, Purdue University*, 2021.
- [60] A. Kotlov, L. Kuznetsov, and B. Hrustalev, “Investigation of the influence of the number of vanes on the performance of a rotary vane compressor,” *MATEC Web Conf.*, vol. 245, 2018, doi: 10.1051/mateconf/201824504008.
- [61] B. Cushman-Roisin, “Kelvin - Helmholtz instability as a boundary-value problem,” *Environ. Fluid Mech.*, vol. 5, no. 6, pp. 507–525, 2005, doi: 10.1007/s10652-005-2234-0.
- [62] B. D. Wieneke, *PIV Uncertainty Quantification and Beyond*. TU delft university, 2022. doi: 10.4233/uuid:4ca8c0b8-0835-47c3-8523-12fc356768f3.
- [63] A. Sciacchitano, B. Wieneke, and F. Scarano, “PIV uncertainty quantification by image matching,” *Meas. Sci. Technol.*, vol. 24, no. 4, 2013, doi: 10.1088/0957-0233/24/4/045302.
- [64] R. Martinuzzi and C. Tropea, “the Flow Around Surface-Mounted, Prismatic Obstacles Placed in a Fully Developed Flow,” *J. Fluids Eng.*, vol. 115, pp. 85–92, 1993.
- [65] J. C. F. Pereira and B. Schönung, “Experimental and theoretical investigation of backward-facing step flow,” *J. Fluid Mech.*, vol. 127, pp. 473–496, 1983, doi: 10.1017/S0022112083002839.
- [66] M. Matuzović, S. Rane, B. Patel, A. Kovačević, and Ž. Tuković, “Analysis of conjugate heat transfer in a roots blower and validation with infrared thermography,” *Int. J. Thermofluids*, vol. 16, p. 100234, 2022, doi: 10.1016/j.ijft.2022.100234.
- [67] A. P. S. Wheeler, T. Korakianitis, and S. Banneheke, “Tip-Leakage Losses in Subsonic and Transonic Blade Rows,” *J. Turbomach.*, vol. 135, no. 1, pp. 1–7, 2012, doi: 10.1115/1.4006424.

Appendix A Modelling of conjugate heat transfer in clearance gap of a Roots blower

This section presents the methodology used for conjugate heat transfer modelling. Heat transfer to solid domains of rotors and casing is included in these calculations. First, the computational domain and case setup are presented. In the results section, the numerical solution is discussed and compared against infrared thermography data. The test Roots blower that was used to obtain empirical data was modified to include transparent sapphire glass for optical access. By making the blower's rotor optically accessible, infrared thermography technique can be employed to obtain temperature fields on the surfaces.

A.1 Computational domain for CHT model

The main elements of the model are shown in Figure A 1. The blower model consists of the steel parts such as rotors and housing and the sapphire glass part which provides optical access for infrared thermography. The properties of these material are given in Table A 2.

The computational mesh is made of 2 648 939 control volumes in total:

- 1 366 176 hexahedral and tetrahedral CVs in the solid domain
- 1 282 763 hexahedral CVs in the fluid domain

The geometry containing calibrated axial clearance domain (Obtained in Stage I of the analysis) and other fluid domains stayed the same. It was upgraded with the solid elements and connected by non-conformal interfaces. The computational domain thus consists of multiple subdomains connected by non-conformal boundaries. Some of the interfaces are shown in Figure 4 along with the components of the CHT model. There are 19 non-conformal interfaces required to be defined in this setup:

- 8 fluid-fluid non-conformal interfaces
- 7 fluid-solid non-conformal interfaces
- 4 solid-solid non-conformal interfaces
- 1 fluid-fluid conformal interface between two dynamic rotor domains

All fluid-solid and solid-solid interfaces have been made using the mapped coupled wall option. The mapped mesh interface option is an alternative approach for modelling CHT between fluid-solid zones. It is more robust than the standard non-conformal interface formulations in cases where the interface zones are poorly aligned and penetrate each other or have gaps between them. Local tolerance is set to 10 in the setup. In the two solid

rotor domains there is no need to control the motion of each node independently, so both rotors are specified as dynamic zones with rigid body motion. The rotational speed is applied according to the operating condition.

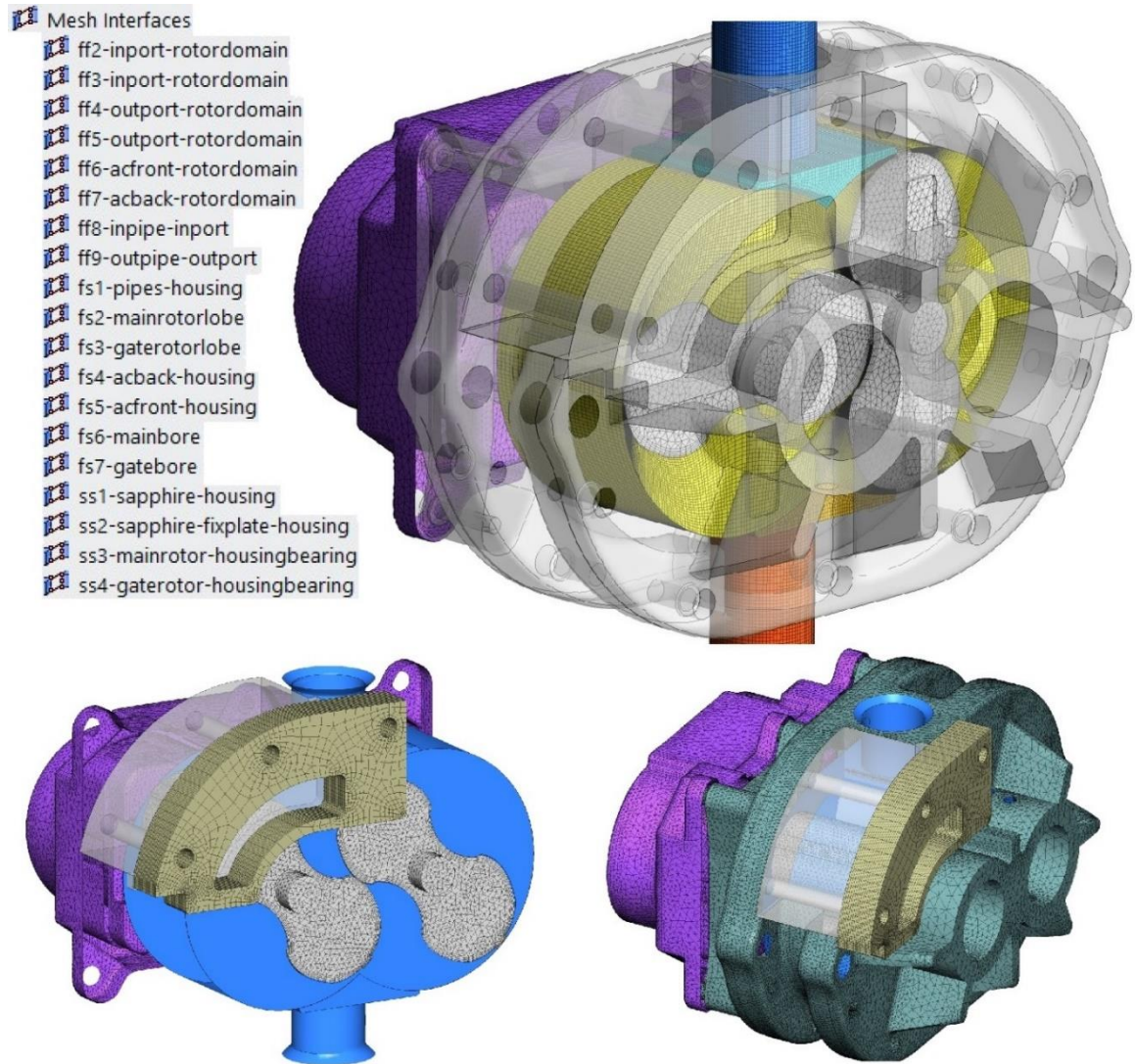


Figure A 1 Computational domain of the full CHT model

A.2 CHT Simulation setup

For CHT analysis, boundary conditions are listed in Table A 1. The main difference was in the specification of wall type boundaries which were not adiabatic in this model. Coupled thermal boundary condition is used at the fluid-solid and solid-solid interfaces to capture thermal interactions between these zones by enforcing continuous temperature and balance the thermal flux. This allows for obtaining the temperature field in both zones which are divided by the thermal interface. Convection thermal boundary condition is assigned on the external boundaries of the compressor. The flow field is not expected to

change significantly with the inclusion of heat transfer so the numerical solution from adiabatic CFD simulations was used as initial condition. Fully converged solution from the non-conjugate CFD simulation is written for each case to an interpolation file and then imported to CHT case as an initial guess of the solution flow. The existing CFD model with air as the working medium was extended with solid material properties provided from Ansys Fluent material database. The following material properties of steel and sapphire glass were specified in the CHT model.

Table A 1 Testing operating conditions

Pressure inlet [bar]	Temperature inlet [°C]	Pressure outlet [bar]	Temperature outlet [°C]	Mass flow rate [kg/s]
1.024	29.66	1.24	52.46	0.0033
1.024	29.19	1.232	59.06	0.0063
1.023	30.03	1.23	57.72	0.0092
1.023	30.92	1.439	82.31	0.0078
1.023	33.8	1.635	139.05	0.007

Table A 2 Material properties of glass and steel

Property	Glass	Steel
Density [kg/m ³]	2401.7	8030
Specific heat [J/(kgK)]	869.99	502.48
Thermal conductivity [W/(mK)]	2.548	16.27

Conduction and convection processes are very different phenomena with each having its own time scale for heat transfer. This poses a problem because in the case of conjugate heat transfer, conduction represents an order of magnitude lower time scale in reaching quasi-steady state. Time marching in solid domain has to be accelerated to overcome this issue and allow for reaching quasi-steady state in reasonable amount of computational time. Fluent solver provides the option to specify an independent solid time step size which enables a different time step size to be defined for solid domain as compared to the main flow time scale. This approach was used in the current study to overcome the time scale disparity. For fluid domain, the time step is determined from the pre-defined rotational speed and crank angle step size parameter of the rotor motion. These are set in dynamic mesh of the fluid zones. The combination of these two parameters returns the

time step size for the solver. Effectively, two cases with different rotational speed will return different time steps if crank angle step size and rotor grid movement per step remains the same. The ratio between the fluid and solid domain time steps can be defined as the time-scale factor tsf and it has been varied with the operating conditions as presented in Table 3:

$$tsf = \frac{\Delta t_s}{\Delta t_f} \quad A 1$$

The time-scale factors are chosen to achieve the same run time for all operating conditions. This also sets the same solid zone time step size.

Table A 3 Flow data

	1000 rpm 1.2 PR	1500 rpm 1.2 PR	2000 rpm 1.2 PR	2000 rpm 1.4 PR	2000 rpm 1.6 PR
Crank shaft speed [rpm]	1000	1500	2000	2000	2000
Crank angle step size [°]	1	1	1	1	1
Fluid zone time step [s]	0.000166	0.000111	8.33e-5	8.33e-5	8.33e-5
Solid zone time step [s]	0.833	0.833	0.833	0.833	0.833
Time-scale factor	5000	7500	10000	10000	10000

Appendix B MATLAB code for PLIF- two camera image mapping

```

%% readimx load
addpath 'D:\Lavision add on\readimx-v2.1.8-win64'; %add the file readimx

fn_654_320 = 'D:\Lavision best extracted
files\RootsTest_13022020\S=301_T=22_P=1.04_L=320_Meas.set'; %load file 320
fn_654_280 = 'D:\Lavision best extracted
files\RootsTest_13022020\S=301_T=22_P=1.04_L=280_A=130.set'; %load file 280

for i=1:200 %for i going from 1 to 200
    A=readimx(fn_654_320,i); %read an image from file 320
    ims_1 = A.Frames{1}.Components{1}.Planes{1}; %access to frame
(n),component (n) and plane (n)
    ims1=flipud(ims_1);
    ims1=rot90(ims1,3);
    X2(:,:,i)=ims1(:,:,); %store all 200 on one matrix C
end

for i=1:200 %for i going from 1 to 200
    B=readimx(fn_654_280,i); %read an image from file 280
    ims_2 = B.Frames{1}.Components{1}.Planes{1}; %access to frame
(n),component (n) and plane (n)
    ims2=flipud(ims_2);
    ims2=rot90(ims2,3);
    Y2(:,:,i)=ims2(:,:,); %store all 200 on one matrix D
end

result_301_320_1 = mean(reshape(X2,1216,1936,200,1),3); %mean of all 320
result_301_280_1 = mean(reshape(Y2,1216,1936,200,1),3); %mean of all 280

result_654_320_l1 = nanmean(X2,3);
result_654_280_l1 = nanmean(Y2,3);

figure(2) %name of mean ratio figure
plot(result_654_320_l1); %plot the ratio figure
imagesc(result_654_320_l1); %display the ratio figure with color
colorbar

% Frame 1, Calib 03
fileID = fopen('03_1_points.txt','r');
t = fscanf(fileID, '%f %f', [2 Inf]);
fclose(fileID);
[~, n] = size(t);
y1(1,:) = 1000*t(1,:);
y1(2,:) = 1000*t(2, :);
y1(3,:) = ones([1, n]);
% Frame 0, Calib 03
fileID = fopen('03_0_points.txt','r');
t = fscanf(fileID, '%f %f', [2 Inf]);
fclose(fileID);
[~, n] = size(t);
x1(1,:) = 1000*t(1,:);
x1(2,:) = 1000*t(2, :);

```

```
x1(3,:) = ones([1, n]);
y3 = y1;
x3 = x1;
img = result_654_320_l1;
figure();
imshow(img, []);
[m n k] = size(img)
tform = fitgeotrans(x3(1:2,:)', y3(1:2,:)', 'NonreflectiveSimilarity');
trans = imwarp(img, tform);
figure();
plot(trans);      %plot the ratio figure
imagesc(trans);   %display the ratio figure with color
colorbar
writeimx(trans, 'D:\Files for Akash\MATLab Code\trans.im7');
```